



VNIVERSITAT E VALÈNCIA

Instituto de Ciencia Molecular
Doctorado en Nanociencia y Nanotecnología

**Low dimensional perovskites: synthetic
methods and applications in optoelectronics**

Tesis doctoral

Maria Grazia Immacolata La Placa

Directores:

Prof. Hendrik Jan Bolink

Dr. Michele Sessolo

Febrero 2020

Prof. Hendrik Jan Bolink y **Dr. Michele Sessolo**, Investigadores de la Universidad de Valencia en el Instituto de Ciencia Molecular (ICMol), certifican que la memoria presentada por la estudiante de doctorado Maria Grazia Immacolata La Placa, con el título “Low dimensional perovskites: synthetic methods and applications in optoelectronics” corresponde a su Tesis Doctoral y ha sido realizada bajo su dirección y tutoría, autorizando mediante este escrito la presentación de la misma.

En Valencia, a 19 de febrero del 2020



Prof. Hendrik Jan Bolink
(director y tutor)



Dr. Michele Sessolo
(director)

Per aspera ad astra

*Dedicato ai miei mentori, ai miei amici,
alla mia famiglia, a me.*

Index

	Page
Chapter 1. Introduction and Aim of the thesis	1
1.1 Overview	1
1.2 Perovskite	7
1.2.1 Three dimensional (hybrid) organic-inorganic perovskite	9
1.2.2 Low dimensional (hybrid) organic-inorganic perovskite	11
1.3 Properties of perovskite semiconductor	13
1.4 Optical and structural properties of metal halide perovskite.	17
1.5 Operating principle of photovoltaic devices	26
1.6 Operating principle of light-emitting diodes	32
1.7 Solar cell and light-emitting device architecture	36
1.8 Perovskite thin film deposition techniques	38
1.8.1 Solution-processing deposition	39
1.8.2 Vacuum-processing deposition	42
1.9 Aim of the thesis	46
Chapter 2. Enhance the photoluminescence quantum yield of the perovskite film	49
Chapter 3. Vacuum-deposition of low dimensional perovskites	65
Chapter 4. Vacuum-deposited 2D/3D perovskite heterojunctions	91
Chapter 5. General conclusion	111
Chapter 6. Spanish summary / Resumen en castellano	115
Bibliography	137
Appendices	149
List of abbreviations and acronyms	173
Author contributions	177
Acknowledgements	181

Chapter 1

Introduction and aim of the thesis

1.1 Overview

The global energy consumption in 2018 increased at nearly twice the average rate of growth since 2010¹, driven by a developing global economy to sustain societal needs such as feeding, heating, cooling and transportation. Unfortunately, today's energy production strongly depends on fossil fuels as oil, natural gas and coal, which are economically convenient but present finite reserves and produce carbon dioxide (CO₂) and other greenhouse gases as by-products of combustion. There is overwhelming and unquestionable evidence for the fact that the Earth's climate is warming and that it is because of increased man-made greenhouse gas emissions (**Figure 1.1**). Moreover, in our energy-centric world the control over oil and gas resources (and their means of delivery) translates into geopolitical and military conflicts.



Figure 1.1. Left: corals seen in Dibba, on the east coast of the northern United Arab Emirates, are healthy and teeming with fish in 2004. Right: the reef was devastated in 2008 by harmful algae blooms, linked, to increased greenhouse gases and rising ocean temperatures. The tide kills sea life by depleting the oxygen in the water.²

In an attempt to arrest global warming from the greenhouse effect, the Kyoto Protocol and then the Paris climate agreements demand a reduction of global CO₂ emissions. In the latest and most recent agreement, 197 nations agreed to keep a global temperature rise well below 2 degrees Celsius above pre-industrial levels and to pursue efforts to limit the temperature increase even further to 1.5 degrees Celsius.³ In order to reach this target and at the same time meet the high global energy/power demands, energy has to be produced and used in cleaner, better ways with fewer emissions. Employing renewable energy sources is the most promising solution to achieve those goals. Renewable alternatives include hydropower, biomass/biofuels, geothermal, ocean thermal energy conversion, waves, tides, wind, and solar. A review of renewable energy potential showed that solar energy availability exceeds all other renewables by orders of magnitude⁴ (**Figure 1.2**).

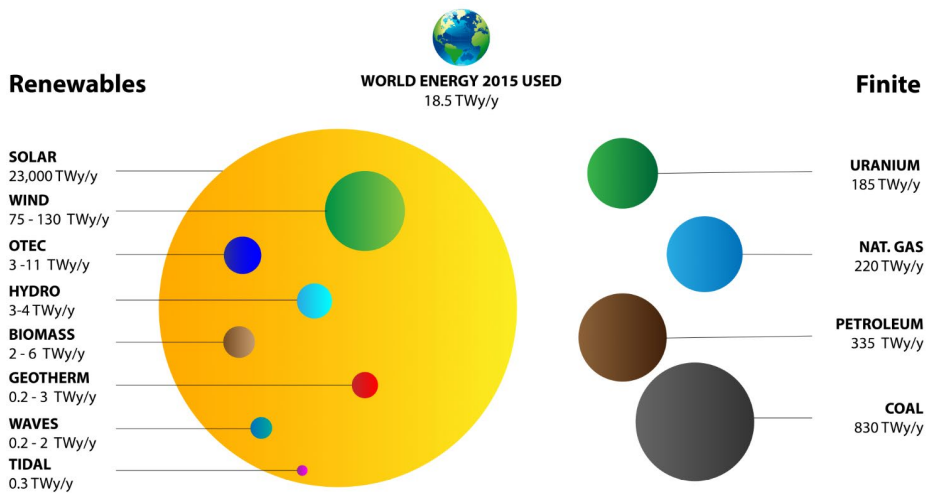


Figure 1.2. 2015 estimated finite and renewable planetary energy reserves (Terawatt-years). The volume of each sphere represents either the yearly potential energy (renewable energy sources), or the estimated total recoverable energy remaining in 2015 (finite energy sources). Adapted from reference.⁴

Solar energy is the most abundant of the renewable sources and photovoltaic (PV) technology, the direct conversion of sunlight into electricity, is becoming more cost competitive. The World Economic Forum predicts that solar photovoltaic infrastructure will have a lower levelized cost of electricity (LCOE, i.e. total cost of building and operating an energy-generating plant, divided by the total energy output) than coal or natural gas electricity generation throughout the world by 2020.⁵ Nowadays, the PV technology is dominated by silicon solar cells, also called ‘first generation’ solar cells. Silica (silicon oxide, SiO₂) is an abundant and non-toxic material, but it requires a substantial energy consumption to be processed into high purity crystalline silicon, increasing the energy payback time of the solar cell (the payback time is the time an energy source needs to be running in order to generate the amount of energy used for its production).

For silicon solar cells the energy payback time is estimated to be approximately eight years.⁶ Conventional solar silicon technology presents a theoretical limit of 29% power conversion efficiency (PCE). The typical silicon solar panels have efficiencies around 20%, and the record silicon solar cells have an efficiency of 26.7% on a lab scale⁷, meaning that the silicon-based PV is reaching its efficiency limit. In order to improve the efficiency/cost relation of solar panels, alternative materials that are abundant, inexpensive and with similar efficiency as silicon have been investigated. These materials, included in so-called ‘second-generation’ solar cells, may be used as single junction solar cells to replace crystalline silicon, or in multi-junction (tandem) solar cells. GaAs, GaInP, GaInAs and Ge thin films semiconductor devices are competitors to established silicon solar cells. GaAs has reached the record efficiency for a single junction solar cell of 27.6%,⁸ however, these cells are rather expensive due to the cost of the starting materials and the device processing. Other important PV technologies are based on cadmium telluride (CdTe) and copper indium gallium selenide (CIGS). CdTe solar cells have reached 22.1% conversion efficiency⁹ and a low payback time¹⁰ but the toxicity of cadmium and the usage of rare materials are still limiting factors for a large scale deployment of this technology. The efficiency of CIGS and CIS solar cells are also high, 22.9% and 23.4% respectively.¹¹ Despite these promising data, however, the market share of thin-film solar cells remains below 10-15%, mainly because of the very low price of silicon solar modules. The ‘third-generation’ solar cells consists of thin-film semiconductors that can be processed through more simple methods, such as spin-coating, blade coating or inkjet printing and thermal vacuum-deposition techniques. These deposition techniques can be used in view of the very different nature of the semiconductors used, such as organic small molecules, polymers, and inorganic quantum dots.¹²

The performance of organic PVs has been steadily increasing over the past few years due to significant innovations in the material engineering. To date, the record PCE values for bulk heterojunction organic solar cells exceed 17% for single-junction and tandem devices.^{13,14} Also dye-sensitized solar cells (DSSCs) have been widely studied, with the first efficient devices reported in the early 90's with a PCE of about 8%.¹⁵ Even if over the years their efficiency has improved, these solar cells present important drawbacks such as the use of rare metals and a liquid electrolyte, which limits the solar cells lifetime.¹⁶ DSSCs have eventually evolved in favor of a more promising technology based on semiconducting, hybrid organic –inorganic perovskites. Efficient perovskite solar cells can be fabricated through simple methods, and are compatible with large-area and flexible devices. Unlike silicon, perovskites are direct bandgap semiconductors with a very high absorption coefficient, enabling quantitative light absorption in films as thin as 500 nm. This feature would enable the fabrication of lightweight PVs. The effective solar absorption of perovskites is clearly visible from the absorption coefficients comparison of different solar absorbers in **Figure 1.3**.

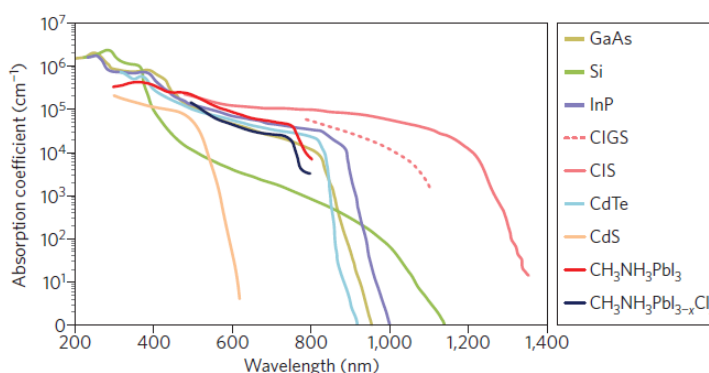


Figure 1.3. Absorption coefficient of perovskites $\text{CH}_3\text{NH}_3\text{PbI}_3$ and $\text{CH}_3\text{NH}_3\text{PbI}_{3-x}\text{Cl}_x$ compared to other solar cell materials. Adapted from reference.¹⁷

Another aspect that makes perovskites rather unique semiconductors is the possibility of profoundly altering their properties upon simple variation of their composition. Lead halide perovskites were first reported in solar cells in 2009, with a 3.8% power conversion efficiency,¹⁸ and the vibrant research over the last decade has made perovskite PV the fastest advancing solar technology so far, reaching an efficiency of more than 25% (**Figure 1.4**) in only 10 years of development. Perovskite solar cells are now among the most efficient thin-film photovoltaic technology and this make them a strong candidate for commercial implementation. Different start-up companies are trying to commercialize this technology as single junction and tandem solar cells.

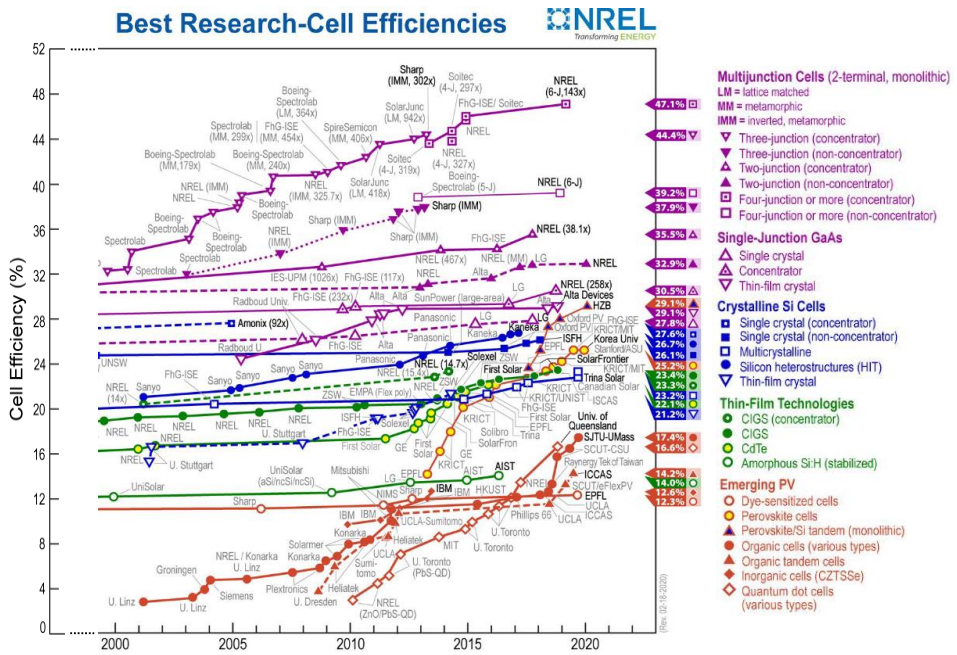


Figure 1.4. Best research-cell efficiency chart - NREL¹⁹

With their good optoelectronic properties, perovskites find a number of other applications beyond photovoltaics, such as photodetectors, memresistors, X-ray detectors, light-emitting diodes (LEDs), etc. Among these, LEDs are particularly attractive in view of the versatile and tunable optoelectronic properties of perovskites. Lighting was the first application offered by gas and electric utilities, and continues to be one of the largest use of produced electricity. In 2005 it was estimated that electric lighting used 19% of all global electricity consumption²⁰, with obvious impact on greenhouse gas emissions. Within this perspective, it is clear that to meet the global energy demand and at the same time reduce greenhouse gas emissions, we have to find ways not only to generate energy efficiently, but also to more efficiently consume it. Reducing energy consumption by enhancing the efficiency of light sources is thus a major route towards CO₂ reduction. In this direction, researchers are evaluating the potential of perovskites to increase the efficiency of LEDs which, in the last four years, has exponentially increased from 0.1% to more than 20% external quantum efficiency (EQE_{EEL})^{21–24} (see Operating principle of light-emitting diodes and Equation 1.16 for details).

1.2 Perovskite

The archetype perovskite is the mineral calcium titanate (CaTiO₃), discovered in 1839 by Gustav Rose in Russia and named after the mineralogist Lev Perovskiy. The same nomenclature is given to any material sharing the same type of crystal structure, with ABX₃ being the general chemical formula. In this structure the cation A is larger than the cation B, while X is a monoatomic anion. Several element of the periodic table can be accommodated in this structure, making perovskites a versatile family of compounds. The “ideal” perovskite definition refers to the cubic crystal structure (i.e. CaTiO₃), which is composed

of a three-dimensional framework of corner-sharing BX_6 octahedra. The A-site cation fills the 12 coordinate cuboctahedral cavities formed by the BX_3 network and is surrounded by 12 equidistant anions, as shown in **Figure 1.5**.

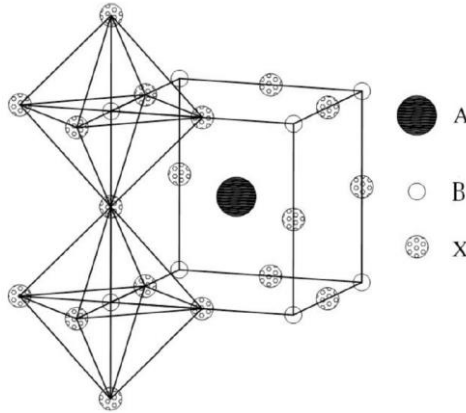


Figure 1.5. Ideal perovskite-type structure ABX_3 with corner-shared octahedron BX_6 , extending in three dimensions to form the framework.²⁵

A cubic perovskite can transform into other crystal structures through tilting of the octahedral BX_6 , which can be induced by changing the elemental composition (A, B and X). These resulting structures are however closely related to the cubic one and likewise belong to the perovskite family structure. There are several structural deviations from the ideal cubic perovskite, i.e. tetragonal, orthorhombic, rhombohedral, monoclinic and triclinic structures. The structural stability of perovskite-type compounds can be predicted using simple geometrical considerations, using the “tolerance factor” t (equation 1.1) as expressed by Goldschmidt in the early 1920s²⁵

$$t = \frac{r_A + r_X}{\sqrt{2}(r_B + r_X)} \quad (1.1)$$

where r_A , r_B and r_X are the ionic radii of the corresponding ions. In other words, the tolerance factor is defined as the ratio of the distance A-X to the distance B-X in an idealized solid-sphere model. Up to now, almost all known perovskites have t values in the range $0.75 < t < 1.1$. Goldschmidt's tolerance factor t is not by itself sufficient to predict the formation, or not, of the perovskite structure. For this a reason the "octahedral factor" μ (equation 1.2) was introduced²⁵

$$\mu = r_B/r_X \quad (1.2)$$

Generally, μ is in the range $0.44 < \mu < 0.90$ for halide perovskite ($X = F, Cl, Br, I$). The octahedral factor is related to a specific combination of B cations and X anions to form stable octahedra. Although the majority of perovskites are oxides or fluorides, halides, sulphides, hydrides, cyanides, oxyfluorides and oxynitrides are also reported. This variety of composition, together with their possible structural distortion, results in diverse physical/chemical properties. Indeed, perovskites can exhibit semiconducting, superconducting, piezoelectric, ferroelectric, dielectric, magnetic, and catalytic properties.²⁶

1.2.1 Three dimensional (hybrid) organic-inorganic perovskite

Three-dimensional (3D) hybrid perovskites that have properties making them interesting for optoelectronics application are base on divalent metals and halides. These metal halide perovskite can be described by the same general formula ABX_3 presented before. The most used consist of divalent metal ions such as lead (Pb^{2+}) or tin (Sn^{2+}), which occupy the B-site surrounded by halides anion, *e.g.* iodide (I^-), bromide (Br^-) or chloride (Cl^-), at the X-site, creating a 3D anionic network of corner-sharing octahedra. The most common A-side cations are monovalent organic cation such as methylammonium (MA: $CH_3NH_3^+$),

formamidinium (FA: $\text{CH}_2(\text{NH}_2)_2^+$) and, in the case of fully inorganic perovskites, cesium (Cs^+), as they fit in the cavity delimited by four corner-sharing octahedra (BX_6) (see **Figure 1.5**). The benefit of organic ammonium cations such as MA and FA with larger radii (0.18 nm and 0.19-0.22 nm, respectively) compared with inorganic cations such as Cs^+ (0.167 nm) resides in a more stable perovskite structure, with a tolerance factor close to 1. I^- , Br^- and Cl^- have ionic radii of 0.220 nm, 0.196 nm, and 0.181 nm, respectively. As highlighted in **Figure 1.6**, where the calculated tolerance factor for a series of halide perovskites is shown, replacing Pb with Sn increases t , enhancing the geometrical stability of the structure. However, the use of Sn results in less chemically stable compounds, as Sn(II) is readily oxidized to the more stable Sn(IV) species.¹⁷

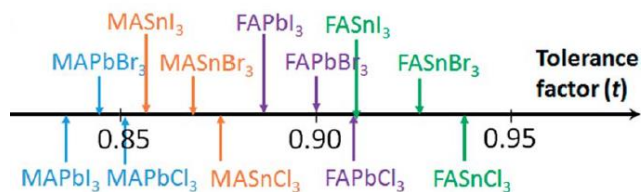


Figure 1.6. Tolerance factors t of a series of hybrid halide perovskites. Adapted from reference²⁷

For a given composition, the perovskite structure will undergo different phase transitions as a function of the temperature. In the case of $\text{CH}_3\text{NH}_3\text{PbI}_3$ (MAPbI_3 in **Figure 1.6**), there are two different phase transition at 162K and at 327K.

The transition at lower temperature was assigned to a change from an orthorhombic to a tetragonal crystalline structure, while at higher temperatures the lattice changes from a tetragonal to a cubic structure.²⁸ The first report on semiconducting metal halide perovskite was published in 1957, when the photoconductivity in all-inorganic CsPbX_3 systems was observed.²⁹

In 1978, Weber replaced Cs^+ with CH_3NH_3^+ and obtained hybrid perovskites with interesting physical properties: he prepared $\text{CH}_3\text{NH}_3\text{PbX}_3$ compounds of different colors (ranging from colorless to black) by changing the halide composition,³⁰ introducing one of the key properties of these materials i.e. the simple tuning of their optical bandgap.

1.2.2 Low dimensional (hybrid) organic-inorganic perovskite

The first research on layered metal based perovskites (i.e. Cu^{2+} and Cr^{2+} metals) were focused on their magnetic properties.³¹ Only in the late 1990s, the B-site cations were changed from the transition metals to the group 14 metals. This yielded semiconducting perovskites with direct bandgap that are of interest in optoelectronics. The first report on layered group 14 hybrids halide perovskites with organic cations was reported in 1986 by Marayama et al.³² When the A-site organic cation is too large to fit within the cavity delimited by the octahedral framework typical of 3D perovskites, the structure collapses into a low dimensional material formed by inorganic sheets of corner sharing BX_6 octahedra separated by organic layers. In this situation the tolerance factor t is much larger than 1.1. This new phase is termed two-dimensional (2D) perovskite and is described by the general formula $(\text{R-NH}_3)_2\text{BX}_4$ where the B-site is occupied by a metal cation, generally Pb^{2+} or Sn^{2+} and the X-site by the halide anion I^- , Br^- or Cl^- . The separation between the inorganic slabs occurs due to the R-NH_3 group which represents a bilayer of aliphatic or aromatic mono-ammonium cations, or a single layer of diammonium cations (**Figure 1.7**).^{33,34}

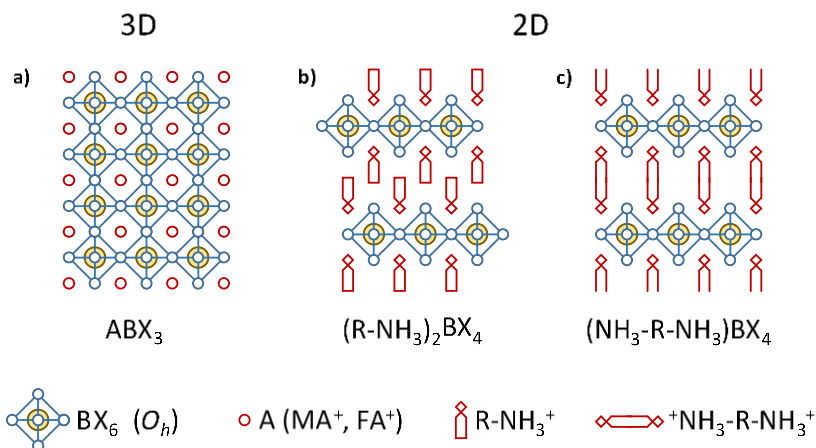


Figure 1.7. Schematics representations of a) 3D perovskites with the general formula ABX_3 , and of 2D perovskites with b) mono-ammonium or c) diammonium organic cations. Adapted from reference³³

The organic group $R-NH_3$ in the 2D perovskites binds to the halogen atoms of the inorganic framework with the terminal cationic groups by hydrogen bonding. The organic groups self-assemble via $\pi-\pi$ interaction when the organic cations contain conjugated groups or through Van der Waals force when they contain non-aromatic substituents. The layered perovskite family is not restricted solely to this structure, as intermediate structures with inorganic sheets of varying thicknesses can be prepared by using both small A-site cations (analogous to those described in the previous paragraph) and large organic cations ($R-NH_3$). In the so-called Ruddlesden-Popper perovskites with formula $(RNH_3)_2(A)_{n-1}B_nX_{3n+1}$ the thickness of the inorganic layers can be tuned by changing the ratio of small and large cations. The dimensionality increases with increasing n , that indicate the number of octahedral sheets comprised in a single inorganic slab,³⁵ see **Figure 1.8**.

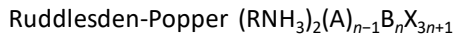
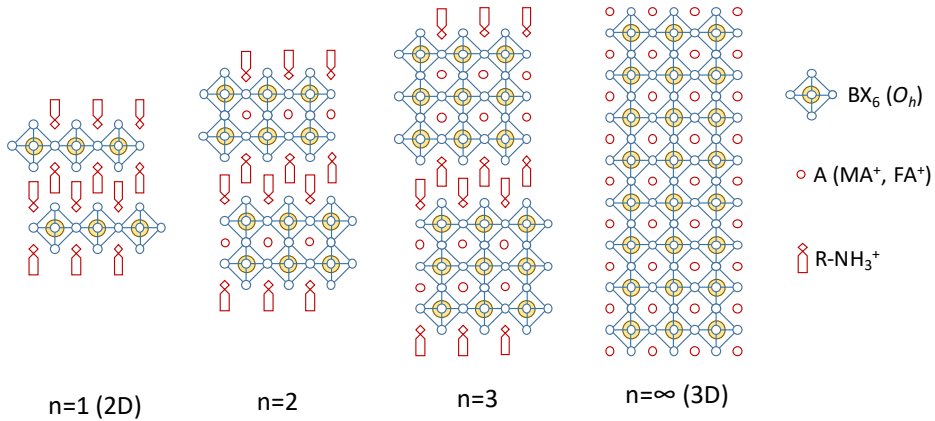


Figure 1.8. Schematic representation of [001] oriented layered Ruddlesden-Popper perovskites, where n defines the thickness of the perovskite sheets.

For $n = 1$, the material is a pure 2D perovskite, while when $n \rightarrow \infty$ the structure is a 3D perovskite. The first reports of Ruddlesden-Popper perovskite with $n > 1$ was published in the 1990s.³⁶ About 20 years later, and few years following the first report of solar cells employing 3D hybrid metal halide perovskites by Miyasaka et al¹⁸, the first solar cell based on a Ruddleson-Popper perovskite with $n = 3$ as absorber was reported by the Karunadasa group.³⁷

1.3 Properties of perovskite semiconductor

Hybrid perovskite are semiconductors with a direct bandgap and the energy bands depicted in **Figure 1.9**. The valence band (VB) is the energy band where all the valence electrons are normally present, while the conduction band (CB) is the empty energy band with higher energy in which electrons can move freely inside the material.

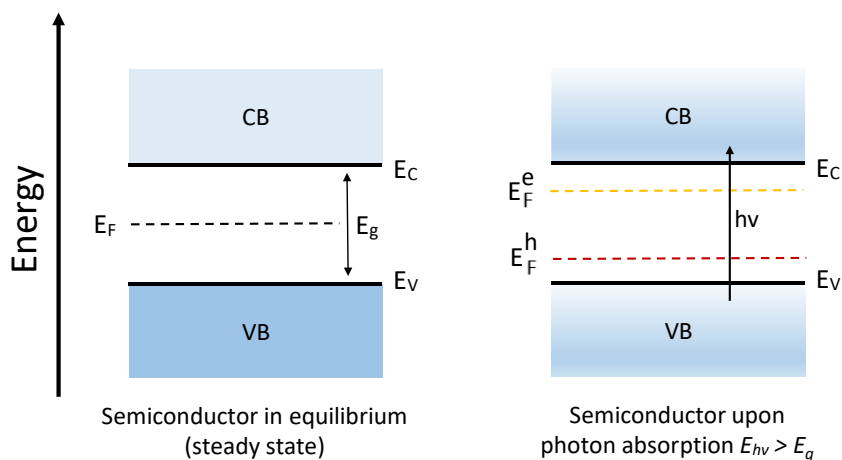


Figure 1.9. Schematic energy bands for an intrinsic semiconductor in equilibrium and upon photon absorption.

The two bands are separated by the bandgap (E_g), a forbidden energy region where no electron states can exist. In an intrinsic semiconductor as perovskite, the Fermi level lies in the middle of the bandgap in steady state condition, as shown in **Figure 1.9**. The light absorption of the perovskite and of all semiconductors depend on the bandgap of the material and only photons with energy equal or higher than the bandgap can be absorbed. Once a photon is absorbed, the electron is excited from the VB to the CB leaving positive charge (hole) in the valence band. These holes can move freely in the valence band and contribute to the conductivity of the material. When photons with higher energy than the bandgap are absorbed they generate charge carriers that have excess thermal energy which they quickly lose as heat to the lattice, in a process known as thermalisation. After photon absorption and a fast thermalization within the bands, two separate quasi-Fermi levels for electrons (E_F^e) and holes (E_F^h) are formed (**Figure 1.9**). The difference between E_F^e and E_F^h is the quasi-Fermi level splitting (QFLS), which defines an upper limit for the voltage a solar cell can generate.

Recombination of electrons and holes in a semiconductor takes place through different mechanisms (**Figure 1.10**).

Radiative recombination

Radiative recombination is the process where an electron from the conduction band relaxes to the valence band and recombines with a hole, releasing energy as a photon. This recombination is also called bimolecular because it involves two free carriers in a band-to-band transition. This is the most important recombination mechanism to achieve high electroluminescence efficiency in LEDs. On the other hand, radiative recombination is also unavoidable in a solar cell, where it helps maintaining a high photovoltage if non-radiative recombination is suppressed.

Non-radiative recombination (Shockley-Read-Hall)

In this recombination mechanism an electron or a hole are captured by trap states within the bandgap, and hence it is also known as trap-assisted recombination. These trap states can be surface defects or deep level traps, and are created by impurities and disorders in the perovskite crystal lattice. It is a monomolecular recombination that involve one free carrier at a time and two steps. Firstly, an electron or a hole is trapped and then once a carrier of opposite charge comes in the proximity of the same trap the non-radiative recombination occurs. It is important to minimize the trap-states and as consequence the non-radiative recombination losses that are detrimental for electroluminescence in LEDs and for charge density and extraction in perovskite solar cells.

Non-radiative Auger recombination

Auger recombination is a three-body process. An electron in the conduction band recombines with a hole in the valence band, but instead of emitting a photon, the

energy is transferred to another electron in the conduction band. This excites the electron into a higher energy level within the conduction band, as shown in **Figure 1.10**. Eventually the electron relaxes back to the conduction band edge releasing energy as heat to the environment. Because it is a three-body collision, this mechanism is important when carrier densities are very high, i.e. at high temperature, under strong illumination and in highly doped materials.

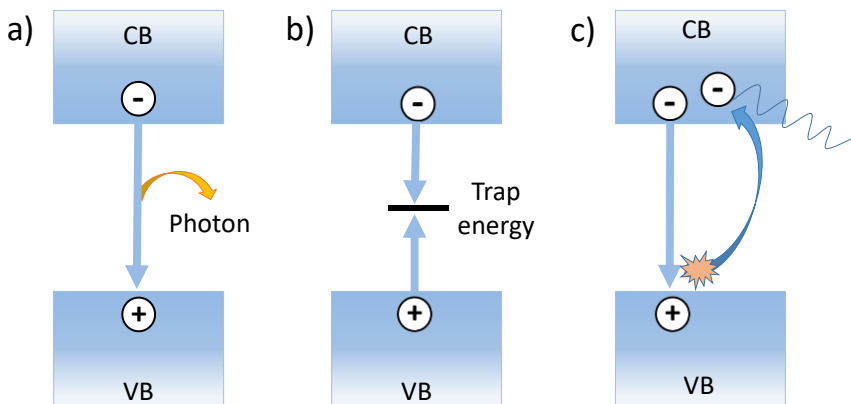


Figure 1.10. Scheme of different types of recombination a) radiative, b) non-radiative (trap-assisted), c) non-radiative (Auger recombination)

In a solar cell the recombination should be prevented in order to maximize the charge collection at the electrodes. In a LED the non-radiative recombination should be avoided to enhance the electroluminescence efficiency. Other two important parameters closely linked with recombination are the carrier lifetime and diffusion length. The lifetime of an electron or a hole is the average time that a carrier can exist before it recombines.

The carrier lifetime takes into account the three types of recombination:

$$\frac{1}{\tau} = \frac{1}{\tau_{Rad}} + \frac{1}{\tau_{SRH}} + \frac{1}{\tau_{Aug}} \quad (1.3)$$

The carrier diffusion length L is the average distance a carrier can move before it recombines and it depends on the carrier lifetime τ and on the diffusivity D as shown in the equations (1.4)

$$L_n = \sqrt{D_n \tau_n} \text{ for electrons} \quad L_p = \sqrt{D_p \tau_p} \text{ for holes} \quad (1.4)$$

With longer diffusion length, carriers can move a longer distance before they recombine and thus are more likely to be collected contributing to the photocurrent in a solar cell. For this reason, in device fabrication it is important to take into consideration the thickness of the active material, which should not exceed the carrier diffusion length.

1.4 Optical and structural properties of metal halide perovskites

In a hybrid metal halide perovskite, the valence band is formed predominantly by a mixture of metal s-orbitals and halide p-orbitals, while the conduction band minimum (CBM) is composed mainly of metal p-orbitals. Increasing the ionic character of the B-X bond by increase the halide electronegativity, going from I to Br to Cl, selectively lowers the energy of the VB. Moreover, the energy of the CB, influenced by the metal Pb p-orbitals, is shifted upward when the Pb-X distances decrease going from I to Br to Cl, due to a more confined electron on a Pb atom. The consequence of the upward shift of the CBM and the downward shift of the valence band maximum (VBM) is the

increase of the band gap with increasing halide electronegativity. As a consequence, by exchanging or mixing different B, and/or X ions, it is possible to tune the optical gap at will, targeting different optoelectronic applications. The band-gap of the archetype compound methylammonium lead triiodide (MAPbI₃) of 1.6 eV can be widened by complete substitution with bromide (MAPbBr₃, 2.3 eV) and chloride (MAPbCl₃, 3 eV), as generalized for several other compositions in the schematic energy level diagram in **Figure 1.11**.

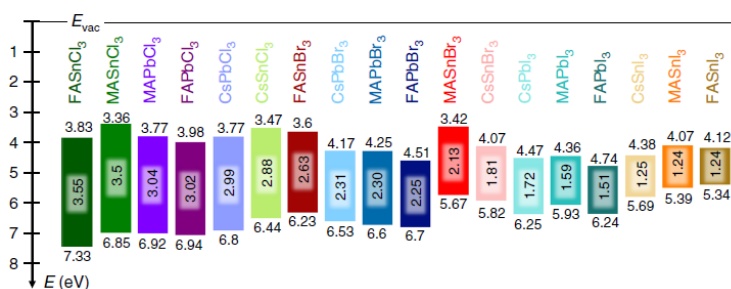


Figure 1.11. Energy level diagrams of several 3D metal halide perovskites ³⁸

The metal substitution has consequences for the optical bandgap of the perovskite. Replacing Pb with Sn shifts upward both the VB and CB, due to the smaller electronegativity and lower i) ionization potential and ii) electron affinity of the Sn. However, the main contribution comes from the metal s-orbitals, and as a result the VB shifts to a higher energy than the CB, and this causes to a reduction of the band gap for Sn perovskites. The A-cation type also affects the bandgap of the perovskite via its effect on structural deformations that reduce the hybridization between the metal s-orbitals and the halide p-orbitals. This effect leads to a downward shift of the VB and a decrease of the band-gap with higher volume A-cations, i.e. changing from Cs to MA to FA.³⁸ Apart from the complete substitution of a specific ionic component in the perovskite structure,

also the partial substitution of different ions and in particular different halide permit to further and continuously tune the absorption onset through the whole visible spectra. A perfect example is given by the archetypal and most studied 3D MAPbX₃ (**Figure 1.12**)

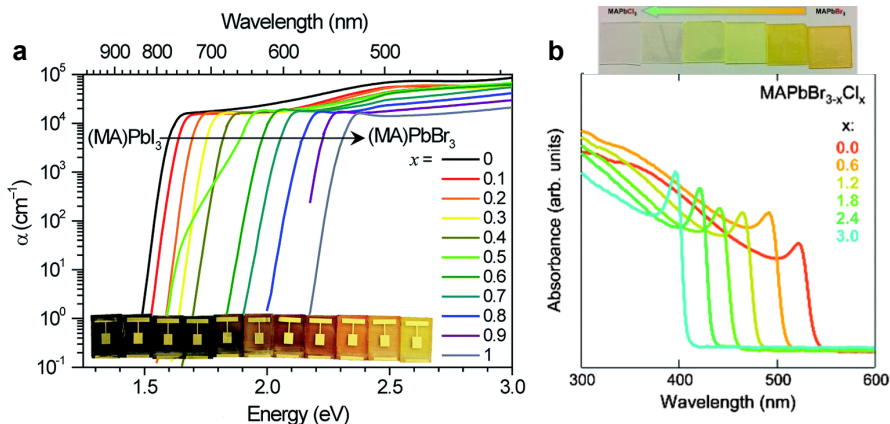


Figure 1.12. a) Absorption coefficient of mixed MAPb(I_{1-x}Br_x)₃ perovskite thin films with increasing bromide content and photos of the samples.³⁹ b) Absorption spectra of mixed bromide-chloride perovskite films with increasing chloride content and photos of the corresponding samples.⁴⁰

By increasing the bromide content in the MAPb(I_{1-x}Br_x)₃ perovskite the absorption edge is shifted to higher energy (**Figure 1.12a**) and the same happens when the chloride content is increased in the MAPb(Br_{1-x}Cl_x)₃ perovskite (**Figure 1.12b**), tuning the absorption from the green to the blue spectral region. From the absorption profile of the perovskites with different halide content it is possible to note that the absorption edge shape changes when going from a 3D perovskite rich in iodide to one with more bromide and/or chloride.

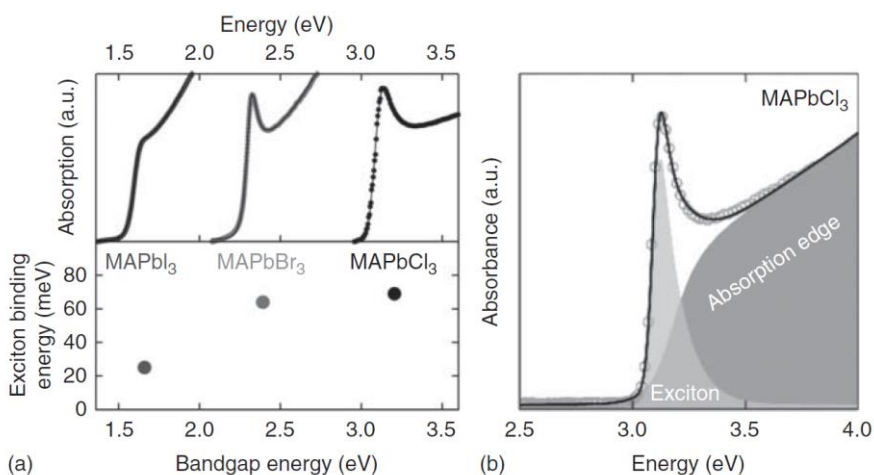


Figure 1.13. a) Top panel, absorption spectra for 3D lead halide perovskites at room temperature. Bottom panel, exciton binding energy as a function of the energy bandgap of the respective materials.⁴¹ b) Absorbance of MAPbCl₃ as a function of energy with two-component (exciton and band-to-band absorption) fit overlaid.⁴⁰

The MAPbI₃ display an absorption edge with band-to-band electronic transition. On the other hand, moving to MAPbBr₃ and then MAPbCl₃ the band edges are dominated by a pronounced excitonic transition. These different profiles are related to different exciton binding energies (E_b) of those perovskites. Moving from I to Br and Cl the stronger ionic character of the Pb-X bond leads to an augmented E_b which is reflected in the increased excitonic component of their optical absorption peak (**Figure 1.13a**). However, the optical absorption profile of the 3D MAPbBr₃ and MAPbCl₃ is constituted by both excitonic and band-to-band transitions (**Figure 1.13b**).

The structure of the 2D perovskites with alternating organic and inorganic layers confer them other peculiar optical and electronic properties. They present a multiple-quantum-well structures where the inorganic layers are the semiconducting wells and the organic layers are the insulating barrier (**Figure**

1.14). This leads to an anisotropic quantum and dielectric confinement along the [001] direction. The dielectric confinement is due to the dielectric mismatch between the organic and the inorganic framework ($\epsilon_{\text{org}} < \epsilon_{\text{inorg}}$).⁴² As a consequence of this confinement, photogenerated electrons and holes spontaneously form excitons that are confined in the metal halide wells. These excitons possess a binding energy in the order of hundreds of meV, at least an order of magnitude higher than the exciton binding energy of 3D perovskite (tens of meV).⁴³

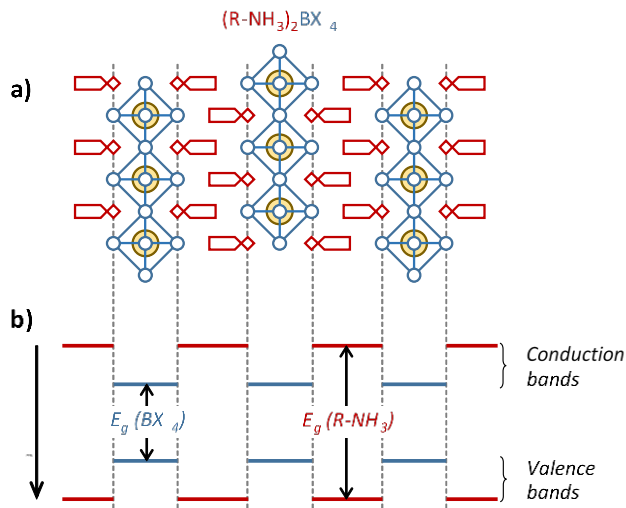


Figure 1.14. a) schematics 2D perovskites structure and b) 2D perovskite flat band energy diagram where the metal halide semiconducting sheet has much lower bandgap than the organic layer.³³

The high exciton binding energy of 2D perovskites is reflected in the characteristic excitonic transition dominating their optical absorption profile. As for 3D materials, the optical bandgap can be tuned by partial or complete halide substitution (**Figure 1.15**).

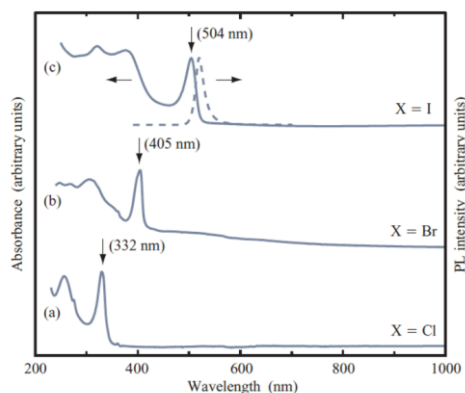


Figure 1.15. Room temperature absorption spectra of $(\text{C}_4\text{H}_9\text{NH}_3)_2\text{PbX}_4$ with a) $\text{X} = \text{Cl}$, b) $\text{X} = \text{Br}$, c) $\text{X} = \text{I}$. In curve (c), the corresponding photoluminescence (PL) spectrum is indicated by the dashed curve.³³

Figure 1.15 shows how the excitonic absorption of butylammonium lead halides $(\text{C}_4\text{H}_9\text{NH}_3)_2\text{PbX}_4$ can be shifted from green to blue and to the ultraviolet region of the electromagnetic spectrum by substitution with I, Br and Cl, respectively. The narrow excitonic PL signal with small Stokes shift (~ 15 nm) with respect to the absorption for the iodide compound is also reported.

It is important to underline that in contrast to 3D perovskites, 2D perovskites have less restrictions towards the size of the cations that can be accommodated between the inorganic sheets. This gives an additional degree of freedom in the compositional design of these compounds. Some examples of large organic amines used as precursors for the cations (R-NH_3) that have been employed to form 2D perovskites are reported in **Figure 1.16**.⁴³

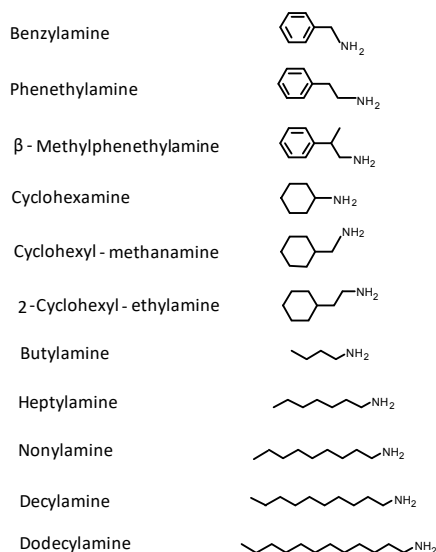


Figure 1.16. Different aliphatic and aromatic organic amines R-NH₂ employed as precursors in the formation of hybrid perovskite 2D (R-NH₃)₂BX₄. Adapted from references^{44,45}

Although the properties of the excitons in 2D perovskites are mainly determined by the nature of the inorganic framework, the energy of the exciton absorption and PL peaks are also influenced by the organic spacers.⁴⁴ The organic component can alter the metal–halide–metal bond angle and hence induce changes in the exciton binding energy and in the electronic band structure.⁴⁵ The organic cation parameters that can be modified in order to tune the optical and electronic properties in 2D perovskites are the following: i) the interactions between organic moieties, ii) the length of the alkyl chain (CH₂)_n of the spacer (R-NH₃), iii) the steric hindrance of R and viii) its structural flexibility. Moreover, a significant contribution to the material properties is related to the dielectric constant of the organic cations which will change the dielectric confinement.

For instance, employing aromatic groups with a more polarizable electron density and higher dielectric constant compared to aliphatic molecules, lead to a smaller exciton binding energy.^{46,47} All these properties, which can be controlled by chemical design, make 2D perovskites interesting candidates for optoelectronic and in particular for lighting applications. On the other hand, the typically wide bandgap, the high E_b and the anisotropic transport of pure 2D $(R-NH_3)_2BX_4$ perovskites are not optimal features for photovoltaics. As previously mentioned, hybrid perovskite thin films can be deposited through simple solution-processing of inexpensive organic and inorganic salts at low temperature. This is also true for 2D $(R-NH_3)_2BX_4$ perovskite thin films, which are typically highly crystalline even when prepared simply by spin-coating solutions of their precursors (**Figure 1.17**).

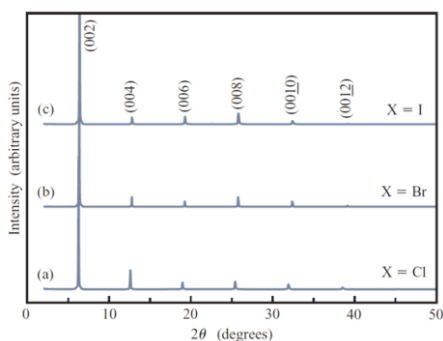


Figure 1.17. XRD patterns of spin-coated thin-films of $(C_4H_9NH_3)_2PbX_4$ with a) $X = Cl$, b) $X = Br$, c) $X = I$. The reflections indexes are reported for the iodide compound and are the same for the other halide analogues.³³

In general, solution-coated films show intense (001) reflections in their X-ray diffraction patterns (XRD), suggesting that 2D perovskites are oriented along the c -axis, with alternating PbX_6 inorganic sheets and organic bilayers parallel to the substrate's plane. This implies that the insulating sheets of organic cations are

perpendicularly oriented to the direction of the electric field (in a thin-film device configuration), hindering charge transport. At the same time, the high E_b limits the interconversion of excitons into free carriers, reducing the charge carrier mobility in pure 2D perovskites. One way to modify E_b is by increasing the thickness of the inorganic slabs, as in 2D Ruddlesden–Popper perovskites. Using a combination of optical spectroscopy and modeling, it was demonstrated how E_b decreases from 470 meV to 125 meV with increasing thickness from $n = 1$ to $n = 5$ (**Figure 1.18**). In support of this data an interesting experimental demonstration of the interconversion between bound excitons and free charges was carried-out by combining microwave photoconductivity and theoretical calculations. In that study was demonstrated that the free charges increases with the thickness of the 2D perovskite and thus increase also the mobility.⁴⁸

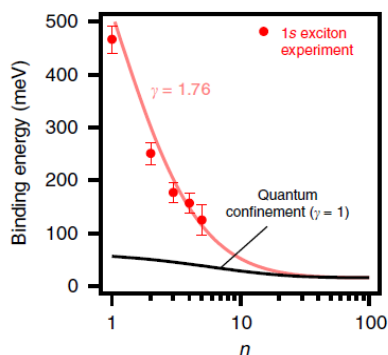


Figure 1.18. Tuning of exciton binding energy of exciton ground state as a function of n .⁴⁹

The use of the quasi-2D Ruddlesden–Popper phases rather than pure 2D perovskites offers also a pathway to address unfavorable crystallographic orientation in thin films. Indeed, as soon as the inorganic layers become thicker

($n > 1$), the small organic cations has been shown to foster the perovskite growth in the vertical direction with respect to the substrates, favoring charge transport in thin film optoelectronic devices.⁵⁰

1.5 Operating principle of photovoltaic devices

Perovskite solar cells are multilayer devices in which the perovskite film absorbs light (photons with an energy equal to or larger than the bandgap), creating holes and electrons pairs which are separated, selectively extracted by (organic) semiconductor materials, and collected at the electrodes.

The sun emits a broad spectrum of electromagnetic radiation (from UV to infrared) which above atmosphere is very close to that of a black body at approximately 5800 K. When going through the atmosphere, the solar spectrum is altered due to absorption processes by ozone (O_3) in the UV, O_2 and H_2O in the visible and near-IR regions. Those absorptions depend also on the distance the sunlight has to travel through the atmosphere and on the incidence angle. For this reason the solar spectrum is described in term of air mass (AM) that the light has to pass through. Conventionally the solar spectrum used as a reference for photovoltaic measurements is defined as AM 1.5 (see **Figure 1.19**), meaning that the light passes through 1.5 atmosphere thickness, which corresponds to a solar zenith angle of 48.2° . Moreover, for standard measurement conditions that allows to compare efficiencies from different laboratories, the solar cells are measured at one sun intensity (100 mW cm^{-2}) and at 25°C .

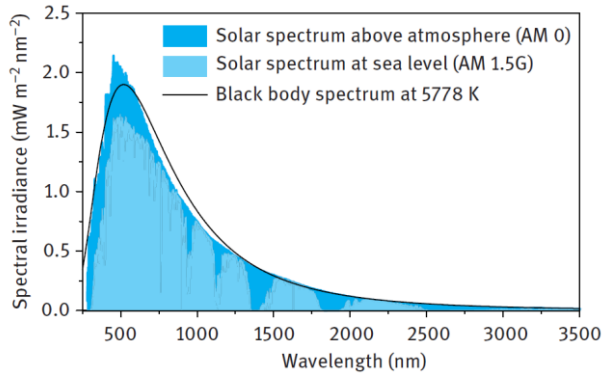


Figure 1.19. Comparison of the solar spectrum above the atmosphere with the solar spectrum at the sea level and with the black body radiation at 5778 K.⁵¹

The electrical power output P_{out} of a solar cell operated at a bias voltage V is given as

$$P_{out} = I \cdot V \quad (1.5)$$

where I is the current passing through the device at a given voltage. As the solar cell is typically a diode, this current is the sum of the diode dark current and the current that is generated by conversion of incident photons into electrons i.e. the photocurrent (J_{ph}).

In 1961, Shockley and Queisser analyzed the limits of photovoltaic energy conversion defining a model known as the *Shockley-Queisser limit* (SQ) which, among other parameters, defines the maximum possible efficiency of a solar cell as a function of the semiconductor bandgap⁵² (**Figure 1.20**). The SQ model includes different assumptions and defines four energy-loss mechanisms.

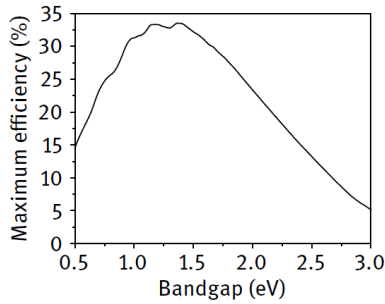


Figure 1.20. Maximum efficiency for a single-junction solar cell as a function of the absorber bandgap.

The two main losses comes from photons that are not absorbed (their energy is less than the semiconductor bandgap) and from thermalization of electron-hole pairs generated from photons with energy higher than the bandgap. Furthermore, the radiative recombination of electrons and holes and the isothermal loss (dissipation due to the electrical work of transferring a charge carrier from the absorber to the contacts) also diminish the maximum power conversion efficiency. A scheme of the energy-loss mechanisms is illustrated in **Figure 1.21**.

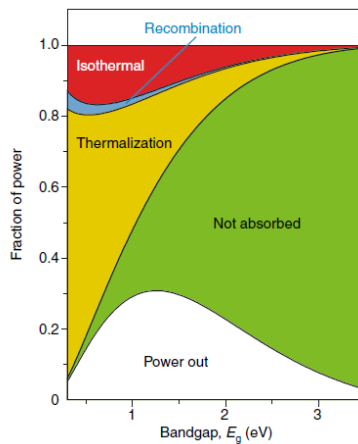


Figure 1.21. Power losses as a function of bandgap in the Shockley and Queisser limit.⁵³

However, in a real device not all the assumptions are fulfilled, and for instance less than one electron is generated per incident photon and not all the charge are extracted at the contacts. As a consequence, the photocurrent generation is best described in terms of the external quantum efficiency (EQE), that is the probability that a photon arrive on the cell, generates an electron-hole pair and charges are extracted at the contact under short-circuit conditions:

$$EQE = \frac{\text{number of photogenerated electrons per second}}{\text{numeber of incident photons per second}} \quad (1.6)$$

It is convenient to take in consideration also the absorption coefficient by mean of the internal quantum efficiency defined as

$$IQE = \frac{\text{number of photogenerated electrons per second}}{\text{numeber of absorbed photons per second}} \quad (1.7)$$

In order to characterize a solar cell, the current is measured while a bias voltage is applied to the device under illumination at 1 sun intensity. As a result, the characteristic current density versus voltage (J-V) curve is obtained. The J-V curve provides a wealth of information about the solar cell characteristic parameters, in particular the short circuit current (J_{sc}), the open circuit voltage (V_{oc}), the fill factor (FF), and the power conversion efficiency of the cell (PCE). The current density can be described by the classical Shockley equation for an ideal diode:

$$J(V) = J_0 \left[\exp\left(\frac{qV}{nk_B T}\right) - 1 \right] - J_{ph} \quad (1.8)$$

where J_{ph} is the photocurrent, V is the applied voltage, J_0 is the reverse saturation current density, q is the elementary charge, n is the ideality factor, k the Boltzmann constant and T the absolute temperature.

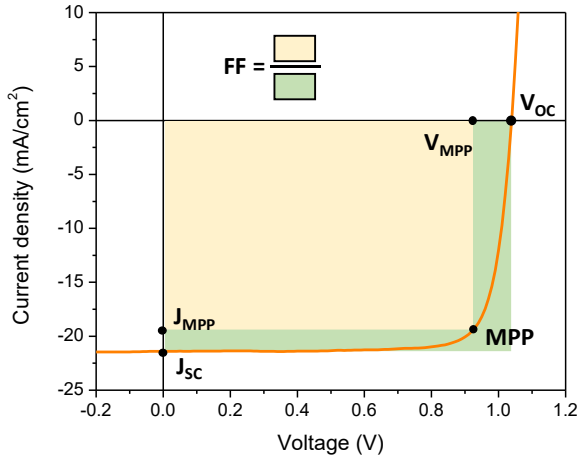


Figure 1.22. Schematic current density–voltage (J-V) curve labelled with the most important characteristic values.

The axis intercepts J_{sc} (typically expressed in mA cm^{-2}) in **Figure 1.22** indicate the current that flow at zero applied bias and it is a good approximation of J_{ph} in a well working solar cell. J_{sc} can be described with the following expression:

$$J_{sc} = q \int_0^{\infty} EQE(E) \Phi_{AM1.5}(E) dE \quad (1.9)$$

from which it is clear how the photocurrent J_{ph} and hence the short circuit current J_{sc} depend on the EQE and on the incident power (Φ_{AM} is the photon flux reaching the solar cell). A semiconductor with a small bandgap will absorb more photons and hence generate a larger current density compared to a wider-bandgap one under the same illumination.

The x axis intercept is the V_{oc} (V) that indicate the voltage at which there is no current flow. It represents the maximum available voltage from a solar cell and it is described by the equation:

$$V_{oc} = \frac{kT}{q} \ln \left(\frac{J_{sc}}{J_0} \right) \quad (1.10)$$

In contrast to J_{sc} , the open circuit voltage increases as the bandgap of the semiconductor increases, due to the larger potential energy of the photo-generated carriers. A parameter that defines the diode rectification from the J-V curve is the fill factor, FF. This measures the “squareness” of the J-V curve and is defined as the ratio of the maximum power point (MPP, product of the corresponding current density and voltage values, J_{MPP} , V_{MPP}), with the product of V_{oc} and J_{sc} (**Figure 1.22.**, equation (1.11))

$$FF = \frac{V_{MPP} \cdot J_{MPP}}{V_{oc} \cdot J_{sc}} \quad (1.11)$$

In reality, solar cells deviate from the ideal diode behavior due to series and shunt resistances, which reduce the FF of the J-V curve. In particular, the series resistance (R_s), which is related to the efficiency of charge transport and extraction within the diode, should be as small as possible. On the other hand, the shunt resistance (R_{sh}) should be as high as possible, as it is related to current leakage paths through the device, caused by defects such as pinholes. Hence the FF quantifies the efficiency of the charge transport and extraction in a solar cell, and that is hence influenced not only by the active material, but also by the device architecture. The power conversion efficiency (PCE) is the fraction of incident power (P_{in}) which is converted to electricity at the maximum power point.

Considering equation 1.11 the PCE is described as follow:

$$PCE = \frac{V_{MPP} \cdot J_{MPP}}{P_{in}} = \frac{V_{OC} \cdot J_{SC} \cdot FF}{P_{in}} \quad (1.12)$$

where usually the incident light power is 1000 Wm^{-2} from a AM 1.5G spectrum at a temperature of $25 \text{ }^\circ\text{C}$.

1.6 Operating principle of light-emitting diodes

Perovskite LEDs are multilayer devices in which a luminescent semiconductor is sandwiched between (organic) semiconducting layers that selectively inject electrons and holes in the active material. When the charges (electrons and holes) meet and recombine in the active layer, photons with an energy equal to the bandgap of the semiconductor are emitted. This process is known as electroluminescence. Perovskites exhibit properties of both organic and inorganic semiconductors, and a precise band diagram model for perovskite optoelectronic devices is not yet developed. As an approximation, perovskite LEDs can be described as p-i-n junctions, where the perovskite acts as an intrinsic semiconductor in between a hole (p-type) and an electron injecting layer (n-type), as illustrated in **Figure 1.23**. When no external voltage is applied and the electrodes are short-circuited, electron and holes need to overcome a potential barrier called built-in potential (V_{bi}), in order to move from one region to the other, as described in **Figure 1.23**.

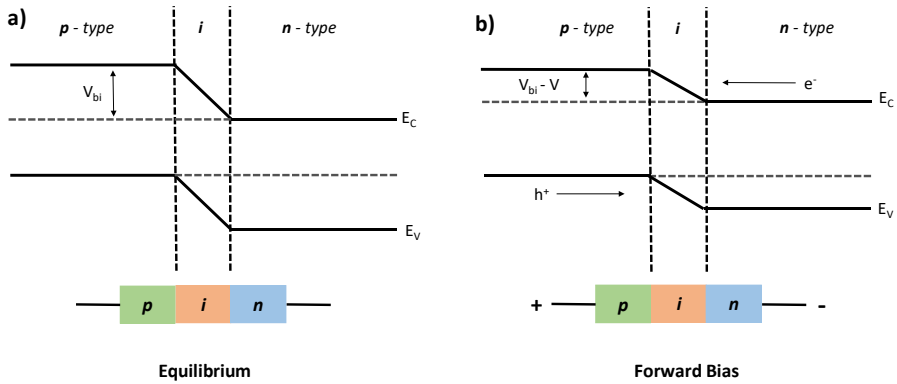


Figure 1.23. Schematic energy band-diagram of p-i-n junction diode under a) thermal equilibrium ($V = 0$) and b) forward bias ($V > 0$).

Upon the application of an external potential V in forward direction, when the p-type region is connected to a positive terminal and the n-type region is connected to a negative terminal, the potential barrier reduces ($V_{bi} - V$) (**Figure 1.23b**) and charge carriers diffuse into the device where they recombine leading to electroluminescence. In forward bias, the current density versus voltage (J - V) curve is characterized by three regimes (**Figure 1.24a**).

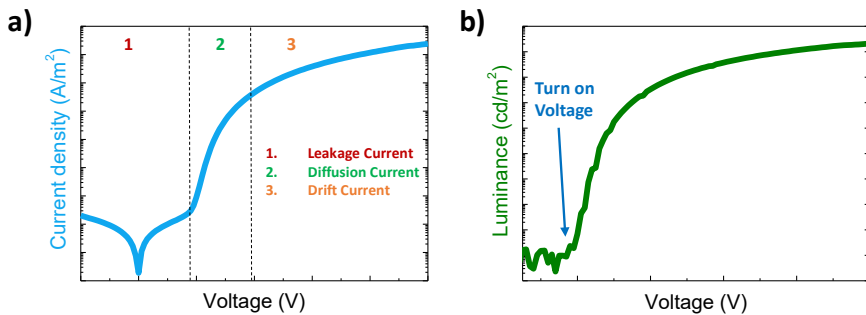


Figure 1.24. a) current density-voltage curve b) luminance-voltage characteristic of a perovskite LED.

In the low voltage regime (1, below V_{bi}) the leakage current is observed. This ohmic current is due to parasitic charge transport through pin-holes/defects in the device. In the second regime (2), where a small positive voltage V (lower than V_{bi}) is applied to the diode, electrons and holes diffuse into the intrinsic perovskite region, resulting in an exponential increase of the current density. This diffusion current can be expressed using the Shockley diode equation without the photocurrent (J_{ph}) contribution:

$$J = J_0 \left[\exp\left(\frac{qV}{nKT}\right) - 1 \right] \quad (1.13)$$

In the last regime (3), when a voltage higher than V_{bi} is applied, the electrons and holes are injected into the emissive active material and drift toward their counter electrodes. In this regime, the current is either injection- or space-charge-limited. As an example, if organic semiconductors are used as the p and n materials, they will have a lower mobility compared to the perovskite and this translate in a current saturation at high voltage due to charge accumulation. The electroluminescence characteristic of a LED can be quantified by measuring the luminance versus voltage (V-L) curve, as depicted in **Figure 1.24b**.

As highlighted from the curve, once the applied voltage V is close to V_{bi} , electron and hole recombination leads to light emission. Electroluminescence will be detected when the voltage overcame the injection barrier, at the so-called turn-on-voltage (V_{on}), which however depends also on the sensitivity of the photodetector used. The electroluminescence is expressed as luminance (cd/m^2), which represents the luminous power (expressed in candelas, cd) emitted by the device per unit area, and it is a photometric measurement because it takes into account the human eye sensitivity. The current density (A/m^2) depicted in **Figure 1.24a** corresponds to the current that is passing through the device per unit area.

In a light-emitting device, three different efficiencies are usually reported: current efficiency, power efficiency and external quantum efficiency. The current efficiency (cd/A) is the ratio between the luminance and the current density flowing through the device. The power efficiency (lm/W) is the ratio of luminous flux to power and it takes into account the current efficiency and the applied voltage. One lumen is the luminous flux emitted by an isotropic source that emit 1 candela for each solid angle of 1 steradian ($Lm = Cd \cdot sr$). To quantify how effectively a LED is emitting light, the internal quantum efficiency (IQE) and external quantum efficiency (EQE) are used. Internal quantum efficiency can be expressed as follows:

$$IQE = \gamma \cdot PLQY \quad (1.14)$$

where γ is the electron hole balance (carrier balance), and PLQY is the photoluminescence quantum yield (ration between emitted and absorbed photons). In actual devices, a significant proportion of generated light is reflected, transferred, and absorbed in both the active layers and the substrate, so it is necessary to also consider the outcoupling efficiency (ratio of generated to extracted light) to fully describe the losses in a LED.⁵⁴

The outcoupling efficiency strongly depends on the device geometry. In planar devices, it is mainly determined by the refractive index of the substrate n , and can be approximated by the expression:

$$\eta_{oc} = 1/(2n^2) \quad (1.15)$$

Hence the external quantum efficiency for electroluminescence (the measure of the number of photon leaving the device per injected electrons) can be expressed as follows:

$$EQE_{EL} = \frac{\text{number of photons emitted}}{\text{number of injected electrons}} = \gamma \cdot PLQY \cdot \eta_{oc} \quad (1.16)$$

This expression highlights the importance of maximizing the PLQY of a semiconductor in order to increase the efficiency of the corresponding LED. It is worth noting that equation 1.16 does not account for photon recycling effects in the semiconductor, which can also strongly alter (reduce) the final EQE_{EL} . The choice of suitable device structures and materials is also important to maximize charge injection yield and charge balance.

1.7 Solar cell and light-emitting device architecture

A perovskite solar cell in a planar configuration consists of a perovskite absorber layer sandwiched between two electrodes, one of which is transparent to allow the incoming sun light to reach the perovskite layer. A light emitting diode has a similar architecture but in this case the transparent electrode is needed for light out coupling from the device.

Both solar cells and LEDs are usually built on a transparent substrate (glass or plastic foil) coated with a transparent conducting oxide (TCO), usually indium tin oxide (ITO) or fluorine doped tin oxide (FTO). The perovskite is an ambipolar semiconductor (it can transport both electrons and holes). However, in order to build efficient devices and limit non-radiative charge recombination, hole and electron transport layers (HTLs and ETLs, respectively) are required. Two types of architecture have been developed, the p-i-n and n-i-p, whose names depends on the polarity of the transparent electrode. In this thesis p-i-n LEDs and solar cells (**Figure 1.25**) will be studied.

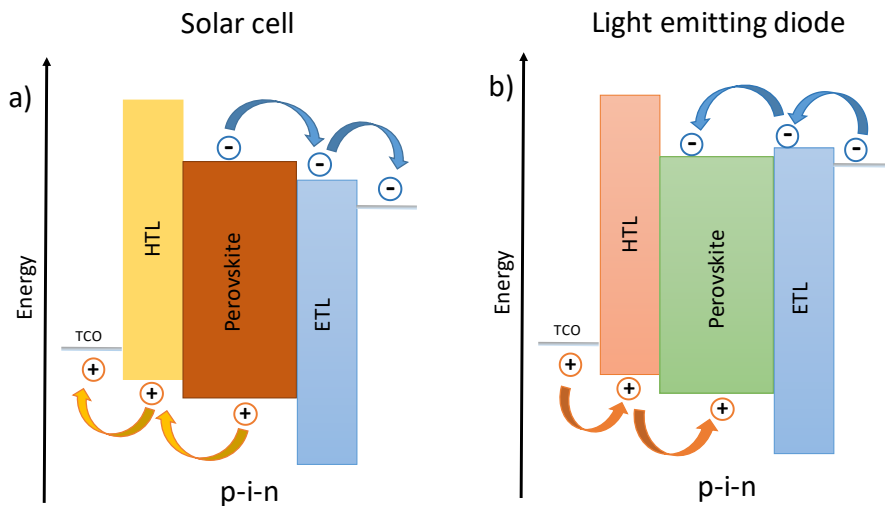


Figure 1.25. Energy band diagram of a typical multi-layered p-i-n a) solar cell with schematic electron and hole extraction b) LED with schematic electron and hole injection and blocking layers.

Generally, the transport layers are organic semiconductors or metal oxides chosen so that their energy levels (HOMO and LUMO) align with the valence and conduction band of the perovskite layer, to minimize energy losses during charge transfer. Moreover, both transport layers are also wide bandgap semiconductors, so that they transport only one type of carrier to the respectively electrode, blocking the other type of carrier. The transport material employed in perovskite LEDs are slightly different from those used in a solar cell. In a solar cell the photo-generated carriers have to be extracted from the perovskite to the electrodes while in a LED, electrons and holes have to be injected and confined in the perovskite layer where they recombine and emit light. For this reason it is crucial to judiciously select the corresponding electron-and hole-transporting interfaces with favorable energy level alignment to the CBM and VBM, respectively, avoiding losses in term of charge extraction and recombination.

Additionally, in order to remove energy barriers and promote ohmic contacts at the electrodes, additional (doped) extraction or injection layers are used (**Figure 1.26**).

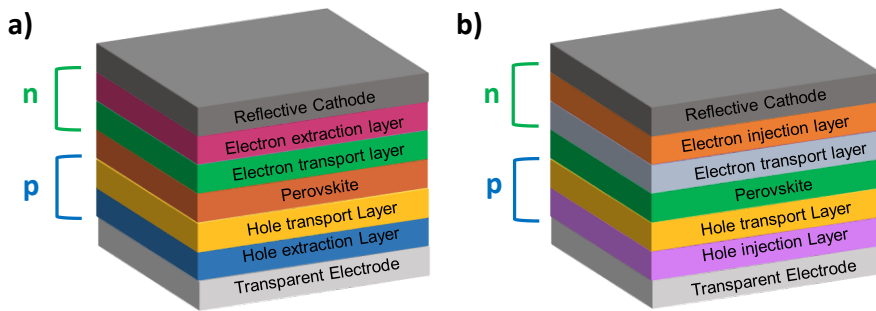


Figure 1.26. Schematic multi-layered planar a) p-i-n solar cell b) p-i-n LED

1.8 Perovskite thin film deposition techniques

The chemical nature of perovskites enables the fabrications of high quality (both optically and electronically) semiconducting thin-films by several deposition methods. Requirements for perovskite films to be applied in optoelectronics are phase purity, dense morphology consisting of close-packed grains free of voids and pinholes. These features are beneficial to maximize the devices performance, for instance by suppressing shunt paths otherwise leading to current leakage, or by reducing grain boundaries that can facilitate the ingress of atmospheric agents (oxygen, moisture) and degrade the perovskite. The deposition methods can be either based on solution or on vacuum techniques and, in general, they can consist in a one-step (the precursors are deposited simultaneously onto the substrate) or two-steps depositions (the precursors are deposited sequentially and the second step consists in the conversion of the inorganic precursors to the perovskite).

1.8.1 Solution-processing deposition

In the most widely adopted *one-step spin-coating process*, a solution of the precursors (organic ammonium halide and inorganic metal halide salts) in an organic polar solvent such as N,N-dimethylformamide (DMF), dimethyl sulfoxide (DMSO), γ -butyrolactone or mixture of them, is dropped onto a substrate, which is then rotated on its axis at high speed (typically at hundreds to thousands revolutions per minute). During rotation, the solution is homogeneously spread onto the substrate, the solvent evaporates and the concentration of the perovskite precursors increases until the solubility limit (**Figure 1.27**). Once the precursors concentration reaches supersaturation, the perovskite starts to crystallize. Quantitative crystallization and removal of residual solvent is ensured by a subsequent low-temperature annealing, typically at 90-150 °C for a duration ranging from few minutes to few hours. The quality of the layer is also dependent on the substrate and in particular on the polarity of its surface, which can be modified by pre-coating with a surface tension modifier or by plasma or UV-O₃ pre-treatments of the substrate. Depending on the precursor solution and on the substrate, this method might lead to rough and not homogenous films, with poor coverage of the substrate surface.⁵⁵ This is probably a consequence of the slow evaporation of the solvent, which leads to uncontrollable crystallization. Indeed, many of the solvents capable of dissolving the metal halide precursor have high boiling points (e.g. DMF, DMSO). Those solvents can also form intermediate phase like MA-PbI₂-DMF, PbI₂-DMF or PbI₂-nDMSO complex which can further slow down the evaporation.⁵⁶ This behaviour yields to inhomogeneous nucleation that limits the control over the film formation needed to entirely cover the substrate.

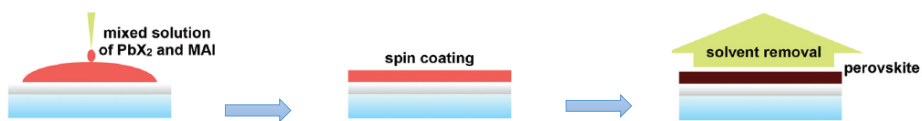


Figure 1.27. Schematic illustration of one-step solution process spin-coated deposition. Adapted from reference⁵⁷

A common strategy to control crystallization of perovskite films during spin-coating is through *antisolvent washing* procedure better known as solvent engineering (**Figure 1.28**).⁵⁸ During spin-coating, a non-polar solvent (also named antisolvent e.g., toluene, chlorobenzene, chloroform or diethylether) is dripped on top of the perovskite layer during its formation. The antisolvent, which should not dissolve the perovskite precursor but be miscible with the polar solvent used for the perovskite coating, accelerates the supersaturation of the precursor solution by fast removal of the polar solvent. In this way the crystallization kinetics is altered allowing a high nucleation density, which results in compact, homogeneous and pinhole-free films. Although the solvent exchange method can lead to high quality perovskite films, it requires the control over several different processing parameters. Among them, one of the most critical is the exact time when the antisolvent is dripped onto the substrate. If the antisolvent is applied too early, the perovskite film will be damaged, presenting visible scratches and spirals.⁵⁶ On the other hand, if the antisolvent is applied too late, it will not affect the formation of the film. Furthermore, the perovskite film can be mechanically damaged by the antisolvent due to the high-speed rotation of the substrate. Due to difficulties in controlling this type of process, the research community experiences a considerable deal of irreproducibility between different laboratories, which limits the benefits of this method.

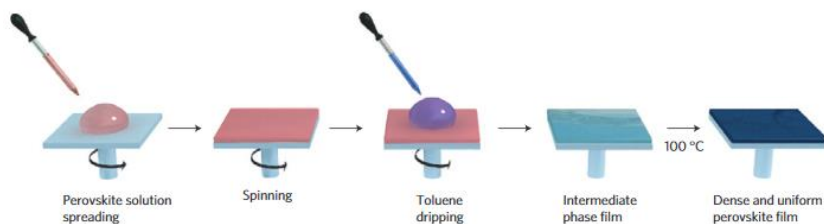


Figure 1.28. Scheme of antisolvent washing procedure. Adapted from reference.⁵⁸

The *gas-quenching* represented another technique to obtain a uniform perovskite thin film with densely packed grains. The inert gas such as Ar or N₂ play the same role of the antisolvent, promoting a rapid supersaturation of the perovskite components in the wet film during the spin-coating, leading to a large number of nuclei and a full substrate coverage, see **Figure 1.29**.^{59,60} Moreover this deposition method offers a valid alternative to the antisolvent washing procedure, reducing material costs and safety concerns due to the dependence on toxic or hazardous solvents.

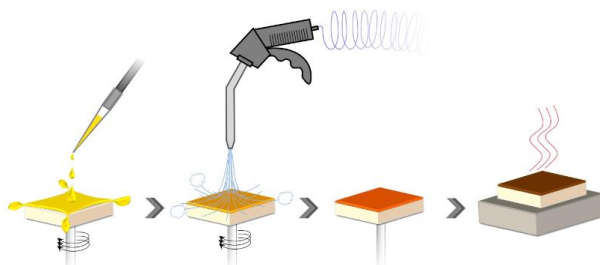


Figure 1.29. Scheme of the gas-quenching procedure. Adapted from reference⁵⁹

In *two-step deposition* methods, the formation of the perovskite layer is based on the intercalation of the organic moieties into a pre-deposited inorganic film. The

inorganic precursor is (spin)-coated on the substrate and the organic cation is subsequently introduced either by spin- or dip-coating⁶¹ (**Figure 1.30**). After deposition the layer is usually annealed in order to promote the interdiffusion of the precursors and crystallization of the perovskite.

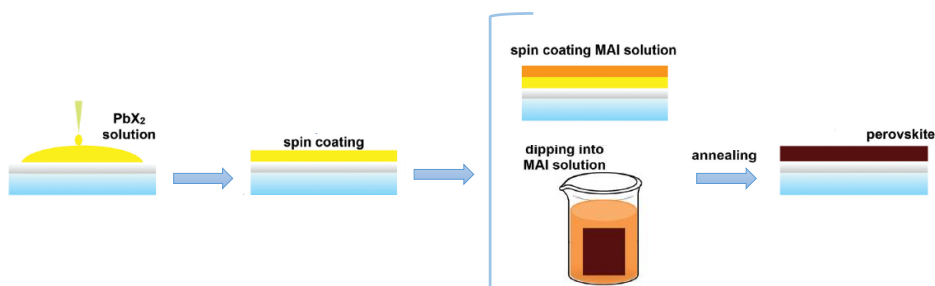


Figure 1.30. Schematic illustration of two-step solution process deposition by either spin- or dip-coating. Adapted from reference⁵⁷

The A-site cations can be introduced also by vapor-based methods in a sequential processing, in which a lead halide film is exposed to vapors of the complementary precursors and hence converted to a perovskite.⁶²

1.8.2 Vacuum-processing deposition

Vacuum-processing methods are widely adopted in the semiconductor industry with a large amount of fabrication approaches. Those offer versatility in the deposition of different perovskite thin-films and in the preparation of optoelectronic devices.^{63,64} Vacuum deposition presents many advantages compared to solution processing techniques, such as fabrication of high purity films, fine control over the film thickness and stoichiometry, typically leading to a flat and homogeneous surface. In general, vacuum deposited perovskites present a well-packed morphology with smaller grain compared to solution

process perovskites. This peculiar characteristic is correlated with the fact that the nucleation proceeds faster than the growth of the grains due to a favorable reaction of the sublimed precursors.⁶⁵ Vacuum based coating techniques eliminate also the issues associated with the use of solvents, such as toxicity, solubility limitation of precursors, formation of intermediate compounds and the need of orthogonal solvents in order to process multilayer devices. In general, no annealing is needed after the vacuum-deposition of the perovskite film because it is already well crystallized at room temperature. This low temperature fabrication makes this method compatible with a wide range of substrates, including textiles or flexible substrate such as plastic foils. Other advantages of vacuum-deposition are: i) the possibility of up-scaling the process ii) to coat uneven surfaces such as textured silicon, in order to fabricate tandem solar cells, and ii) its flexibility in terms of materials, which allows to deposit 3D, 2D, multication and mixed halide perovskites.^{66,67} As for solution-based deposition methods, vacuum techniques can be classified into one and two-step processes.

Dual-source and multiple-source vacuum deposition are among the more widely applied one-step processes to optoelectronic applications. In those vapor-base techniques, the organic cation and the metal halide, placed in thermally controlled ceramic crucibles, are simultaneously evaporated at their corresponding sublimation temperatures in a high vacuum chamber, where they condense and react on a substrate placed above the sources (**Figure 1.31a**). The material stoichiometry can be finely adjusted by control of the evaporation rates of the single components (previously calibrated).⁶⁸

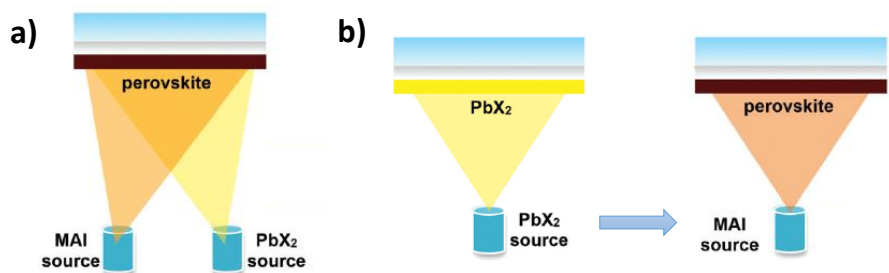


Figure 1.31. Schematic illustration of a) one-step multiple source vacuum-deposition and b) two-step single source vacuum-deposition. Adapted from reference⁵⁷

Single-source deposition is a simplified variant of co-evaporation, where a pre-formed perovskite is directly sublimed from a single thermal source or a metal foil in a high vacuum chamber, see **Figure 1.32**. The perovskite is rapidly vaporized by a fast increase of the source temperature, and for this reason the technique is also known as flash evaporation. The high speed of the process allows the perovskite to vaporize and reassemble on a substrate maintaining its initial stoichiometry.^{68–71}

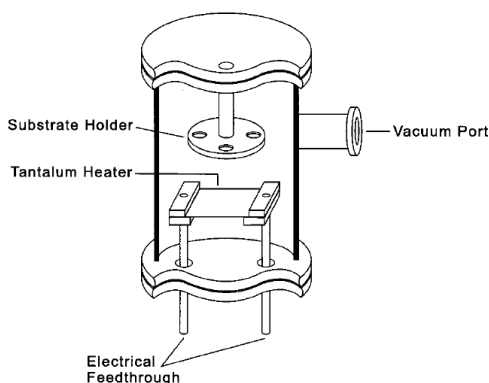


Figure 1.32. Example of a single source thermal deposition chamber

The *sequential vacuum-deposition* attempts to overcome the difficulties of controlling the evaporation of organic ammonium halides. The organic salts generally do not evaporate as a molecular beam, but rather dissociate into fragments forming a cloud, making the co-evaporation complicated to control. With sequential deposition the perovskite film is deposited layer-by-layer, one precursor after the other, followed by a low temperature annealing ⁷² (**Figure 1.31b**)

In this thesis the antisolvent washing (Chapter 2) and dual-source evaporation (Chapter 3 and 4) will be employed, and the details of each process will be further discussed in the corresponding Chapters.

1.9 Aim of the thesis

Through the end of contribute to the next generation of photovoltaics and light emitting devices the preparation of no-expensive and high quality materials with high PLQY and reduced non-radiative recombination is crucial. For such a reason the thesis is focus on the develop of high optoelectronic potential hybrid perovskite material and on their processing methods. In the different Chapters, various low dimensional perovskite synthetic approaches and their application are investigated.

In the Chapter 2, a low dimension quasi-2D perovskite with a remarkable PLQY was prepared thanks to interplay of different fabrication approaches such us altered stoichiometry, solution engineered deposition and the use of electron donor passivating agent.

In the Chapter 3, quasi-2D and pure 2D perovskite were fabricated by vacuum-deposition method in order to overcame the limitation of the solution process approach. High crystallinity, homogenous, compact films were prepared. However, different challenges were face up during the deposition process.

In the Chapter 4, the 2D perovskites fabricated by dual-source vacuum deposition in the Chapter 3 were apply to study the effect and the advantages of a wide bandgap 2D perovskite material on the reduction of non-radiative recombination of a polycrystalline 3D perovskite in a heterostructure system.



Chapter 2

Enhance the photoluminescence quantum yield of the perovskite film

2.1 Introduction

Radiative recombination of charge carriers is a critical process that must be maximized in order to reach the best performance in optoelectronic devices and in particular in light-emitting diodes. Efficient electroluminescence requires charge balance in the semiconductor so that the ratio of electrons and holes is as close as possible to one. Moreover, the leakage current (**Figure 1.24a**, Chapter 1) has to be minimized in order to reduce the probability that the carriers cross the diode without recombining, and the non-radiative loss mechanisms should be reduced in favour of radiative recombination. The outcoupling of the generated photons from the device is also very important, and can be altered with

the choice of appropriate materials and geometry. As detailed in Chapter 1, the external quantum efficiency of electroluminescence (EQE_{EL}) is proportional to the semiconductor photoluminescence quantum yield (PLQY), and hence increasing the semiconductor PLQY is key to fabricate efficient electroluminescence devices. The earliest works on perovskite LEDs employed polycrystalline methylammonium lead halides as the emitting layer, reached EQE_{LE} in the order of 1%²¹, a consequence of the low PLQY at low excitation fluence ($< 25 \text{ mW/cm}^2$).⁷³ At low excitation intensity (low charge carrier concentration) most of the charges recombine non-radiatively due to a high defect density. However, the PLQY rises at higher excitation densities after the defects are filled and radiative recombination becomes dominant. Materials for efficient LEDs should have a high PLQY at low carrier concentration, to minimize the device power consumption. One of the strategies to increase the PLQY at low fluence is the spatial confinement of charge carriers, which can be obtained by decreasing the perovskite grain size. Nanostructured perovskites such as nanoparticles (NPs) and quantum dots (QDs) have a larger exciton binding energy and lower charge diffusion length compared to bulk perovskites, which increases the excitonic and bimolecular recombination.^{74,75} Perovskites with reduced dimensionality can be prepared via several methods, either using templates or by direct synthesis of perovskite NPs. The use of templates, such as organic molecules,⁷⁶ polymers⁷⁷ or wide band gap metal oxides like Al_2O_3 ,^{78,79} results in enhanced PLQY thanks to the crystal growth confinement. Unfortunately, at the same time, the scaffold inhibits the connectivity needed for efficient charge transport through the perovskite layer, limiting the device performance. Perovskite nanoparticles prepared by colloidal chemistry can show PLQY close to unity in solution.⁸⁰⁻⁸² However, a substantial reduction of the PLQY is commonly observed when NPs suspensions are processed into thin-films, likely due to aggregation of the NPs.

Another approach to increase the exciton binding energy and limit the diffusion length in perovskites is the use of 2D crystal structures, as described in Chapter 1. However, intense luminescence has so far only been observed from 2D perovskites at liquid nitrogen temperatures. The lack of efficient luminescence at room temperature is still not well understood, but it is likely related to the thermal quenching of excitons.⁸³ Low dimensional Ruddlesden-Popper (quasi-2D) perovskites offer a means to enhance the PLQY, compared to pure 3D and 2D materials. In this Chapter, a quasi-2D lead bromide perovskite is studied, employing methylammonium (MA) and butylammonium (BA) as the small and large cations, respectively, with the aim of increasing the PLQY. The $(\text{BA})_2(\text{MA})_{n-1}\text{Pb}_n\text{X}_{3n+1}$ perovskite with $n = 5$ was used as a starting compound, since a similar stoichiometry but with phenethylammonium as the large organic cation has been successfully applied in efficient LEDs.^{84,85} The ratio between BA and MA was varied while the concentration of PbBr_2 was maintained constant. In the quasi-2D perovskite with $n = 5$, $(\text{BA})_2(\text{MA})_4\text{Pb}_5\text{X}_{16}$ the BA:MA molar ratio is 2:4. In order to study the influence of the concentration of the long chain cations on the material growth and properties, higher organic cations ratios were also investigated (BA:MA = 3:3 and 4:2). It is important to underline that for higher BA:MA ratios the stoichiometry deviates from a Ruddlesden–Popper phase, however, for simplicity in this Chapter they will be referred to as quasi-2D perovskites.

2.2 Material preparation

The perovskite precursor solution was prepared by dissolving BABr (Dyesol), MABr (Dyesol) and PbBr_2 (Sigma Aldrich, 99.999% trace metals basis) in dimethyl sulfoxide (DMSO) solution with a concentration of 200 mg/mL. The solution was stirred at 60 °C overnight and was filtered using a

PTFE syringe filter (0.22 μm) before deposition. The different quasi-2D stoichiometries were prepared by dissolving BABr, MABr and PbBr₂ in dimethyl sulfoxide (DMSO) solutions, maintaining the overall concentration at 200 mg/mL. The exact precursors composition for each BA:MA ratio is reported in **Table 2.1**.

BABr:MABr:PbBr ₂ molar ratio	In 1 mL	BABr	MABr	PbBr ₂
2:4:5	mass (mg)	23.8	34.6	141.6
	mole (mol)	0.154	0.309	0.386
3:3:5	mass (mg)	35.1	25.5	139.4
	mole (mol)	0.228	0.228	0.380
4:2:5	mass (mg)	46.1	16.7	137.2
	mole (mol)	0.299	0.150	0.374

Table 2.1. Perovskite precursors composition for different BA:MA ratio.

The deposition was initially performed by single step spin-coating on glass substrates in a nitrogen filled glovebox.

2.3 Discussion

The absorption spectra of the quasi-2D perovskite film series processed by single step spin-coating are reported in **Figure 2.1**. In the optical absorption spectra of all compounds, several different absorption peaks can be identified, as expected for low dimensional perovskites. Ruddlesden–Popper perovskites, in this case, present a distribution of n , i.e. a distribution of phases with different thickness of the inorganic slabs. The quasi-2D perovskite with BA:MA = 2:4

shows the typical band-to-band absorption of 3D MAPbBr₃ (**Figure 2.1a**) at about 528 nm, with additional excitonic features at 454 nm and 435 nm.

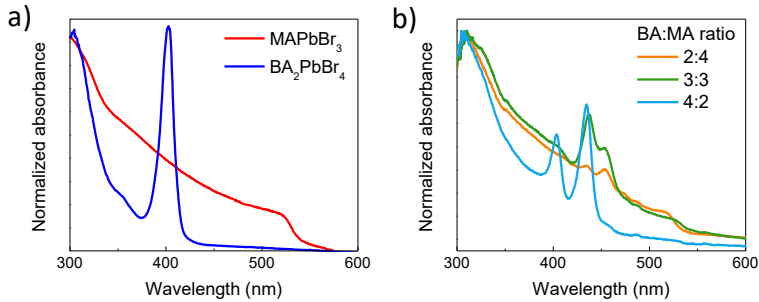


Figure 2.1. Thin-films absorption spectra of a) the archetype 3D MAPbBr₃ and 2D BA₂PbBr₄ perovskites and b) quasi-2D perovskites with different BA:MA ratios.

With increasing BA:MA ratio (3:3 and 4:2, **Figure 2.1b**), the excitonic character of these transitions increases as a consequence of the exciton confinement in the inorganic sheets, which are separated by the organic cations. At the same time, the absorption onset at 528 nm slowly disappears, implying that the formation of 2D-type layered perovskites is favored. In fact, the perovskite with the BA:MA ratio of 4:2 shows an additional absorption peak at about 400 nm, which is similar to that of the pure BA₂PbBr₄ 2D phase (**Figure 2.1a**). Unfortunately, this thin-film series exhibited negligible photoluminescence at the low excitation intensity used in our measurements, i.e. a monochromatic light at a wavelength of 330 nm obtained from a Xenon lamp coupled to a monochromator (irradiance $\sim 0.1 \text{ mW cm}^{-2}$). The PLQY, the perovskite morphology and the crystallinity can be improved by using an antisolvent washing procedure during the spin-coating deposition, as described in the Chapter 1. This method is expected to reduce the trap density.

2.4 Engineered perovskite films

Chloroform (CHCl_3) was used as “antisolvent” due to its low polarity with respect to the perovskite precursor solvent, DMSO. Several parameters have been adjusted and studied in order to modify the film morphology, in particular the spinning speed, the volume of antisolvent and the dripping time. Upon optimization of these parameters (based on optical and morphological quality of the films), the deposition was performed via consecutive spin-coating at 1000 and 3000 rpm for 5 and 60 seconds, respectively. After 35 seconds during the second spin-coating step, 300 μL of CHCl_3 were dripped onto the spinning substrate and the resulting films were annealed at 90 $^\circ\text{C}$ for 5 minutes. As a consequence of the solvent engineering (SE) method, the optical absorption profiles of the perovskite film with the same compositions described before (simple spin-coating deposition) was found to be substantially altered.

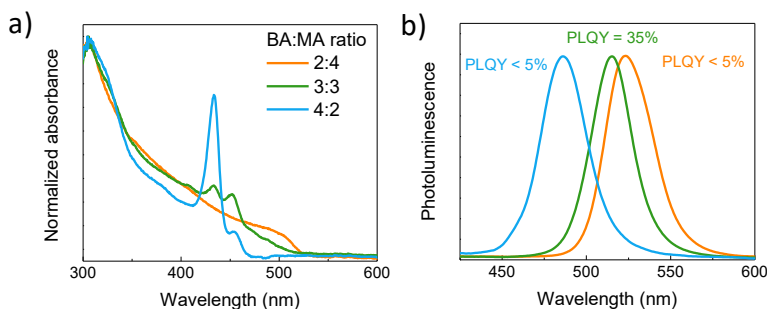


Figure 2.2. a) thin-films absorption spectra of quasi-2D perovskite with different BA:MA ratio deposited with solvent engineering (SE) method and b) normalized photoluminescence spectra of the quasi-2D perovskite series under irradiation at 330 nm.

As clearly visible from the absorption spectra reported in **Figure 2.2a**, the absorption onset at about 528 nm is shifted at higher energy, compared to the analogous films prepared without solvent engineering (**Figure 2.1b**), most likely

due to grain size reduction and morphology modification.⁸⁶ Moreover, the intensity of the excitonic absorption in pure 2D and quasi-2D perovskites (2:4 and 3:3) is reduced, while the absorption spectrum for the 4:2 compound show a more intense excitonic absorption centered at 430 nm. What is more interesting is that these low dimensional perovskite films exhibited bright photoluminescence under low fluence excitation at 330 nm (**Figure 2.2b**). This is a consequence of the solvent engineering process, which rapidly removes the excess DMSO reducing the precursors solubility and hence modifying the crystallization kinetics. The induced fast crystallization may limits the grain growth of the perovskite during the deposition and enhancing the photoluminescence due to charge confinement. The PL spectra shift follow the trend observed in the optical absorption, blue-shifting from 523 nm to 515 nm and 486 nm when increasing the BA content with BA:MA ratios of 2:4, 3:3 and 4:2, respectively. The corresponding PLQY is below 5% for the 2:4 and 4:2 materials, while the equimolar 3:3 perovskite exhibits a PLQY of 35%. While remarkable, this value is still low, indicating that trap states are present and act as non-radiative recombination centres. A way to further enhance the PLQY is through passivation of these trap states, which can be performed, for example, by dissolving an electron donor in the solvent used for the washing and/or by post-deposition treatments with a variety of Lewis bases.^{74,87-90} The additive can bind to the under-coordinated Pb ions and compensate the halide vacancies, which are the most commonly reported surface traps. Here we choose a n-type molecular semiconductor, 9,9-spirobifluoren-2-yl-diphenylphosphine oxide (SPPO1), that act also as a Lewis base due to the phosphine oxide group, (**Figure 2.3**) and studied its effect on the morphology and optical properties of the perovskite films.

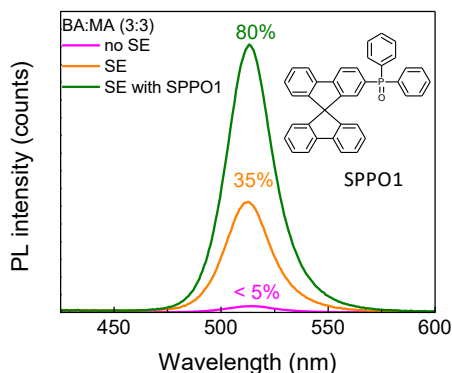


Figure 2.3. Photoluminescence spectra and corresponding PLQY of the quasi-2D perovskite with equimolar BA:MA ratio, without and with SE and with SE in the presence of SPPO1 under excitation at 330 nm. The SPPO1 chemical structure is also reported.

SPPO1 was added to the chloroform used for the antisolvent treatment during the deposition of the 3:3 quasi-2D perovskite, which was selected in view of its already high PLQY. The deposition process with the SPPO1 additive has a strong effect on the photoluminescence properties of the perovskite film, resulting in a very high PLQY of 80% (**Figure 2.3**). Besides being obtained in 2016, this value is still among the higher reported PLQY values for perovskite thin-films.^{88,91} The absorption spectra of the quasi-2D perovskite with BA:MA 3:3 ratio deposited by simple spin-coating, with solvent engineering and with solvent engineering in the presence of SPPO1 have rather similar profiles (**Figure 2.4a**). For this reason, the different PLQY is likely related to a diminished grain size, as supported by the XRD measurements. The broadening of the diffraction peaks observed for the perovskites prepared with solvent engineering and SPPO1 (**Figure 2.4b**) is consistent with the presence of smaller crystalline domains.

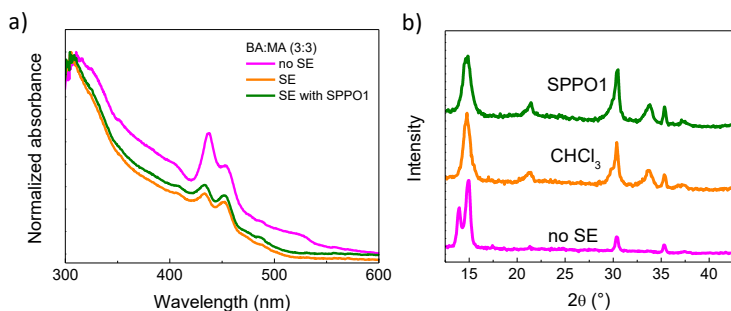


Figure 2.4. a) Absorption spectra of the quasi-2D perovskite thin-films with BA:MA 3:3 ratio without, with SE and with SE in the presence of SPPO1. b) Grazing incidence X-ray diffraction patterns of the same samples.

In order to investigate the relationship between morphology and PLQY, the perovskite films were analyzed by atomic force microscopy (AFM). **Figure 2.5** shows the AFM topographies with the corresponding profiles for the 3:3 quasi-2D perovskite films, prepared without solvent engineering, with solvent engineering and in the presence of SPPO1. Clearly, the simple one-step spin-coating does not yield a homogeneous perovskite film (**Figure 2.5a**), leading to a rough surface with a significant height variations through the sample. This is likely due to the slow evaporation of the DMSO which leads to inhomogeneous nucleation and consequently to uncontrolled crystallization during the film formation. On the other hand, the chloroform dripping drastically reduces the surface roughness, leading to a more flat and homogeneous sample, consequence of a limited grain growth in favor of a high nucleation density (**Figure 2.5b**). In the presence of SPPO1 (**Figure 2.5c**), the average grain size appears to be further reduced, as well as the overall homogeneity of the sample surface. The peak to peak roughness R_{PTP} diminishes from 105 nm for the samples without SE treatment to 80 nm and 70 nm for the quasi-2D perovskite films obtained after SE with CHCl_3 and SE with CHCl_3 and SPPO1, respectively.

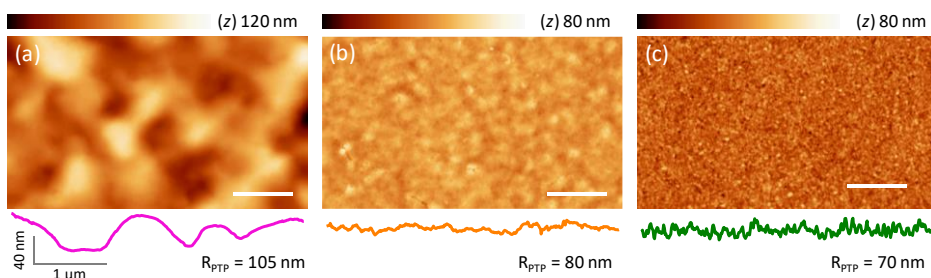


Figure 2.5. AFM topographies of the quasi-2D perovskite films with equimolar BA:MA 3:3 ratio a) without SE, b) with SE and c) with SE in the presence of SPPO1. The corresponding surface profile is shown at the bottom of each picture.

In order to shed light on the role of SPPO1 during solvent engineering, we performed time-resolved PL (TRPL) measurements in the nanosecond time scale on thin films with and without SPPO1. In contrast to previous reports for perovskite films upon passivation,⁸⁹ we observed that the PL lifetime is essentially unchanged (**Figure 2.6**). This observation can be explained by considering that non-radiative recombination is faster than the TRPL excitation pulse, hence the PL decay reflects similar radiative recombination kinetics for the two samples.

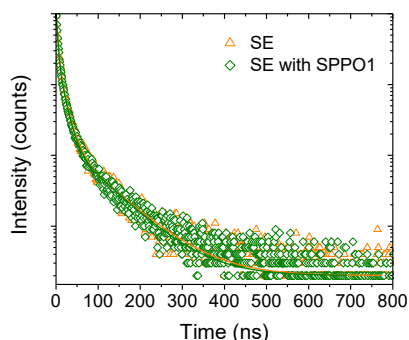


Figure 2.6. Time-resolved PL measurement taken at the peak emission wavelength of the thin-film quasi-2D BA:MA 3:3 ratio with a LED wavelength of 340 nm.

In summary, the remarkable PLQY observed is the result of a synergistic effect of (i) the choice of a suitable BA:MA ratio, (ii) the use of solvent engineering and (iii) the introduction of an electron-donating molecule such as SPPO1, which leads to grain size reduction and passivation of trap states.

Another interesting characteristic of these films is their ambient stability. Surprisingly, passivated quasi-2D films stored in ambient condition (in the presence of oxygen and moisture) exhibited a PLQY as high as 43 % even 3 years after preparation. The photoluminescence homogeneity of a film stored in air for 3 years was investigated with a hyperspectral imager microscope coupled with a continuous wave laser exciting at 405 nm an area of $330 \times 330 \mu\text{m}^2$. The PL image (**Figure 2.7**) shows the high homogeneity of the film despite the long exposure to air. Also, the average PL spectrum over the whole field of view is consistent with that of the as-prepared films shown previously (**Figure 2.3**).

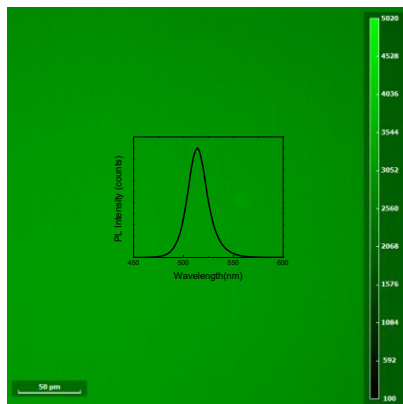


Figure 2.7. Hyperspectral image of the BA:MA 3:3 perovskite film stored in air for three years. The average PL spectrum is also reported.

2.5 Light Emitting Diode application

The high PLQY together with the morphological quality of the BA:MA 3:3 quasi-2D films is suited for LEDs applications. Hence, they were integrated into multilayer devices with a p-i-n configuration. The transparent anode consists of a glass substrate with an indium tin oxide (ITO) coating, which was cleaned with a detergent solution, Millipore water, isopropyl alcohol, and then treated in a UV-ozone chamber for 20 minutes to activate the surface. The p-i-n device structure includes a 70 nm thick hole injection layer, poly(3,4-ethylenedioxythiophene) doped with poly(styrenesulfonate) (PEDOT:PSS), spin-coated in air and annealed at 150 °C for 15 minutes. Subsequently the perovskite layer was deposited in a nitrogen filled glovebox with the process described above. The electron transport layer 1,3-bis[3,5-di(pyridin-3-yl)phenyl]benzene (BmPyPhB, 40 nm) and a metal cathode (Ba 10 nm, Ag 100 nm) were instead thermally evaporated in a high vacuum chamber. The flat band energy diagram for this architecture device is depicted in **Figure 2.8**.

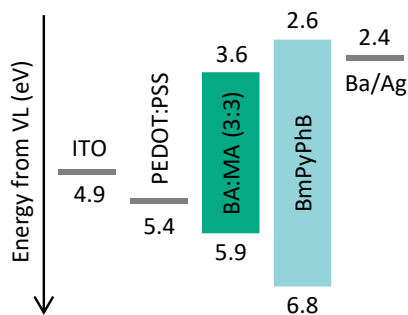


Figure 2.8. Schematic flat energy diagram for the set of materials used, referred to the vacuum level (VL) (values from references ^{92,93})

The LEDs electroluminescence was observed at low applied bias (3.5 V) and it increase rapidly until it reaches about 1000 cd m^{-2} at 8V, as depicted in **Figure 2.9a**. Despite the high luminance, these devices showed a rather high current density, which limits the overall current efficiency to 1.3 cd A^{-1} (**Figure 2.9b**).

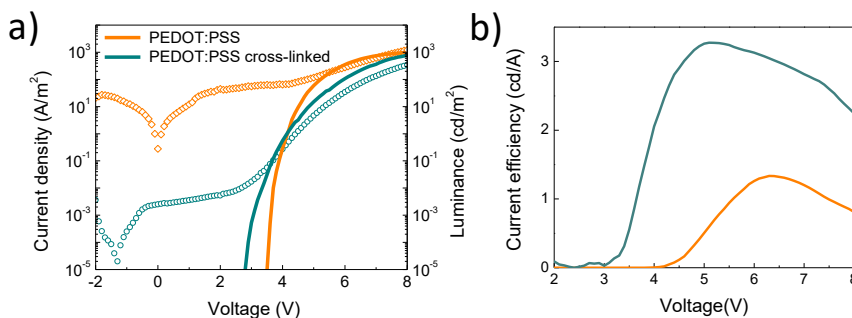


Figure 2.9. a) Current density and luminance and b) current efficiency versus applied bias for the LEDs prepared with and without cross-linked PEDOT:PSS.

This phenomenon might arise from the partial solubility of PEDOT:PSS in the DMSO solvent used for the perovskite processing, hindering the formation of a well-defined interface between the hole injection and the emissive layers. In order to improve the PEDOT:PSS stability and its adhesion to the metal oxide substrate, we added to its suspensions a small amounts (1 v/v%) of 3-glycidoxypropyltrimethoxysilane (GOPS) as a cross-linking agent.⁹⁴ The cross-linking of PEDOT:PSS with GOPS takes place at the same temperature we used for the annealing of PEDOT:PSS neat films (150 °C). As a result of the incorporation of the modified, cross-linked hole injection PEDOT:PSS layer, the LEDs leakage current is substantially reduced, leading to the expected J–V curve for a high quality diode and at the same time, a reduced turn-on voltage for electroluminescence (2.8 V), indication of a better charge injection into the perovskite emitter (**Figure 2.9a**). The luminance rapidly increases reaching a brightness of about 1000 cd m^{-2} at 8 V, with green electroluminescence

analogous to the photoluminescence spectrum observed above (**Figure 2.10**). Moreover, the maximum current efficiency reaches 3.3 cd A^{-1} at 5 V (**Figure 2.9b**).

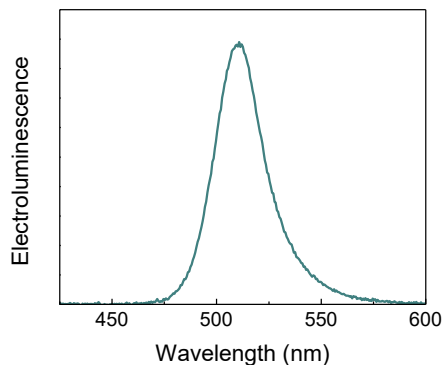


Figure 2.10. Electroluminescence spectrum of the LED using quasi-2D BA:MA 3:3 perovskite as the emissive layer.

Despite the promising performance of the LEDs, if one considers the high PLQY (80%) of the perovskite emitter, it is obvious that other loss mechanisms are hindering efficient electroluminescence. Possible further improvements can be obtained with the use of selective hole-transport materials on top of PEDOT:PSS, or by modifying the PEDOT:PSS surface work function. Poly-TPD [Poly(N,N0-bis(4-butylphenyl)-N,N0-bis(phenyl)-benzidine), VB-FNPD [9,9-bis[4-(4-ethenylphenyl)methoxy]-phenyl]-N2,N7-di-1-naphthalenyl-N2,N7-diphenyl-9H-fluorene-2,7 diamine] and a modified PEDOT:PSS with NAFION (sulfonated tetrafluoroethylene copolymer) were hence tested in the perovskite LEDs. Unfortunately, the best performance remained that obtained with the cross-linked PEDOT:PSS with GOPS. Additional progress might be achieved with transport materials that promote charge balance assisting the electrons or holes injection while confining the opposite charges into the perovskite film.

2.6 Conclusion

In this Chapter the preparation of high photoluminescence quantum yield in low dimensional perovskites has been reported. The development of a material engineering protocol including the modification of the perovskite solution deposition with antisolvent washing and variation of the ratio between the large (BA) and small (MA) organic cations. A remarkable PLQY of 35% was obtained for quasi-2D perovskite films with a BA:MA 3:3 ratio. A further enhancement of the PLQY up to 80% was obtained with the addition in the antisolvent of an organic semiconductor with electro donating properties, likely reducing non-radiative recombination channels. Thin-films of these materials have been integrated in multilayer LEDs which showed a low current leakage and a low turn-on voltage for electroluminescence, a high brightness of about 1000 cd m⁻² and a maximum current efficiency of 3.3 cd A⁻¹.

Author contribution

Complete Journal article is added to Appendix 1

La-Placa, M. G.; Longo, G.; Babaei, A.; Martínez-Sarti, L.; Sessolo, M.; Bolink, H. J. Photoluminescence Quantum Yield Exceeding 80% in Low Dimensional Perovskite Thin-Films: Via Passivation Control. *Chem. Commun.* **2017**, 53 (62), 8707–8710. <https://doi.org/10.1039/c7cc04149g>

Chapter 3

Vacuum-deposition of low dimensional perovskites

3.1 Introduction

In Chapter 2, a reliable method to prepare high quality quasi-2D perovskite thin-films, was described. However, the antisolvent washing method requires the control over several different processing parameters, compromising the reproducibility of the perovskite film growth. To overcome this limitation, the vacuum-deposition of quasi-2D and pure 2D perovskites has been investigated. While the solution processing and single crystal fabrication of 2D hybrid perovskites have been widely reported, vacuum processing of these materials remains rather unexplored. Only few reports have described the sequential vacuum-deposition⁹⁵ and single-step thermal ablation^{70,96} of low-dimensional perovskite films. The sequential deposition of the precursors needs, however, a post deposition annealing to ensure the formation of the perovskite

structure. In the flash evaporation, the deposited film might contain different phases, due to the different sublimation temperatures of the organic and inorganic components. These techniques are simpler variants of the vacuum co-deposition method which is discussed in this Chapter. The multiple-source vacuum deposition of hybrid perovskite is often more challenging compared to the other vacuum methods because of the distinctly different physical and chemical properties of the organic and inorganic components, and for other reasons that will be discussed in the following. Nevertheless, the co-deposition presents several advantages over solution processing, as highlighted in Chapter 1. Only one report exists on fully co-evaporated 2D perovskites, and it dates back to 1997.⁹⁷ In this report, however, the lack of higher order peaks in the X-ray diffraction profile suggests that the vacuum-deposited film were defective and disordered. In this Chapter, the multiple-source vacuum co-deposition of different quasi-2D as well as pure and mixed halides 2D perovskite films is presented. Their structural, optical and charge transport properties are also investigated.

3.2 Vacuum- deposited thin-film preparation

Bare and ITO-coated glass substrates were subsequently cleaned with soap, water and isopropanol in an ultrasonic bath, followed by UV-ozone treatment. They were then transferred to a vacuum chamber integrated into a nitrogen-filled glovebox (H_2O and $\text{O}_2 < 0.1$ ppm) and evacuated to a pressure of 10^{-6} mbar. The vacuum chamber is equipped with four temperature-controlled evaporation sources (Creaphys) fitted with ceramic crucibles and independent temperature controllers and shutters (**Figure 3.1**). A quartz crystal microbalance (QCM) sensor was used for each evaporation source with an additional one placed close to the substrate holder to monitor the total deposition rate. The thin-

films were prepared by co-sublimation of the precursor compounds, upon calibration of the deposition rate for each material. The calibration factor was obtained by comparing the thickness of the thin film detected from the QCM sensors with that measured with a mechanical profilometer.



Figure 3.1. Picture of the evaporation chamber employed for the deposition of perovskite thin-films.

3.3 Materials

All organic ammonium salts, $C_4H_{12}IN$ (BAI), $C_4H_{12}BrN$ (BABr), $C_3H_{10}IN$ (PAI), $C_3H_{10}BrN$ (PABr), $C_8H_{12}IN$ (PEAI) and $C_8H_{12}BrN$ (PEABr), were purchased from Lumtec. PbI_2 and $PbBr_2$ were purchased from Tokyo Chemical Industry CO (TCI). All materials were used as received.

3.4 Vacuum deposition of Ruddlesden-Popper perovskites

Initially, the same material presented in the previous Chapter ($BA_2(MA)_{n-1}Pb_nBr_{3n+1}$) was chosen as the target Ruddlesden-Popper perovskite to be vacuum processed. The process involves a three-source co-deposition of

butylammonium bromide (BABr), methylammonium bromide (MABr) and lead bromide (PbBr₂). Hence we first investigated the formation of the archetypical compound MAPbBr₃ by dual-source deposition of the precursor compounds, MABr and PbBr₂. The small organic cation MABr was deposited at a rate of 1.1 Å/s and a temperature ranging from 180 to 220 °C, while the inorganic salt was sublimed at a rate of 0.4 Å/s (temperature 260- 300 °C). The optical absorption spectra of as-deposited MAPbBr₃ films (**Figure 3.2**) show the expected band-to-band absorption onset at about 530 nm (2.3 eV), in agreement with that of the same materials obtained by solution processing (**Figure 2.1**, Chapter 2). The vacuum-deposited films were transparent and uniform with a dim orange colour.

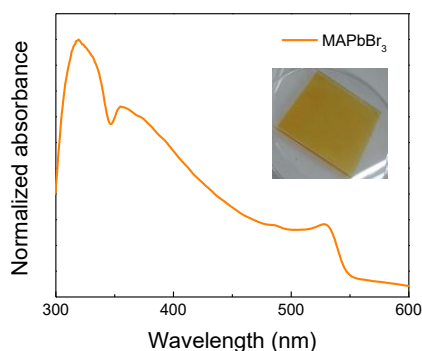


Figure 3.2. Absorption spectrum of a vacuum-deposited 3D MAPbBr₃ thin-film and photography of the same.

The X-ray diffraction of the three dimensional perovskite (**Figure 3.3a**) shows only the reflections corresponding to the MAPbBr₃ perovskite, indicating a good phase purity of the compound.⁹⁸ Moreover, the presence of intense diffraction signals indicates that the 3D perovskite is highly crystalline. The top-view scanning electron microscopy (SEM) image of the MAPbBr₃ perovskite (**Figure 3.3b**) confirms the formation of a high quality thin-film, with complete surface

coverage and with compact and uniform morphology. All grains exhibit an elongated cuboid shape with a length of approximately 100 nm.

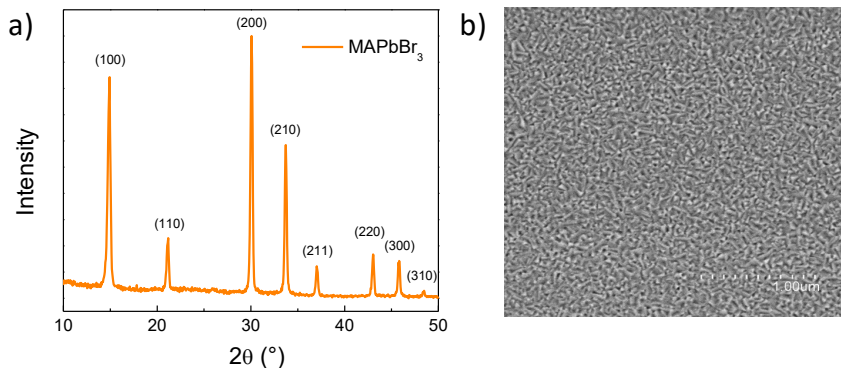


Figure 3.3. a) X-ray diffraction and b) SEM image of a vacuum-deposited MAPbBr₃ thin film. The scale bar is 1 μm.

After the development of a reliable process for the deposition of the 3D perovskite, the co-deposition was modified by adding a third source containing the large ammonium cation BABr. The BABr was found to sublime at approximately 160 °C. **Figure 3.4** reports the absorption spectra of the as-prepared material obtained with two different BABr deposition rates, 0.5 Å/s (**Figure 3.4a**) and 1 Å/s (**Figure 3.4b**). The rates were modified in order to understand the effect of different amounts of large ammonium cation on the growth of the perovskite. Similarly to the materials described in Chapter 2, the vacuum-processed perovskite films exhibit multiple absorption peaks that can be ascribed to a distribution of domains with different n values (thickness of the inorganic slabs) rather than a pure phase, as commonly reported in the literature.^{99,100}

The absorption spectrum of the compound obtained with BABr deposition rate of 0.5 Å/s (**Figure 3.4a**) shows a band-to-band absorption at about 525 nm, which represents the absorption edge of the 3D MAPbBr₃ ($n = \infty$), and two additional excitonic peaks at 447 nm and 412 nm, characteristic of small n values.

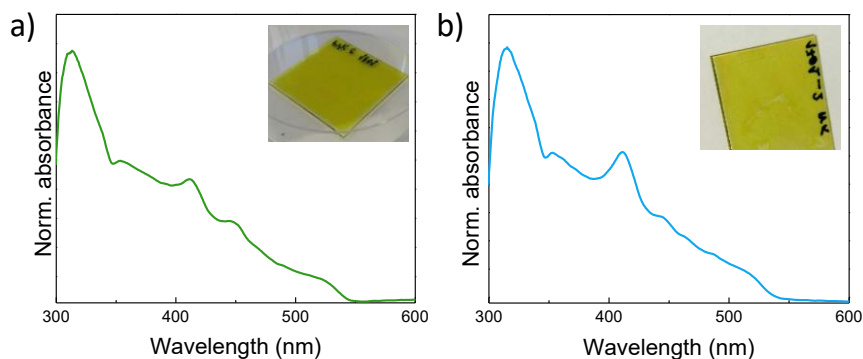


Figure 3.4. Absorption spectra of the vacuum processed Ruddlesden-Popper perovskite thin-films obtained at different BABr deposition rates, a) 0.5 Å/s and b) 1 Å/s. The images of the as-deposited films are also reported.

The spectrum collected for the compound with higher rate of BABr during the deposition (**Figure 3.4b**) shows an absorption onset at slightly higher energy (515 nm). Moreover, the intensity of the excitonic peak close to 400 nm is higher, suggesting that the stoichiometry is closer to that of the pure 2D BA₂PbBr₄ perovskite. This behavior follows the same trend observed for solution-processed Ruddlesden-Popper perovskites presented in the previous Chapter. The vacuum deposited films were transparent and uniform with a yellowish colour, as shown in **Figure 3.4**. Compared with the XRD diffraction of the 3D perovskite (**Figure 3.3**), the XRD patterns of the materials deposited in the presence of BABr with a deposition rate of 0.5 Å/s (**Figure 3.5**) reveal additional low-angle

reflections, suggesting the formation of a low dimensional perovskite compound. Unfortunately, these data also show the presence of reflections related to the MAPbBr₃ 3D phase, as indicated by the asterisks in the **Figure 3.5**, suggesting a low phase purity for this compound.

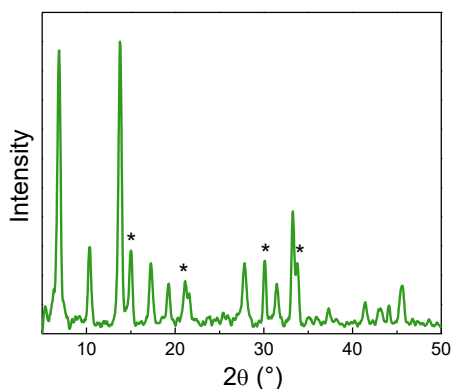


Figure 3.5. X-ray diffraction pattern of the vacuum-deposited Ruddlesen-Popper perovskite thin films. The stars indicate reflections of the 3D MAPbBr₃ perovskite.

The diffraction signals at low angles corresponds to (0k0) reflections due to the presence of low dimensional perovskite phases with a small n . Typically, the number of (0k0) peaks below $\sim 2\theta = 14^\circ$ determine the n value of the quasi-2D perovskite, and in particular the compounds with $n = 2, 3$ or 4 would show two, three or four evenly spaced reflections below 14° , respectively. The threshold at $2\theta = 14^\circ$ is due to the fact that at this angle the d-spacing matches the distance between the inorganic layers in both 2D and 3D perovskites.¹⁰¹ The XRD pattern (**Figure 3.5**) shows three equally spaced peaks below 14° , however the diffraction was recorded up to $2\theta = 5^\circ$ and hence it is not possible to determine the exact value of n . The SEM images in **Figure 3.6** show a homogeneous and compact film, composed of grains with sizes ranging from 200 to 400 nm, hence larger than the grains of the 3D MAPbBr₃ perovskite in **Figure 3.3b**.

Interestingly, increasing the BABr sublimation rate from 0.5 to 1 Å/s leads to an increase of the grain size (**Figure 3.6**).

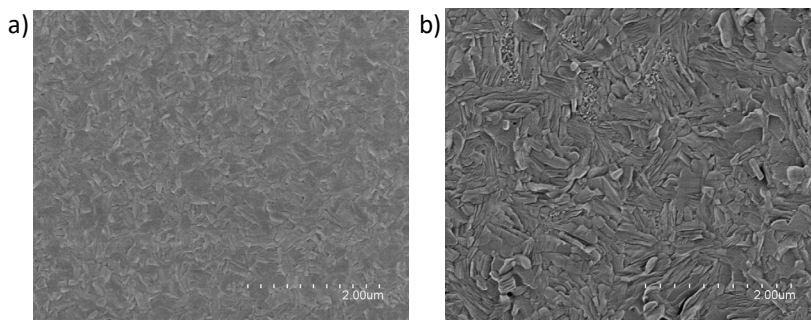


Figure 3.6. SEM images of the vacuum-deposited perovskite films with different BABr deposition rates, a) 0.5 Å/s and b) 1.0 Å/s. The scale bar is 2 μm.

Apart from the formation of films with low phase purity, the vacuum co-deposition of quasi-2D perovskites was not found to be very reproducible. During the deposition the pressure inside the chamber (usually stable at 10^{-6} mbar) increases to $>10^{-5}$ mbar, limiting the control of the evaporation process. Moreover, organic salts are often not thermally stable and not easy to sublime due to the possible dissociation in their volatile precursors.¹⁰² Due to these reasons, the deposition rates and the sensor cross-reading of the large and small organic cations were difficult to control, making the process not reliable. As low dimensional perovskites, in contrast to 3D perovskites, offers less restrictions to the size of the cations that can be accommodated between the inorganic sheets, the vacuum sublimation of other organics cations have been studied. In particular butylammonium iodide (BAI), propylammonium bromide (PABr), propylammonium iodide (PAI), phenethylammonium bromide (PEABr) and phenethylammonium iodide (PEAI) were tested. During the sublimation of most of them, an increase of the vacuum pressure was observed, accompanied by the

physical ejection of their powders from the crucibles. This behavior complicates their co-evaporation with the other organic and inorganic precursors needed for the deposition of quasi-2D perovskites. Only the sublimation of the phenethylammonium halide was found to be reasonably stable, hence PEAI and PEABr were further investigated for the vacuum processing of the simplest archetypical 2D perovskites.

3.5 Vacuum co-deposition of two-dimensional perovskite

The synthesis of different pure and mixed halide 2D perovskite, of formula $(R-NH_3)_2BX_4$, by dual source vacuum deposition was investigated together with their structural, optical and charge transport properties. Phenethylammonium lead iodide $(PEA)_2PbI_4$ and phenethylammonium lead bromide $(PEA)_2PbBr_4$ were deposited by sublimation of the corresponding organic ammonium and metal halides, phenethylammonium iodide (PEAI) and lead iodide (PbI_2) in the first case, and phenethylammonium bromide (PEABr), and lead bromide ($PbBr_2$) in the second case. All the depositions were performed in the same vacuum chamber reported in **Figure 3.1**. The organic precursors were outgassed in the high vacuum chamber prior to the deposition and were sublimed at the minimum temperature required for their evaporation. These precautions led to a stable and reproducible co-deposition of 2D perovskites. The PEAI and PEABr were sublimed around 160 °C while PbI_2 and $PbBr_2$ were sublimed at temperatures ranging from 260 to 300 °C. The mixed halide $(PEA)_2PbBr_2I_2$ perovskites films were prepared with the same procedure and are described in this Chapter as $(PEABr)_2PbI_2$, when deposited by co-sublimation of PEABr and PbI_2 , and as $(PEAI)_2PbBr_2$ in the case of PEAI and $PbBr_2$ co-evaporation. The relative deposition rate of the organic halides and lead salts was 2:1, in agreement with the compounds stoichiometry.

The structural properties of the sublimed thin films 2D perovskites were studied by X-ray diffraction. The diffractograms (**Figure 3.7**) were collected for both the as-deposited samples and for the low-temperature annealed films (5 min at 100 °C in an inert atmosphere).

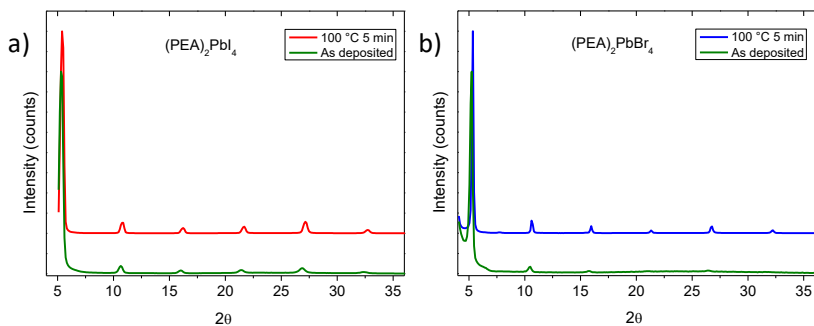


Figure 3.7. XRD patterns of vacuum deposited a) $(\text{PEA})_2\text{PbI}_4$ and b) $(\text{PEA})_2\text{PbBr}_4$ perovskite thin-film, as deposited and after annealing at 100 °C for 5 minutes.

The perovskite films show similar diffraction patterns before and after annealing, albeit more intense and sharper diffraction peaks can be observed for the annealed samples, especially for the bromide compound. This means that the crystallization of the perovskites occurs directly during the deposition process at room temperature, while crystallinity can be enhanced with a short thermal annealing a 100 °C. Therefore, we performed thermal annealing as standard process for all the pure and mixed 2D perovskite compositions. XRD analysis was carried out with Fullprof software and whole-pattern Le Bail fits (**Figure 3.8**, solid lines) were performed on the acquired diffractograms (**Figure 3.8** open circles) to refine the lattice parameters.

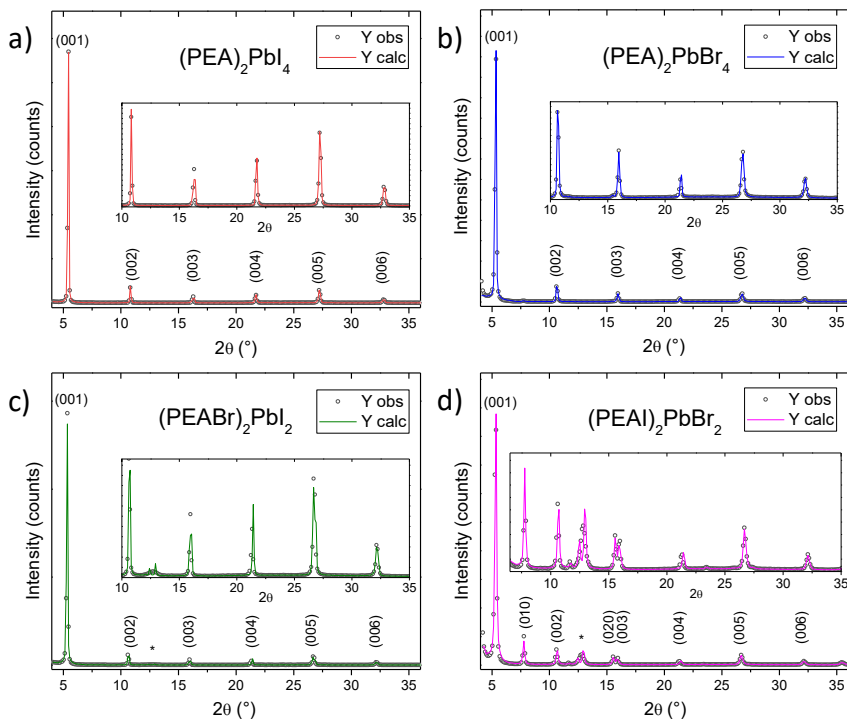


Figure 3.8. X-ray diffraction analysis of 200 nm thick, vacuum-deposited 2D perovskites films after annealing for 5 min at 100 °C. “Y obs” indicates the experimental traces while “Y calc” indicates the calculated intensities based on whole-pattern fitting (Le Bail refinement).

As can be seen from **Figure 3.8** the diffractograms can be well-fitted by considering a P -1 space group with varying lattice parameters as detailed in **Table 3.1**.

Sample	a (Å)	b (Å)	c (Å)	α (°)	β (°)	γ (°)
(PEA) ₂ PbI ₄	11.49	11.73	17.14	99.63	105.36	89.85
(PEA) ₂ PbBr ₄	11.60	11.63	17.51	99.57	105.55	89.83
(PEABr) ₂ PbI ₂	11.60	11.63	17.49	99.61	105.62	89.81
(PEAI) ₂ PbBr ₂	11.60	11.56	17.48	99.59	105.67	89.79

Table 3.1 Lattice parameters derived from Le Bail fits for different samples. Space group = P -1

Table 3.1 shows that as the halogen becomes smaller, the c-axis parameter, perpendicular to the inorganic perovskite sheets, increases from 17.14 Å for (PEA)₂PbI₄ to 17.51 Å for (PEA)₂PbBr₄. Qualitatively, this can be clearly seen by a shift of the corresponding (00l) peaks to lower angles in **Figure 3.9**.

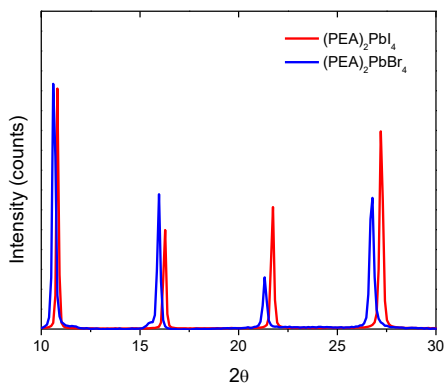


Figure 3.9. comparison of XRD patterns of a vacuum deposited PEA₂PbI₄ and PEA₂PbBr₄

This behavior, which might appear counterintuitive, has already been reported for the same and in other similar 2D perovskites, and it is attributed to a different

orientation of the phenethylammonium cations between the inorganic layers.^{103,104} When the octahedra contract (due to smaller and more electronegative halides), the aromatic substituents in the organic cations will tilt with a higher angle with respect to the surface of the inorganic slabs, resulting in a larger distance between them, as depicted in **Figure 3.10**.

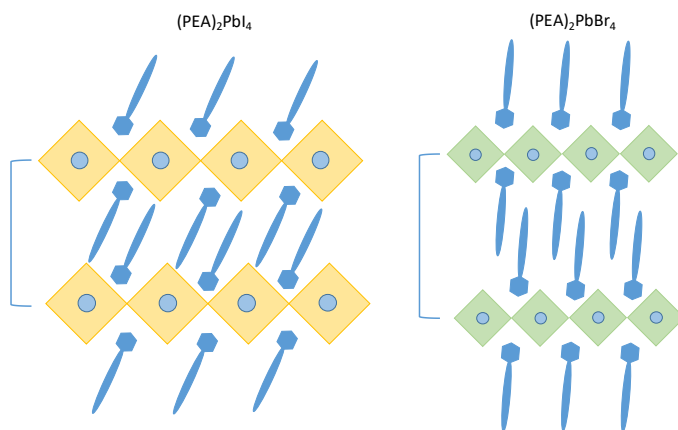


Figure 3.10. Scheme of 2D perovskite structures with different inorganic slabs distances, consequence of the octahedra contraction when substituting larger (left) with smaller halides (right).

As is clearly observable in **Figure 3.8**, in all 2D perovskite films the c -axis diffraction signals dominate the diffraction patterns, with a preferential orientation along the $[001]$ direction. This preferential orientation suggests that the 2D perovskite films grow with the alternating organic and inorganic sheets parallel to the substrate's plane. Such orientation is common for 2D perovskite, but not favorable for charge transport within a thin film device.^{101,105–107}

In the case of the $(\text{PEAI})_2\text{PbBr}_2$ film prepared from co-sublimation of PEA I and PbBr_2 , one can also note the intense reflections for the (010) and (020) planes at $2\theta = 7.8^\circ$ and $2\theta = 15.6^\circ$, respectively, as well as a broad signal around $2\theta = 12.8^\circ$, which can be attributed to a combination of (1-11) and (-1-12) planes, or from unreacted PbI_2 . Hence, it appears that this sample does form but with a less pronounced orientation. The morphology of the vacuum deposited 2D perovskite films was studied by scanning electron microscopy (SEM) and atomic force microscopy (AFM), shown in **Figure 3.11** and **Figure 3.12**, respectively.

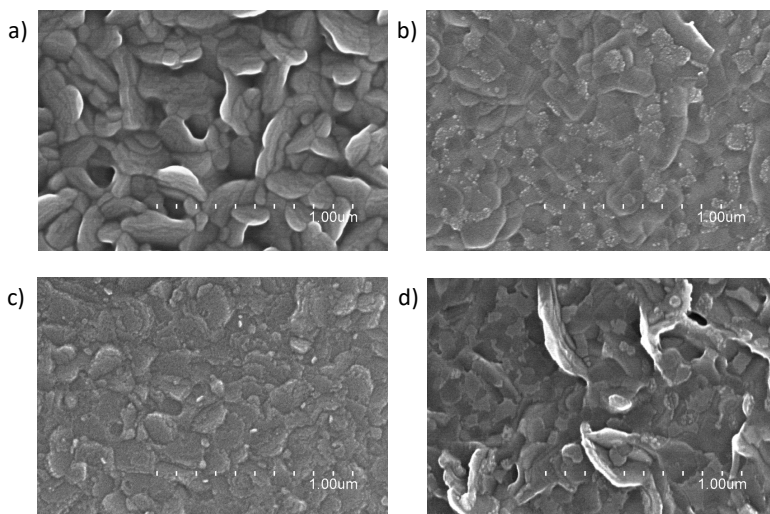


Figure 3.11. SEM pictures of vacuum deposited (a) $(\text{PEA})_2\text{PbI}_4$ (b) $(\text{PEA})_2\text{PbBr}_4$ c) $(\text{PEABr})_2\text{PbI}_2$ and d) $(\text{PEAI})_2\text{PbBr}_2$ thin-films. The scale bar in all SEM images is 1 μm .

The SEM of the $(\text{PEA})_2\text{PbI}_4$ perovskite (**Figure 3.11a**) shows well-defined, randomly distributed platelets formed by multiple grains with sizes ranging from 200 nm to 400 nm. The surface was found to be rather rough, with a high root-mean-square roughness and average height, see **Table. 3.2** and **Figure 3.12a**.

The pure bromide $(\text{PEA})_2\text{PbBr}_4$ films are also characterized by the presence of platelets, although these are more compact compared to the iodide counterparts (**Figure 3.11b**). The grain size is in the range of hundreds of nanometres and the topography is characterized by a reduced R_{RMS} and a Z_{AVG} as can be seen in **Table 3.2** and **Figure 3.12b**. The morphology and grain size of the mixed $(\text{PEABr})_2\text{PbI}_2$ perovskite films were found to be very similar to that of the pure bromide compound, although with a much flatter topography, as described in **Table 3.2**. Finally, the $(\text{PEAI})_2\text{PbBr}_2$ films (**Figure 3.11d**) show the most heterogeneous morphology, with small platelets and large lamellar aggregates, resulting in a very rough surface, reflected in high R_{RMS} and Z_{AVG} values (**Table 3.2** and **Figure 3.12d**).

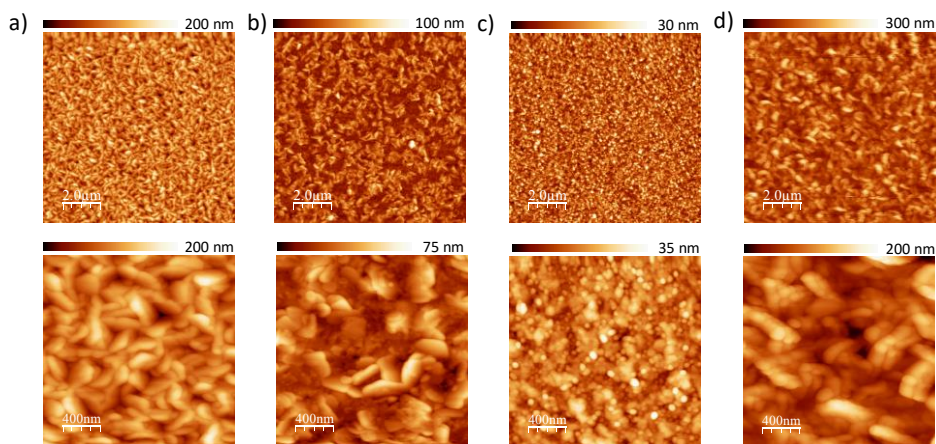


Figure 3.12. AFM topographies at different magnifications of a) PEA_2PbI_4 , b) $\text{PEA}_2\text{PbBr}_4$, c) $(\text{PEABr})_2\text{PbI}_2$ and d) $(\text{PEAI})_2\text{PbBr}_2$ 2D perovskite thin films.

Sample	R_{RMS} (nm)	Z_{AVG} (nm)
(PEA) ₂ PbI ₄	25.8	95.0
(PEA) ₂ PbBr ₄	10.9	28.3
(PEABr) ₂ PbI ₂	4.0	14.1
(PEAI) ₂ PbBr ₂	29.2	74.8

Table 3.2. Root-mean-square roughness R_{RMS} and average height Z_{AVG} as calculated from the AFM analysis for the different 2D perovskite thin-films.

The steady state optical characterization of the vacuum-deposited 2D perovskite films is presented in **Figure 3.13**. The optical absorption of the (PEA)₂PbI₄ films shows a band in the UV and an intense excitonic peak, typical of the 2D perovskite, centered at 503 nm, with a full width at half maximum (FWHM) of 35 nm. When the film of (PEA)₂PbI₄ was excited with a LED at 340 nm, intense photoluminescence centered at 521 nm was observed, as shown by the yellow dashed line (**Figure 3.13a**). The peak has a FWHM of 24 nm and a Stokes shift of 80 meV. The (PEA)₂PbBr₄ film exhibit the expected optical absorption band at higher energy, compared to the analogous iodide compound, with a very sharp excitonic peak (FWHM=15 nm) centered at 403 nm. Another weak absorption band was detected at 434 nm, which cannot be ascribed to the pure (PEA)₂PbBr₄ phase. An intense and narrow photoluminescence centered at 410 nm and with a FWHM of 17 nm was observed, with a small Stokes shift of 60 meV. However, other two peaks were systematically detected in the PL spectrum, a low intensity peak centered at 434 nm and a more intense and broad band centered at 507 nm (**Figure 3.13b**).

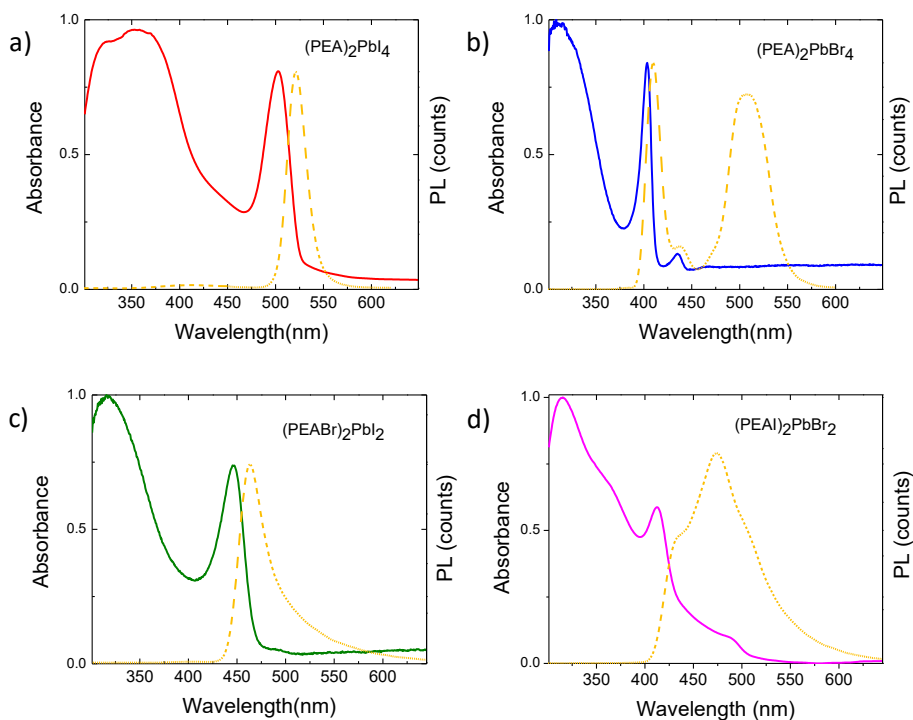


Figure 3.13. Optical absorption and photoluminescence spectra (excitation at 340 nm) of 200 nm thick films of (a) $(\text{PEA})_2\text{PbI}_4$, (b) $(\text{PEA})_2\text{PbBr}_4$, (c) $(\text{PEABr})_2\text{PbI}_2$ and (d) $(\text{PEAI})_2\text{PbBr}_2$ perovskites.

Most likely, the additional small intensity peak can be associated to the presence of a bromide-rich, mixed bromide/iodide phase, while the broad PL band at lower energy can be ascribed to the formation of an iodide-rich phase. This may be the result of a possible halide cross-contamination in the evaporation chamber, which was used for the vacuum processing of both $(\text{PEA})_2\text{PbBr}_4$ and PEA_2PbI_4 perovskites. In order to verify this hypothesis, energy-dispersive X-ray spectroscopy (EDS) was used to determine the material composition. In the 2D $(\text{PEA})_2\text{PbI}_4$ films, an I/Br ratio of 14.3 was found, indicating that approximately 6% of the total halide content consists of the bromide. In the case

of $(\text{PEA})_2\text{PbBr}_4$, the Br/I ratio was as low as 3.5, meaning that as much as 22% of the total halide content is due to iodide contamination. The EDS analysis justified the observed optical properties of the perovskite film, and clearly indicates that there is cross-contamination between the different precursors from different vacuum-deposition runs. Interestingly, in the case of the 2D $(\text{PEA})_2\text{PbI}_4$ films there is a rather low bromide contamination, while the contamination of iodide in $(\text{PEA})_2\text{PbBr}_4$ films is more relevant. The contamination can be due to i) re-evaporation of previously deposited materials from the surface of the chamber or even to ii) halide exchange between the subliming vapors and the chamber itself. These processes can be more or less pronounced depending on the volatility of the materials as well as on their chemical reactivity, and poses a challenge that should be taken into account in the vacuum-deposition of perovskites. The optical absorption of the mixed halide $(\text{PEABr})_2\text{PbI}_2$ perovskite (**Figure 3.13c**) deposited by dual source sublimation of PEABr and PbI_2 , was found to be blue shifted with respect to that of the $(\text{PEA})_2\text{PbI}_4$ and red-shifted compared to $(\text{PEA})_2\text{PbBr}_4$, as expected for a mixed halide perovskite. The excitonic absorption was centered at 446 nm (FWHM = 36 nm), while the PL peak was found to be asymmetric with a maximum at 464 nm (FWHM= 34 nm), implying a large Stokes shift of 110 meV. The EDS analysis revealed a Br/I ratio of 0.9, very close to the expected stoichiometry for the $(\text{PEABr})_2\text{PbI}_2$ perovskite and with only a negligible excess of iodide. At this halide ratio, 3D perovskites usually show halide segregation effects,¹⁰⁸ due to the poor miscibility of the iodide and bromide phases. For this reason, we studied the evolution of the PL over time under continuous laser irradiation at 375 nm. Immediately after illumination, we noted the presence of the previously observed high energy peak at 464 nm with a weak component at lower energy (approximately 500 nm). With continuous irradiation, the low energy component dominates the PL spectrum, implying the formation of iodide-rich phases where carriers are efficiently

transferred and radiatively recombine (**Figure 3.14**). This is hence in agreement with what generally observed for other mixed halide perovskites.

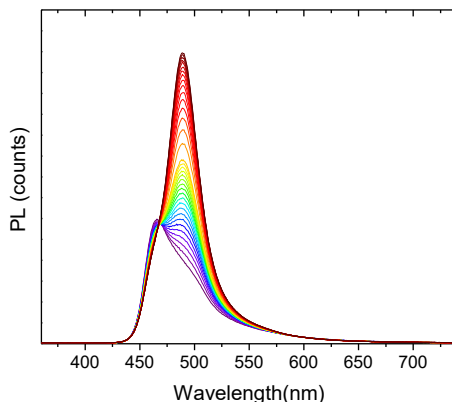


Figure 3.14. Evolution of the photoluminescence spectra of the $(\text{PEABr})_2\text{PbI}_2$ thin film under continuous excitation with a CW laser at 375 nm. Each spectrum is collected every 10 s, going from purple to dark red.

Rather different optical properties were observed for the other mixed halide $(\text{PEAI})_2\text{PbBr}_2$ perovskite films, obtained by simultaneous sublimation of PEAI and PbBr_2 . The absorption spectrum in **Figure 3.13d** show an excitonic peak at 412 nm, close to that of the pure bromide compounds $(\text{PEA})_2\text{PbBr}_4$, and a weak absorption at approximately 490 nm, which is close to the excitonic absorption of the pure iodide $(\text{PEA})_2\text{PbI}_4$ perovskite. This behavior suggests the coexistence of different domains, as also confirmed by the PL spectrum, which shows a broad band composed of several peaks: one with a maximum at approximately 434 nm and a second, more intense at 475 nm with a shoulder around 504 nm. The optical characteristics are consistent with the presence of a dominant, bromide-rich phase and of a second iodide-rich one. This hypothesis is supported by the elemental analysis, which revealed a Br/I ratio of 1.8, implying that

approximately 65% of the halide consists of bromide. The high bromide content of the $(\text{PEAI})_2\text{PbBr}_2$ films could also partially explain why the corresponding unit cell parameters are close to those of the $(\text{PEA})_2\text{PbBr}_4$ (**Table 3.1**). When the PbBr_2 is reacting with the PEAI during the co-deposition process, the halide exchange is limited to an iodide inclusion of about only 30-40 mol%. On the other hand, the co-deposition of PbI_2 and PEABr was found to lead to perovskites with a well-balanced halide content. This phenomenon could be ascribed either to a higher chemical reactivity of PEABr, or to a higher stability of PbBr_2 compared to PbI_2 . Some literature points towards the latter hypothesis, as the energetic stability of lead halides increases with increasing halide electronegativity (from iodide to bromide).^{109,110} The vacuum-deposited 2D perovskite films were further studied by means of time-resolved microwave conductivity.

3.6 Time-Resolved Microwave Conductivity

The Time-Resolved Microwave Conductivity (TRMC) technique can be used to study the mobility, the photoconductance (ΔG) and lifetimes of photo-generated charge carriers in semiconductors. Additionally, analysis of TRMC data provides the understanding of recombination mechanisms and defect densities. The TRMC is based on the interaction between the electric field component of microwaves (GHz regime) and mobile charge carriers. Pulsed laser light at various wavelengths in the microwave cavity is used to excite electrons from the VB to the CB of the perovskite. Absorption of microwaves by photo-induced charges reduces the microwave power P on the detector.

The normalized reduction in microwave power P ($\Delta P / P$) is related to ΔG by:

$$\frac{\Delta P}{P} = -K\Delta G \quad (3.1)$$

in which K is the sensitivity factor. Considering that both electrons and holes contribute to the photoconductance, ΔG is proportional to the sum of both their concentration and mobility, as shown in equation 3.2

$$\eta \sum \mu = \frac{\Delta G}{I_0 e \beta} \quad (3.2)$$

where η indicated the incident photon, $\sum \mu$ is the sum of electron and hole mobility, I_0 is the incident intensity, e is the elementary charge, and β is the geometrical factor.

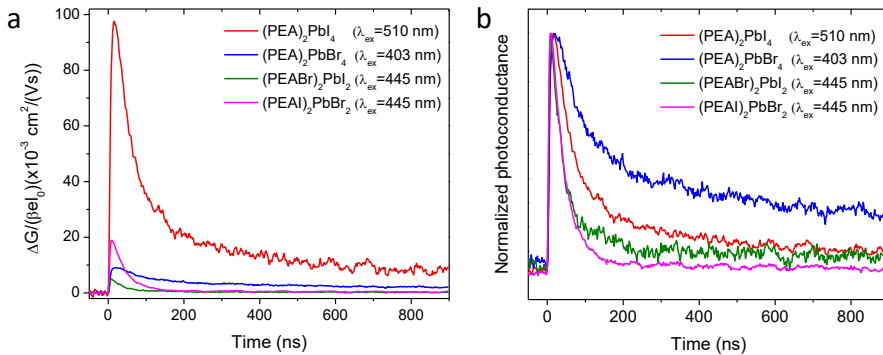


Figure 3.15. a) Time-resolved microwave conductivity traces of vacuum-deposited 2D perovskite selectively excited at 510, 403 and 445 nm. b) normalize time-dependent photoconductance of the same sample series.

Figure 3.15 shows the time-dependent photoconductivity traces for all the 2D perovskites reported in this Chapter. Three different excitation wavelength (pulsed laser excitation at 510 nm, 403 nm and 445 nm) were applied according to the maximum absorption at the excitonic peak of each compound. Upon excitation, electron-hole pairs are generated within the inorganic sheets of the 2D perovskite and, due to the strong confinement (large E_b), they will mostly exist as bound excitons, hence not contributing to the photoconductance. This is important as in these compounds the TRMC signal is not directly a measure of the charge mobility, but rather its product with the free carrier generation yield.¹¹¹ From the maximum change in TRMC signal (**Figure 3.15a**), recorded with an excitation density on the order of 10^{12} photons/cm², we can immediately observe that the pure iodide 2D compound (PEA)₂PbI₄ present a larger photoconductance (0.1 cm²/Vs) as compared to the bromide and mixed halide analogues. The photoconductance of (PEA)₂PbI₄ is consistent with the low yield of excitons dissociating into mobile carriers, and is comparable to previously reported values for similar solution-processed 2D perovskite films.¹¹¹ The lower absolute photoconductance observed for (PEA)₂PbBr₄ and mixed (PEABr)₂PbI₂ and (PEAI)₂PbBr₂ film can be ascribed to the lower crystal/grain size, as observed by electron microscopy (**Figure 3.11**). Among these materials, the larger grains in the (PEAI)₂PbBr₂ films might hence be responsible for the slightly higher photoconductance observed for this specific compound (0.02 cm²/Vs). In order to evaluate the charge carrier recombination, the TRMC traces were normalized (**Figure 3.15b**) allowing a direct comparison of the recombination lifetime $t_{1/2}$ (time after excitation when the charge carrier concentration drops to 1/2 of its initial value). Interestingly, the pure bromide (PEA)₂PbBr₄ perovskite showed a longer lifetime (160 ns) compared to the pure 2D iodide films ($t_{1/2} = 70$ ns). This trend is somewhat unexpected, as E_b was reported to increase when moving from iodide to bromide perovskites, implying

a lower photoconductance but also a lower lifetime for bromide compounds.¹¹² The larger lifetime is hence most likely correlated with the presence of iodide in $(\text{PEA})_2\text{PbBr}_4$, acting as carrier traps and causing slower charge recombination within the material. Finally, the overall lower lifetimes observed for the mixed compounds (40 ns) correlates with an increased disorder due to the presence of mixed halide domains. In all cases the lifetime values observed here well compare with the literature data.¹¹¹

3.7 Conclusion

In this Chapter, the vacuum-deposition and characterization of Ruddlesden-Popper perovskites, as well as of pure and mixed halide 2D perovskites have been reported. The evaporation of the organic salts at their minimum sublimation temperature resulted in stable rates, which allowed the deposition of 2D perovskites. The 2D PEA_2PbX_4 perovskite films, where X stands for I, Br, or a combination of both, exhibited the expected trend in bandgap, increasing from the pure iodide to the pure bromide materials, and in between these two extremes for the mixed halide compounds. Upon analyzing the perovskite films from consequential sublimation of iodide and bromide precursors, it became clear that some halide cross-contamination is occurring. This has implications in particularly for the fabrication of wide bandgap perovskite films, such as $(\text{PEA})_2\text{PbBr}_4$, because the presence of iodide unavoidably results in multiple luminescence features due to the heterogeneous energy landscape within the semiconductor film. Hence it is recommended to use a dedicated chamber for a given composition in order to ensure the formation of high purity perovskite compounds. During the preparation and study of the mixed I/Br 2D perovskites by co-sublimation of either PEAI and PbBr_2 or vice versa, a Br/I 1:1 stoichiometry was only obtained when using PbI_2 and PEABr ,

most likely due to the higher reactivity of PbI_2 (as compared to the more stable PbBr_2) towards the organic cations. This is another important observation to be considered when designing vacuum deposition of low-dimensional, mixed halide compounds. The 2D perovskites were also analyzed by time-resolved microwave conductivity (TRMC). The pure iodide PEA_2PbI_4 showed photoconductance and lifetime values in agreement with previously reported solution-processed thin films, making it an interesting candidate for implementation in multilayer optoelectronic devices.

Author contribution

Complete Journal article is added to Appendix 2.

La-Placa, M.-G.; Guo, D.; Gil-Escrig, L.; Palazon, F.; Sessolo, M.; Bolink, H. J. Dual-Source Vacuum Deposition of Pure and Mixed Halide 2D Perovskites: Thin Film Characterization and Processing Guidelines. *J. Mater. Chem. C* **2020**, 1902–1908. <https://doi.org/10.1039/c9tc06662d>.



Chapter 4

Vacuum-deposited 2D/3D perovskite heterojunctions

4.1 Introduction

As outlined in the first Chapter, there are several reasons behind the rapid development of optoelectronic devices based on organic-inorganic metal halide perovskites, such as their high absorption coefficient, ambipolar charge transport, easy-to-tune bandgap etc.^{113–115} These properties led to the demonstration of perovskite solar cells (PSCs) with a certified power conversion efficiency (PCE) of 25% in only 10 years of development.¹¹⁶ Despite these achievements, the efficiency is still far from the Shockley-Queisser limit of about 30% for a semiconductor with a bandgap of 1.6 eV.¹¹⁷ In order to further enhance the PCE, the effort should be focused on increasing the open-circuit voltage (V_{oc}) through the reduction of non-radiative recombination losses. Indeed, while for a

solar cell in the radiative (Shockley-Queisser) limit the only recombination channel is the radiative recombination of free electrons and holes, in a real solar cell the V_{oc} value is lower due to undesirable non-radiative recombination. Polycrystalline perovskite thin films used in high-efficiency PSCs still contain defects at the surface and at grain boundaries which are responsible of the non-radiative recombination.¹¹⁸ At the same time, defects play an important role in the permeation of moisture or oxygen into the perovskite film, accelerating the material and device degradation. Therefore, the passivation of defects located at the surface and at the grain boundaries is one of the main challenges that the PSCs technology is currently facing. Passivation of non-radiative recombination (trap) states enhances the PLQY and hence leads to an increase of the obtainable V_{oc} , since these two parameters are closely related as described in the equation 4.1.

$$eV_{oc}^{max} = QFLS = QFLS_{rad} + k_B T \ln(PLQY) \quad (4.1)$$

where e is the electron charge, V_{oc}^{max} is the maximum achievable open-circuit voltage, $QFLS$ is the quasi-Fermi level splitting, $QFLS_{rad}$ is the $QFLS$ in the radiative limit (when all charges recombine radiatively), k_B is the Boltzmann constant and T the temperature. Hence an increase in the PLQY maximizes the V_{oc} towards the QFLS in the radiative limit. Passivation of defects in perovskites have been pursued through several strategies. Among the most important ones are interface engineering using organic molecules and additives as show in Chapter 2, the use of alternative precursors or altered stoichiometry, embedding small alkali metal cations, or the use of thin organic buffer layers at the perovskite/transport material interface.¹¹⁹⁻¹²¹

More recently, several studied have highlighted passivation and stabilization through the use of wide band-gap, low dimensional perovskites in combination

with 3D perovskites. The underlying concept is to combine the high efficiency of the 3D absorber with the passivation and the stabilization properties of 2D perovskites,¹²² thanks to the hydrophobic character of the alkylammonium chains.¹²³ These bilayers can be prepared by functionalization of the 3D perovskite surface with large ammonium cations, resulting in the formation of thin low-dimensional perovskite layers.^{124,125} Alternatively, the direct processing of a 2D perovskite film on top of a preformed 3D material can also be pursued.¹²⁶ Up to now, thin 2D perovskite layers on the surface and/or at the grain boundaries of 3D perovskites have been deposited solely by solution processing, leading to unavoidable intermixing between the two phases.

In this Chapter, the fabrication of 2D/3D perovskite heterojunctions by dual-source vacuum deposition is reported. The interaction between the 3D and 2D phases as well as the charge transport properties of 2D perovskites in neat 2D/3D interfaces were studied by combining 3D (methylammonium lead iodide, MAPI) and 2D (phenethylammonium lead iodide, PEA₂PbI₄) in three different perovskite heterostructures: i) 2D/MAPI/2D, ii) 2D/MAPI, iii) MAPI/2D. All these structures have been integrated into vacuum-deposited PSCs in order to rationalize the role of each interface.

4.2 Thin-film 2D/3D heterostructure preparation

The organic ammonium salts C₈H₁₂IN (PEAI) and CH₃NH₃I (MAI) were purchased from Lumtec. PbI₂ was purchased from Tokyo Chemical Industry CO (TCI). All materials were used as received. The ITO-coated glass and glass substrates were cleaned as explained in the previous Chapters. The 2D PEA₂PbI₄ thin films were deposited in the vacuum chamber showed in **Figure 3.1** following the process described in the Chapter 3 of this thesis. The 3D MAPI perovskite films were deposited in a dedicated vacuum chamber equipped with

six temperature-controlled evaporation sources (Creaphys) fitted with ceramic crucibles (**Figure 4.1**). Three quartz crystal microbalance sensors were used: two monitoring the deposition rate of each evaporation source and a third one close to the substrate holder monitoring the total deposition rate. MAI and PbI_2 were co-sublimed at temperatures ranging from 140 to $>300^\circ\text{C}$, respectively, to form the 3D perovskite with a total thickness of 500 nm. The samples were transferred from one chamber to the other by means of portable chambers filled with nitrogen.



Figure 4.1. Picture of the vacuum chamber employed for the deposition of the MAPI perovskite films.

4.3 2D/3D heterostructure: characterization

In order to investigate the influence of the 2D perovskite layers on the morphology and crystallinity of the 3D perovskite, 10 nm thick PEA_2PbI_4 films were initially deposited below and on top of a 500 nm thick MAPI film. The comparison of X-ray diffraction patterns of the bare 3D perovskite and of one sandwiched between 2D perovskite layers is shown in **Figure 4.2**, where all the reflections of the reference sample (MAPI on glass) are indexed. As commonly

observed for both solution-processed and vacuum-deposited MAPI,^{127,128} a preferential orientation occurs along the [110] direction. However, when the MAPI film is deposited in between two PEA₂PbI₄ layers, we observed a decrease in the intensity of the (110) and (220) peaks and an increase of the intensity of the (022) and (134) reflections. These observations suggest a change in the orientation of the MAPI film when deposited between 2D perovskite layers. The change of the diffraction profiles together with their enlarged FWHMs also indicates a reduction of the crystal size for the MAPI film.

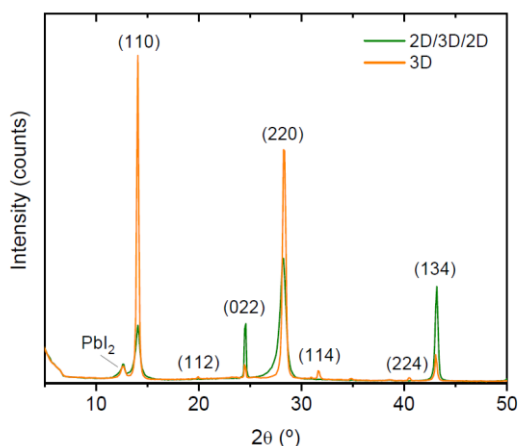


Figure 4.2. X-ray diffraction patterns of vacuum deposited MAPI film (3D) and of the PEA₂PbI₄/MAPI/PEA₂PbI₄ heterostructure (2D/3D/2D).

The peak at low angle ($2\theta = 12.7^\circ$) is ascribed to the presence of unreacted PbI₂, both in the pure MAPI and in the 2D/MAPI/2D heterostructure. It is interesting to note that in several reported solution-processed 3D/2D perovskite systems, an excess of PbI₂ in the 3D compound is intentionally used to then form a low-dimensional perovskite by simple spin-coating of the corresponding organic ammonium halide.¹²² In our case, the excess PbI₂ in the MAPI film is maintained

even after deposition of the 2D PEA_2PbI_4 film. Considering that no PbI_2 diffraction could be observed in pure PEA_2PbI_4 films (**Figure 4.3**), it implies that the PbI_2 signal comes only from the underlying MAPI layer. These observations suggest that no intermixing takes place between the two materials, resulting in a neat 3D/2D perovskite interface.

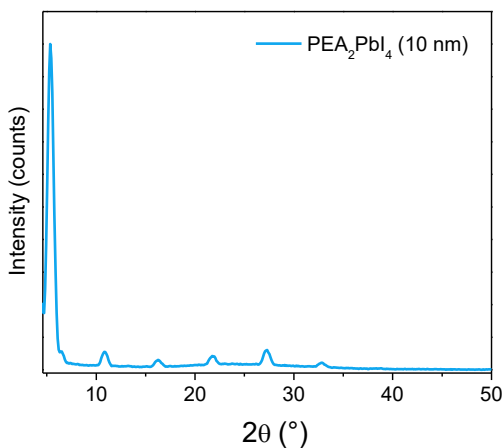


Figure 4.3. XRD pattern of a vacuum deposited, 10 nm thick PEA_2PbI_4 perovskite film

The formation of a pure PEA_2PbI_4 film at the interface with MAPI was also confirmed by the photoluminescence (PL) of the 2D/3D bilayer (**Figure 4.4**). The PL spectrum was recorded upon laser excitation at 375 nm on the back side of the glass substrate, where the 3D layer was deposited on top of the 2D film (glass/2D/3D). The high energy peak centered at 523 nm is in agreement with the presence of a pure PEA_2PbI_4 perovskite, while the peak at 768 nm is a signature of the 3D MAPI perovskite.

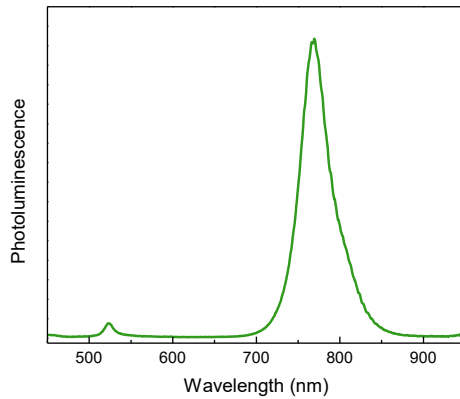


Figure 4.4. PL spectrum upon laser excitation at 375 nm of a 2D/3D bilayer.

On the other hand, no changes were observed in the optical absorption of the 2D/MAPI/2D heterostructure compared with the bare MAPI, as highlighted in **Figure 4.5**. In the optical absorption, the contribution of the very thin 2D perovskite film is not detectable because of the very high absorbance of MAPI in the green-blue region of the spectrum.

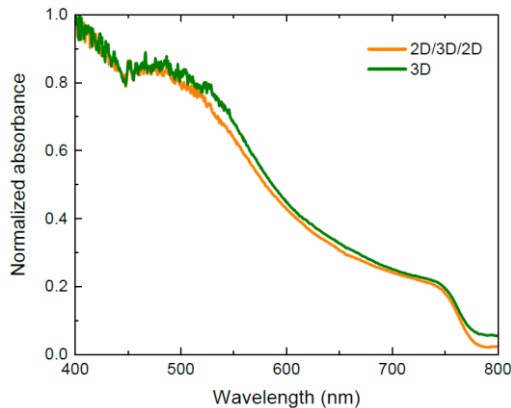


Figure 4.5. Optical absorption of a 3D MAPI film and a 2D/3D/2D perovskite heterostructure.

The morphology of the bare 3D layer and of the 3D film sandwiched in between of the 2D perovskite was investigated by SEM and AFM (**Figure 4.6**). The surface of the MAPI film in **Figure 4.6a** appears homogeneous and compact with an average grains size of approximately 100 nm. In the case of the 2D/3D/2D heterostructure (**Figure 4.6b**), it appears that the presence of the PEA_2PbI_4 layer affects the film growth and the morphology of the 3D perovskite. In fact, the surface appears more textured compared to the reference MAPI film and the grain size is slightly reduced, in agreement with the XRD reported in **Figure 4.2**.

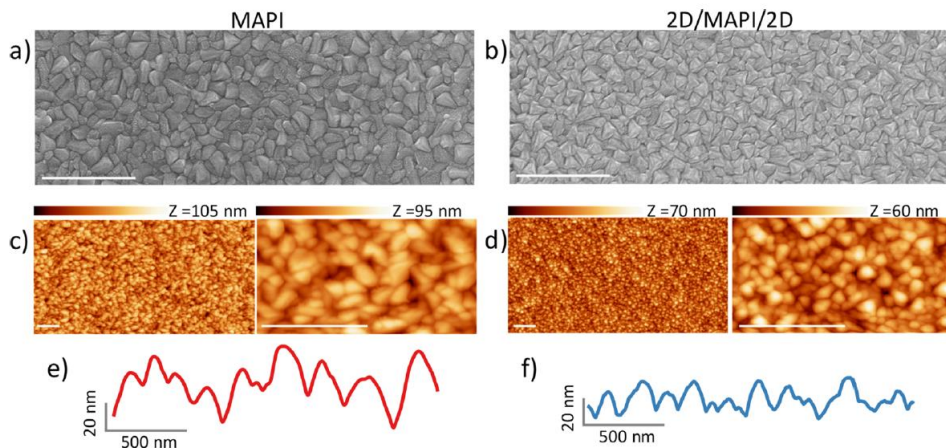


Figure 4.6. SEM images and AFM topographies at different magnifications of (a,c) a MAPI film and of (b,d) a 2D/MAPI/2D heterostructure. (e,f) AFM profiles for the same samples. The scale bar in all SEM and AFM images is 1 μm .

The MAPI surface analyzed by AFM (**Figure 4.6c**) was found to be rather rough, with a root-mean-square roughness R_{RMS} of 13 nm and average height Z_{AVG} as high as 50 nm (**Figure 4.6e**). The grain size reduction observed by SEM for the 2D/MAPI/2D heterostructure was confirmed by AFM (**Figure 4.6d**), where the

topography presented a R_{RMS} of 8 nm and a strongly diminished Z_{AVG} of 27 nm (**Figure 4.6f**). Moreover, in the case of the 2D/MAPI/2D heterostructure, the height distribution was found to be narrower, indicating a more homogeneous surface compare to the bare MAPI.

4.4 2D/3D heterostructure: solar cell application

The heterostructure described above were incorporated in fully vacuum-deposited PSCs in order to study their photovoltaic properties. The low-dimensional PEA_2PbI_4 films were deposited in between the HTL/MAPI, the MAPI/ETL or both HTL/MAPI/ETL interfaces, and then integrated in a p-i-n device configuration depicted in **Figure 4.7a**. Also in this case, patterned ITO-coated glasses were used as transparent electrodes. After cleaning they were transferred to the vacuum-chamber where all layers were thermally deposited in high vacuum with a base pressure of 10^{-6} mbar. Molybdenum oxide (MoO_3 , 5 nm) and *N4,N4,N4'',N4''*-tetra([1,1'-biphenyl]-4-yl)-[1,1':4',1''-terphenyl]-4,4'' diamine (TaTm, 10 nm) were used as HTLs while fullerene (C_{60} , 25 nm) and bathocuproine (BCP, 8 nm) were used as ETLs. The deposition rates for TaTm and C_{60} were 0.5 Å/s, while a rate of 0.3 Å/s was used for the thinner BCP layer. The transport layers were sublimed in the vacuum chamber shown in **Figure 4.1**. The devices were completed with the deposition of 100 nm thick silver electrode. MoO_3 and Ag were evaporated in a separated vacuum chamber using tantalum boats and applying currents ranging from 2.0 to 4.8 A. For all the devices, the MAPI thickness was kept constant (500 nm) while varying the PEA_2PbI_4 thickness between 2.5 nm and 10 nm.

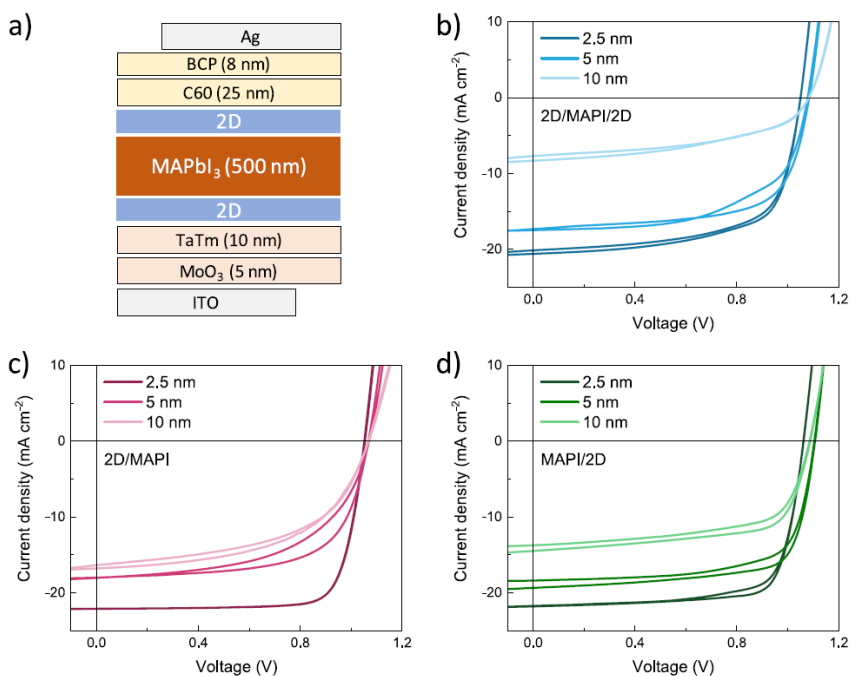


Figure 4.7. a) Scheme of the p-i-n solar cells employing a perovskite heterostructure as the active layer. J-V curve under 100 mW cm^{-2} illumination of the b) 2D/MAPI/2D, c) 2D/MAPI, and d) MAPI/2D heterojunction solar cells for different PEA₂PbI₄ layer thicknesses.

The first heterojunction that was tested and implemented in a PSC was the triple layer 2D/MAPI/2D with 2.5 nm thick 2D films. The device showed a short-current density (J_{sc}) exceeding 20 mA cm^{-2} , only slightly lower than that of the reference MAPI solar cell (**Table 4.1**), and a very similar open-circuit voltage (V_{oc}) of 1050 mV. The fill factor (FF), however, was strongly reduced at 65.5%, which is surprising considering that the 2D perovskite films were only 2.5 nm thick.

Perovskite structure		V_{oc} [mV]	J_{sc} [mA cm ⁻²]	FF [%]	PCE [%]
MAPI	<i>fwd</i>	1057	22.7	77.2	18.6
	<i>rev</i>	1056	22.7	78.5	18.9
2D/MAPI/2D	<i>fwd</i>	1050	20.1	65.5	13.9
	<i>rev</i>	1050	20.6	66.0	14.3
2D/MAPI	<i>fwd</i>	1054	22.1	78.4	18.3
	<i>rev</i>	1051	22.1	78.6	18.3
MAPI/2D	<i>fwd</i>	1062	21.7	73.5	17.0
	<i>rev</i>	1061	21.8	76.6	17.7

Table 4.1. Performance parameters extracted from the J–V characteristics of p–i–n PSCs of the control MAPI absorber device and of 2D/MAPI/2D-, 2D/MAPI-, and MAPI/2D-based solar cells with 2.5 nm thick PEA₂PbI₄ 2D films

Increasing the thickness of the low-dimensional perovskite films results in a further decrease of the FF to 49.7%, accompanied by a drastic reduction in the current density, to values as low as 8 mA cm⁻² for devices including 10 nm thick 2D films. Clearly, the 2D/MAPI/2D heterojunction solar cells suffer from hindered charge extraction, a situation that becomes more severe for thicker 2D films. This is in agreement with the formation of PEA₂PbI₄ films with insulating sheets perpendicular to the current flow, as described in the Chapter 1 of this thesis. All solar cells based on the 2D/MAPI/2D heterostructure showed a hysteresis in the J–V curve when scanning in forward (from short- to open-circuit) or reverse (from open- to short-circuit) bias. However, the V_{oc} for the devices employing 5 and 10 nm thick PEA₂PbI₄ films was found to increase up to >1080 mV, meaning that the 2D films are indeed capable of reducing non-radiative recombination within the MAPI layer.

In order to rationalize the properties of the 2D/MAPI/2D heterostructures and devices, analogous solar cells based on either 2D/3D or 3D/2D bilayers were fabricated and characterized as a function of the thickness of the PEA_2PbI_4 films. Solar cells with the 2.5 nm thick 2D film at the front contact (2D/MAPI) shows a high J_{sc} of 22.1 mA cm^{-2} and very good rectification, with a FF as high as 78.6% and negligible hysteresis. The V_{oc} is approximately 1.05 V, leading to a PCE of 18.3%, comparable to that of the reference MAPI solar cells. Also in this heterojunction configuration, increasing the thickness of PEA_2PbI_4 to 5 and 10 nm results in lower photocurrent (18 and 16.5 mA cm^{-2} , respectively) and causes again a drastic reduction of the FF, which is below 55% for both thicknesses, as shown in **Figure 4.7c**. The cells with thicker 2D films show also hysteresis in the J–V curve. However, when compared to bare MAPI devices, the solar cell photovoltage is also found to increase to about 1070 mV for thicker 2D perovskite films. A similar behavior was observed for the solar cells with the 2D film at the back contact, where PEA_2PbI_4 is deposited on top of MAPI and below C60 (3D/2D), as shown in **Figure 4.7d**. The current density decreases with increasing thickness of the 2D perovskite films, from 21.8 mA cm^{-2} (2.5 nm) to approximately 14 mA cm^{-2} (10 nm). The J–V curves for devices with thicker (5 and 10 nm) 2D films show more hysteresis. Also for the MAPI/2D heterojunction, the FF was observed to scale inversely with the thickness of PEA_2PbI_4 but not as drastically as in the case of 2D/MAPI structures. The FF decreases from 73.5% to 63.9% when the 2D layer thickness is increased from 2.5 nm to 10 nm. Importantly, with this device configuration, we do observe a substantial increase in the photovoltage, with the MAPI/2D solar cells having a V_{oc} exceeding 1.1 V for 5 nm thick PEA_2PbI_4 layers. This observation indicates that the 2D perovskite layer is indeed capable of reducing the non-radiative recombination within the MAPI film. Interestingly, the fact that no changes in photovoltage were observed with the 2D/MAPI heterojunction (as compared to

bare MAPI) might indicate that the chemistry of the 2D/3D interface differs from that of the 3D/2D one. The trend of the V_{oc} and FF for the different configurations and as a function of the 2D film layer thickness is reported in **Figure 4.8**. In general, devices including 2.5 nm thick PEA_2PbI_4 films do not show an appreciable variation of the photovoltage compared to the reference MAPI cells (1055 mV), while these thin 2D films already undermine the charge extraction (deduced from a diminishing FF). One exception is the 2D/3D heterojunction, where the V_{oc} and FF are essentially unchanged with respect to the reference MAPI solar cells, leading to similar PCE exceeding 18%.

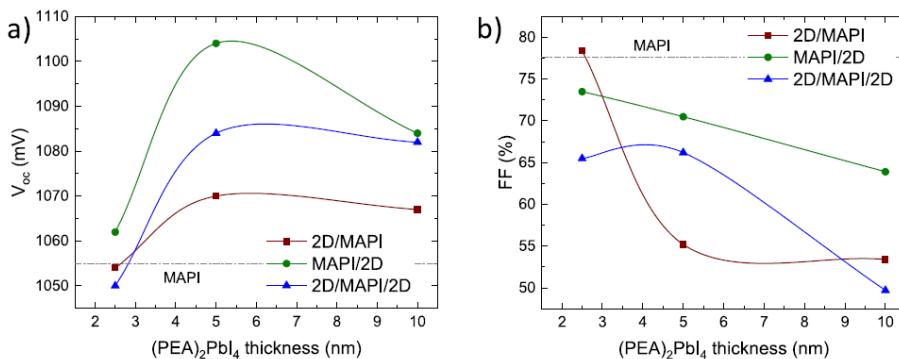


Figure 4.8. Trend of the a) V_{oc} and b) FF for the three different heterojunction solar cells as a function of the 2D PEA_2PbI_4 perovskite layer thickness. The dotted lines represent average values for single-layer MAPI reference devices.

Increasing the 2D layer thickness to 5 nm leads to a general enhancement of the V_{oc} , with the devices based on the 2D/3D and 2D/3D/2D structures reaching 1070 and 1084 mV, respectively, and a peak for the 3D/2D heterojunction solar cells at 1104 mV. While such a 50 mV increase in V_{oc} might appear moderate, it corresponds to a 7-fold enhancement of the external PLQY.^{87,129} Hence, the vacuum-deposited PEA_2PbI_4 films on top of MAPI are indeed capable of

reducing non-radiative charge recombination, although at the expense of the FF (70%). For thicker (10 nm) 2D films, we observed a reduction of the V_{oc} , which is more prominent for the 3D/2D heterojunction with a 10 nm thick film. Although the incorporation of 2D perovskites at the interface with MAPI is beneficial for the obtainable photovoltage, it leads to a drop in FF, which became more important once the PEA_2PbI_4 thickness increased from to 5 and 10 nm. The loss in FF can be attributed to the unfavorable orientation of the insulating sheets formed by the bulky organic cations within the 2D perovskite films (**Figure 4.3**), perpendicularly oriented to the direction of the charge transport, as mentioned before. Besides the orientation of the 2D perovskite with respect to the substrate, another factor that can contribute to the loss in FF is the presence of an energy barrier for the charge extraction (either hole or electron, or both) at the 3D/2D heterojunction or at the perovskite/organic interfaces. Such an energy barrier is related to misalignment of the energy levels, which is likely to exist at least in one case (either 2D/3D or 3D/2D) as a consequence of the larger bandgap of PEA_2PbI_4 as compared to that of MAPI. The ionization energy (IE) is an estimate of the valence band maximum (VBM) in an intrinsic semiconductor. Via air photoemission spectroscopy (APS) the IE of both 3D and 2D perovskite were measured, and their flat band energy diagram was calculated (**Figure 4.9**). From the APS measurement for the MAPI perovskite we observed an IE of 5.0 eV, only slightly smaller compared to recently reported ultraviolet photoemission spectroscopy measurements,¹³⁰ while a larger IE of 5.5 eV was measured for PEA_2PbI_4 films. This implies the presence of an energy barrier for the hole extraction of approximately 0.5 eV, which supports the severe drop in FF observed when PEA_2PbI_4 is deposited in between the HTL and the MAPI (**Figure 4.7b**).

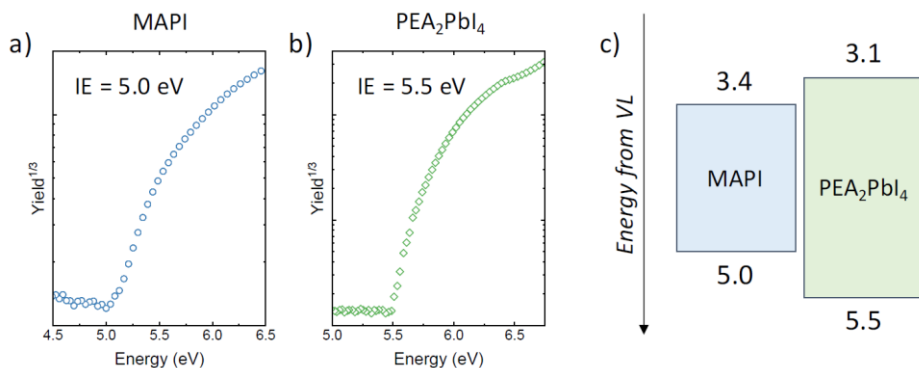


Figure 4.9. Air Photoelectron spectroscopy for vacuum deposited a) MAPI and b) PEA₂PbI₄ thin films. c) Flat band energy diagram with measure ionization energies (IE) and estimated electron affinity taking into account the bandgap of the two materials.

Estimating the bandgap of PEA₂PbI₄ at 2.4 eV from the absorption spectrum (**Figure 3.13a**, Chapter 3) and considering a MAPI bandgap of 1.6 eV,¹³⁰ the barrier for the electron extraction at the 3D/2D interface would be 0.3 eV (**Figure 4.9**). The lower energy difference among the electronic affinities at the 3D/2D interface agrees with the smaller FF losses associated with using the 2D perovskite on top of the MAPI surface and below the ETL. The vacuum-deposited 2D/3D heterostructures, together with the bare 3D and 2D perovskites, were further studied by means of time-resolved microwave conductivity, described in the Chapter 3

The normalized time-dependent conductance traces for bare MAPI and 2D/MAPI bilayers (**Figure 4.10**) were obtained by selectively exciting the perovskite films at 600 nm from two different sides: i) from the quartz substrate side (on which the perovskite was deposited), ii) from the film side. The normalized TRMC traces allow to compare the charge carrier decay for the different perovskite based films. No appreciable signal from the 2D perovskite was observed as it does not absorb light at 600 nm.

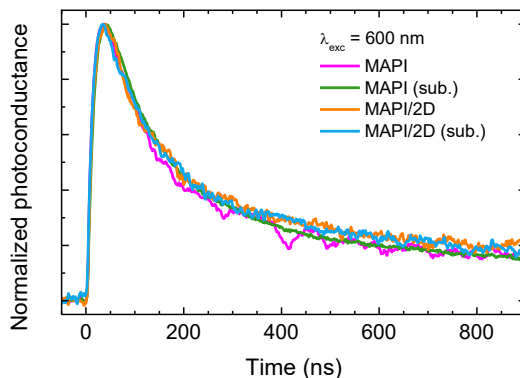


Figure 4.10. Normalized change in conductance for a MAPI film and a 2D/MAPI bilayer deposited on quartz, measured by TRMC with an incident laser pulse of 10^{11} photons/cm². The annotation (sub.) denotes that the light is shined through the quartz substrate.

After a fast initial rise limited by the response time of the microwave cavity, the signals decayed due to charge recombination or trapping. Interestingly, the decay kinetics of the MAPI and 2D/MAPI are very similar, independently on the excitation side and on the presence of the 2D layer. Hence, from this measurement, it is not possible to conclude that the MAPI film is effectively passivated by the 2D layer. It is evident from **Figure 4.11a**, that the electron and hole mobility is directly related with the maximum change in photoconductance (ΔG , Chapter 3 equation 3.2). ΔG increase slightly with the light intensity, reaching values close to $10 \text{ cm}^2/(\text{Vs})$, which is comparable to values previously obtained for evaporated 3D perovskite layers.^{131,132} The slight difference in maximum mobility can be related to the different substrate on which the 3D MAPI layer has been deposited. Such a dependence could indicate that the 3D film contains a substantial amount of deep traps, which become saturated at higher intensities.

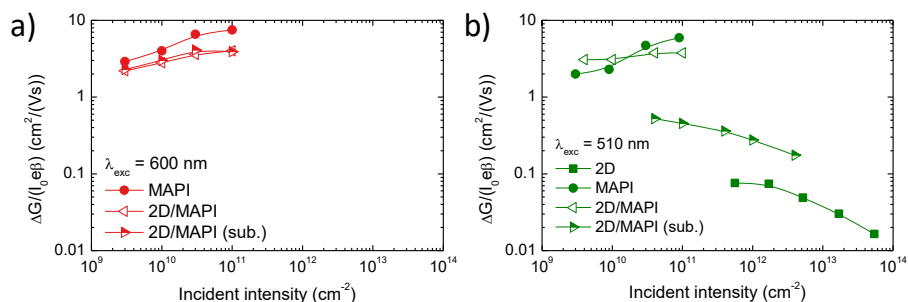


Figure 4.11. Maximum TRMC signal heights expressed in charge carrier yield times mobility for excitation at (b) 600 and (c) 510 nm at different incident light intensity. The annotation (sub.) denotes that the light is shined through the quartz substrate.

This hypothesis agrees with the higher V_{oc} values observed for the heterostructure devices, as show in **Figure 4.8a**. Finally, the samples were excited at 510 nm (**Figure 4.11b**), which corresponds with the maximum absorption of the excitonic band of the 2D perovskite (**Figure 3.13a**, Chapter 3). The 2D layer exhibited a very low signal, which is a consequence of the high exciton binding energy preventing dissociation of the excitons into mobile carriers. The MAPI films as well as the 3D/2D bilayer gave signal intensities comparable to that obtained with an excitation at 600 nm, implying that the charge carrier yield is independent on the used wavelengths. Interestingly, exciting the 2D/MAPI sample through the 2D layer leads to a substantial decrease of the signal intensity. This can be explained by the fact that a substantial part of the incident light is absorbed by the 2D perovskite itself, and the excited states generated in the 2D layer do not lead to mobile carriers in the MAPI film by either charge or energy transfer. This inefficient charge carrier generation might partially explain the photocurrent losses observed in the heterostructure solar cells (**Figure 4.7**).

4.5 Conclusion

In this Chapter, 2D phenethylammonium lead iodide (PEA₂PbI₄) films prepared by dual-source vacuum deposition were used for the fabrication of fully vacuum processed perovskite heterostructures. The PEA₂PbI₄ layers were deposited below and on top of the 3D methylammonium lead iodide (MAPI), prepared by dual-source co-deposition. The morphology, the structure and optical properties of the bare 3D and the 2D/3D/2D heterostructures were investigated. The vacuum-deposited PEA₂PbI₄ films tend to grow with the alternating inorganic and organic sheets parallel to the substrate and hence, when incorporated into devices, they lead to severely hindered charge extraction. This is a result of an interplay of different parameters, such as the preferential in-plane orientation of the 2D film, the low carrier mobility, and the mismatch in the energy levels between the 2D and 3D perovskites. By separately studying the 2D/3D and 3D/2D bilayers, we identified a trade-off between V_{oc} and FF of the solar cell. The best results were obtained for a 3D/2D heterostructure solar cell that reached an open-circuit voltage as high as 1.1 V.

Author contribution

Complete Journal article is added to Appendix 3.

La-Placa, M.-G.; Gil-Escrig, L.; Guo, D.; Palazon, F.; Savenije, T. J.; Sessolo, M.; Bolink, H. J. Vacuum-Deposited 2D/3D Perovskite Heterojunctions. *ACS Energy Lett.* **2019**, 2893–2901. <https://doi.org/10.1021/acsenerylett.9b02224>



Chapter 5

General conclusion

Two dimensional (2D) perovskites were initially studied in the 1990s but only recently they are being widely studied as semiconductors in optoelectronic devices, either as absorbing/emitting layer, as passivating agents, or as interlayers to enhance the device stability. The aim of the thesis was the application of different synthetic methods to the deposition of low dimensional perovskite films, and their application in solar cells and light-emitting diodes. Low dimensional Ruddlesden-Popper (quasi-2D) perovskites were investigated in Chapter 2 with the aim of enhancing their PLQY, which is crucial for the preparation of efficient LEDs. In order to reach that objective, the quasi-2D materials were prepared following a material engineering protocol which includes the variation of the ratio between the large (BA) and small (MA) organic cations, the modification of the solution deposition by antisolvent washing, and

the inclusion of an organic semiconductor with electro donating properties (SPPO1). The quasi-2D perovskites with a BA:MA molar ratio of 3:3, solvent engineered with SPPO1, could be deposited as highly homogeneous and pinhole-free films with a remarkable PLQY of 80%. Thanks to these characteristics, LEDs employing the quasi-2D perovskite films showed intense electroluminescence at low voltage with low leakage current, confirming the potential of this family of perovskite as photo- and electroluminescent materials. Despite the promising results, the solvent engineering protocol showed limited reproducibility, related with the control over several different processing parameters. In Chapter 3, those limitations are overcome by processing quasi-2D and 2D perovskite films by thermal vacuum deposition. The vacuum processing of these materials is still rather unexplored, but it offers many advantages over solution processing, as described in Chapter 1. Homogeneous thin-films with high crystallinity and good morphology were obtained for vacuum-deposited 2D perovskites. Through the series of experiments carried out to deposit pure and mixed halide PEA_2PbX_4 perovskite films (with $\text{X} = \text{I}^-$, Br^- , or a combination of both), an halide cross-contamination between different deposition runs was found. In particular, we observed a low bromide content in $(\text{PEA})_2\text{PbI}_4$ and a large iodide contamination in $(\text{PEA})_2\text{PbBr}_4$ films, suggesting that the use of a dedicated chamber might be necessary for the fabrication of wide bandgap (bromide) perovskites. Moreover, in the preparation of mixed I/Br 2D perovskites, a strong dependence of the material quality with the chemical nature of the halide precursors was observed. This is another important guideline that has to be considered for the vacuum processing of low-dimensional, mixed halide perovskites. Recently, low dimensional perovskites are being extensively studied as interlayers to enhance the open-circuit voltage and the stability of solar cells, using 2D/3D perovskite bilayers. In Chapter 4, the fabrication of 2D/3D heterostructures by dual-source vacuum deposition of the 2D $(\text{PEA})_2\text{PbI}_4$ and 3D

MAPI films is described for the first time. The advantages of vacuum-deposition, such as the exclusion of issues associated with the use of solvents (leading to intermixing between the 2D and 3D phases) and the precise control over the film thickness, allowed to study three different heterostructures (2D/3D/2D, 2D/3D, 3D/2D) with varying thickness of the 2D layers (2, 5 and 10 nm). When using these perovskite heterostructures in solar cells, a trade-off between the V_{oc} and FF was identified. This behaviour is related to the preferential in-plane orientation of the 2D film, a low carrier mobility, and a mismatch in the transport energy levels between the 2D and the 3D perovskites. A photovoltage as high as 1.1 V was obtained for a 3D/2D heterojunction solar cell, which could be further improved by promoting charge transport, either by controlling the 2D perovskite orientation, or by using low dimensional perovskites with higher n values.

Chapter 6

Spanish summary / Resumen en Castellano

6.1 Capítulo 1

Introducción de la tesis

6.1.1 Visión general

La producción de energía depende en gran medida de los combustibles fósiles como el petróleo, el gas natural y el carbón, que son económicamente convenientes, pero presentan reservas finitas y producen dióxido de carbono (CO₂) y otros gases de efecto invernadero como productos de la combustión. Para una reducción de las emisiones de CO₂ y para detener el calentamiento global, la energía debe ser generada y utilizada de manera más limpia, produciendo menos emisiones. El empleo de fuentes de energía renovables es la solución más prometedora para lograr estos objetivos. La energía solar es la más

abundante entre las fuentes renovables y la tecnología fotovoltaica (PV), conversión directa de la luz solar en electricidad, se está volviendo más competitiva económicamente. Hoy en día, la tecnología fotovoltaica está dominada por las células solares de silicio. La sílice (óxido de silicio, SiO_2) es un material abundante y no tóxico, pero requiere un consumo de energía sustancial para su conversión en silicio cristalino de alta pureza, lo que aumenta el tiempo de retorno energético de la célula solar (el tiempo que una fuente de energía necesita estar funcionando para generar la cantidad de energía utilizada para su producción). Además, las células solares de silicio están alcanzando su límite teórico de eficiencia. Para mejorar la relación eficiencia/coste de los paneles solares, se están investigando materiales alternativos que son abundantes, de simple preparación, y con una eficiencia similar a la del silicio. Entre estos materiales se encuentran las perovskitas híbridas orgánicas-inorgánicas. Las células solares de perovskita pueden ser fabricadas a través de métodos simples, que son compatibles con fabricación a gran escala y con sustratos flexibles. A diferencia del silicio, la perovskita es un semiconductor de banda directa con un coeficiente de absorción muy alto, lo que permite una absorción cuantitativa de la luz en películas tan finas como 500 nm. Esta característica permitiría la fabricación de células solares mucho más ligeras comparadas con las de silicio. Otro aspecto que hace únicas a las perovskitas es la posibilidad de alterar sus propiedades optoelectrónicas mediante simples variaciones de su composición. Gracias a sus buenas propiedades optoelectrónicas, las perovskitas tienen una serie de aplicaciones distintas más allá de la fotovoltaica, por ejemplo en fotodetectores, memresistores, detectores de rayos X, diodos emisores de luz (LEDs), etc. Entre ellas, los LEDs son una aplicación particularmente atractiva debido a las versátiles y modificables propiedades optoelectrónicas de las perovskitas.

6.1.2 Perovskitas híbridas

El nombre perovskita, derivado del mineralogista ruso Lev Perovski, es usado para nombrar todos los compuestos que presentan estructura cristalina tridimensional de fórmula general ABX_3 . Una subclase específica de esta familia son las perovskitas híbridas, en las cuales el catión A es orgánico, M es un metal divalente con coordinación octaédrica (Pb^{2+}) y X es un haluro. La estructura de las perovskitas híbridas de plomo consiste en un retículo de octaedros de haluro de plomo (PbX_6) unidos por los vértices, intercalados con los cationes orgánicos (**Figura 1.5**). La estructura cristalina de las perovskitas híbridas puede presentar diferente dimensionalidad, que se utiliza para clasificar las perovskitas en tridimensionales (3D) y en las de más baja dimensionalidad, las bidimensionales (2D) y las cuasi-2D. La formación de estas estructuras depende en gran medida del tamaño del catión A. Si el catión A es suficientemente pequeño para caber en la cavidad determinada por cuatro octaedros plomo-halógeno, se forman estructuras 3D. Los cationes más comunes son los cationes orgánicos monovalentes como el metilamonio (MA: $CH_3NH_3^+$), el formamidinio (FA: $CH_2(NH_2)_2^+$) y, en el caso de perovskitas completamente inorgánicas, el cesio (Cs^+). Si el catión orgánico es más grande, la estructura tridimensional no puede acomodarlos y se formará una estructura bidimensional, donde láminas de octaedros de haluro de plomo se alternan con capas de moléculas orgánicas. La perovskita 2D presenta la fórmula general $(R-NH_3)_2PbX_4$ (**Figura 1.7**). La familia de las perovskitas de baja dimensionalidad no se limitan solo a esta estructura, ya que pueden prepararse estructuras intermedias con láminas inorgánicas de diversos espesores utilizando una mezcla de cationes pequeños (A) y cationes orgánicos grandes ($R-NH_3$). Estos materiales se denominan perovskitas Ruddlesden-Popper o cuasi-2D, con fórmula $(RNH_3)_2(A)_{n-1}Pb_nX_{3n+1}$ donde n indica el número de láminas inorgánicas (**Figura 1.8**).

El espesor de las capas inorgánicas (n) puede modularse cambiando la proporción de cationes pequeños y grandes.

6.1.3 Propiedades de las perovskitas híbridas

Las perovskita híbridas son semiconductores con un bandgap directo con bandas de energía que pueden simplificarse como se muestra en la **Figura 1.9**. La banda de valencia (VB) es la banda de energía llena formada por los electrones de valencia, mientras que la banda de conducción (CB) es la banda de energía vacía en la que los electrones pueden moverse libremente dentro del material. En un semiconductor intrínseco las dos bandas están separadas por una banda prohibida (E_g , en inglés, *bandgap*), sin estados electrónicos. Sólo pueden ser absorbidos fotones con una energía igual o superior a E_g . La absorción de un fotón conlleva la excitación de un electrón desde la VB a la CB, dejando una carga positiva (hueco) en la banda de valencia.

En una perovskita híbrida de haluro metálico, la VB está formada por una mezcla de orbitales s del metal y orbitales p del haluro, mientras que la CB está compuesta principalmente por orbitales p metálicos. Aumentando la electronegatividad del haluro (sustituyendo I con Br y Cl) baja la energía del orbital p del haluro, disminuyendo la energía de la VB. Además, la energía de la CB, influenciada por los orbitales p de metal Pb, se desplaza hacia arriba cuando las distancias Pb-X disminuyen al pasar de I a Br a Cl. Como consecuencia, al intercambiar o mezclar haluros con diferente electronegatividad es posible modular el bandgap, ampliando el abanico de posibles aplicaciones de las perovskitas. Asimismo, al pasar de I a Br y Cl, el carácter iónico más fuerte del enlace Pb-X conduce a un aumento de la energía de enlace del excitón (E_b). En la perovskita 2D los excitones poseen una energía de enlace del orden de cientos de meV, al menos un orden de magnitud mayor que la energía de enlace de los

excitones de las perovskitas 3D (decenas de meV). La alta E_b de las perovskitas 2D se refleja en la intensa transición excitónica característica que domina su perfil de absorción óptica. Este comportamiento de la perovskita 2D es una consecuencia de sus estructuras de múltiples pozos cuánticos donde las capas inorgánicas actúan como semiconductores y las capas orgánicas como barreras aislantes (**Figura 1.14**). Por esta razón, los electrones y huecos fotogenerados forman excitones que son confinados en las capas de halogenuros metálicos, lo que aumenta su energía de enlace. Las películas delgadas de las perovskitas 2D muestran picos intensos (001) en sus patrones de difracción, sugiriendo que se orientan a lo largo del eje c , con las capas inorgánicas de PbX_6 alternadas con bicapas orgánicas paralelas al plano del sustrato. Esto implica que las láminas aislantes de cationes orgánicos están orientadas perpendicularmente a la dirección del campo eléctrico, obstaculizando el transporte de la carga. Al mismo tiempo, la elevada E_b limita la conversión de los excitones en portadores de carga libres, reduciendo la movilidad de carga. Una forma de cambiar la orientación cristalográfica desfavorable y favorecer el transporte de la carga es mediante el uso de fases cuasi-2D en lugar de las perovskitas 2D puras.

6.1.4 Recombinación

La eficiencia de las células solares y los diodos emisores de luz está limitada por varios procesos de pérdida, entre los cuales está la recombinación de la carga. La recombinación de electrones y huecos en un semiconductor tiene lugar a través de diferentes mecanismos (**Figura 1.10**).

Recombinación radiativa

La recombinación radiativa es el proceso en el que un electrón de la banda de conducción relaja a la banda de valencia y recombina con un hueco, liberando energía en forma de un fotón. Este es el mecanismo de recombinación más importante para los LEDs, pero también es inevitable en una célula solar.

Recombinación no radiativa (Shockley-Read-Hall)

En este mecanismo de recombinación, un electrón o un hueco es capturado por estados electrónicos situados dentro de la banda prohibida (denominados trampas electrónicas), que suelen ser causados por impurezas y defectos en la red cristalina del semiconductor. Por lo tanto, este mecanismo de recombinación también se conoce como recombinación asistida por trampas. Una vez el estado de trampa está ocupado, puede haber recombinación con un portador de carga opuesta, siendo la recombinación no radiativa (sin emisión de fotones). Es importante reducir al mínimo las trampas, y en consecuencia, las pérdidas por recombinación no radiativa que son perjudiciales para la electroluminiscencia en los LED y para la eficiencia en las células solares basadas en perovskitas.

6.1.5 Principio de funcionamiento de las células solares

En una célula solar el material fotoactivo absorbe la luz generando pares de electrones y huecos, que son extraídos hacia los electrodos por materiales transportadores de carga de tipo n y p , respectivamente. Para evaluar el funcionamiento de las células solares se identifican unos parámetros característicos:

- Corriente de cortocircuito, J_{sc} (mA cm⁻²), representa la corriente generada a circuitos cerrado (0 voltios), depende de la cantidad de fotones absorbidos, de la eficiencia de separación de carga, y de la eficiencia de extracción.

- Voltaje a circuito abierto, V_{oc} (V), es el máximo voltaje generado por una célula solar en circuito abierto cuando la corriente es nula.

- Factor de llenado (en inglés, fill factor), FF (%), se define como la relación entre el punto de máxima potencia dividido entre el producto de V_{oc} y J_{sc} . Gráficamente representa la “cuadratura” de la curva de densidad de corriente en función del voltaje (**Fig. 1.22**).

- Eficiencia de conversión energética, PCE (%), expresada como el cociente del punto de máxima potencia de la célula solar y la potencia lumínica irradiada sobre el dispositivo.

- Eficiencia cuántica externa, EQE (%), representa la relación entre el número de electrones extraídos en los contactos y el número de fotones incidentes sobre el dispositivo.

6.1.6 Principio de funcionamiento de diodos emisores de luz

Los LEDs son dispositivos multicapas donde una lámina de material luminiscente está interpuesta entre capas de otros semiconductores que transportan selectivamente electrones y huecos, confinándolos en el material activo donde recombinan radiativamente (**Figura 1.25**). El mecanismo de funcionamiento de los LEDs de perovskita puede aproximarse al de una heterounión p-i-n. En general, pueden identificarse tres regímenes de

funcionamiento en la curva característica de corriente-voltaje (J-V): corriente de fuga (1), corriente de difusión (2) y régimen de corriente de deriva (3) (**Figura 1.24**). Para cuantificar el rendimiento de un LED se utilizan los siguientes parámetros:

- Luminancia (cd m^{-2}), representa la intensidad de luz emitida en candelas por unidad de superficie del dispositivo.
- Densidad de corriente (A m^{-2}), corresponde a la intensidad de corriente por unidad de superficie del dispositivo.
- Eficiencia de corriente (cd A^{-1}), representa la intensidad de luz emitida por densidad de corriente inyectada en el dispositivo.
- Eficiencia de potencia (lm W^{-1}), expresa la eficiencia, pero teniendo en cuenta también el voltaje aplicado al diodo.
- Eficiencia cuántica externa EQE (%), representa el número de fotones emitidos por electrones inyectados.

6.1.7 Técnicas de deposición de capa fina de perovskita

Las propiedades químicas de las perovskitas permiten la fabricación de películas delgadas de alta calidad (tanto óptica como electrónica) mediante varios métodos de deposición. Las técnicas de formación de capas de perovskitas se pueden dividir en dos clases: técnicas de deposición por disolución y técnicas de deposición en alto vacío.

Métodos de disolución:

- Deposición en un sólo paso por rotación (**Fig. 1.27**)
- Deposición con lavado con antidisolvente (**Fig. 1.28**)
- Deposición en un sólo paso con secado de gas (**Fig. 1.29**)
- Deposición secuencial por rotación (**Fig. 1.30**)
- Deposición secuencial por baño (**Fig. 1.30**)

Métodos de alto vacío

- Co-evaporación (**Fig. 1.31a**)
- Evaporación flash (**Fig. 1.32**)
- Evaporación secuencial (**Fig. 1.31b**)

En esta tesis, los principales métodos de deposición empleados han sido la técnica de disolución con antisolvente y la co-evaporación en alto vacío. En la técnica de *deposición con antidisolvente*, durante la rotación del sustrato, mientras la disolución se extiende sobre el mismo y tiene lugar la formación de la capa de perovskita, se vierte un disolvente de polaridad opuesta sobre dicha capa. El antidisolvente acelera la supersaturación de la disolución de los precursores mediante la rápida eliminación del disolvente polar. De esta manera se altera la cinética de cristalización permitiendo la formación de películas compactas y homogéneas. Este método requiere el control de varios parámetros de procesado diferentes y por eso es difícil de controlar.

En la técnica de *co-evaporación en alto vacío*, el catión orgánico y el haluro metálico, colocados en crisoles cerámicos térmicamente controlados, se evaporan simultáneamente a sus correspondientes temperaturas de sublimación en una cámara de alto vacío, donde condensan y reaccionan sobre un sustrato colocado sobre las fuentes. La estequiometría del material puede ajustarse con

precisión mediante el control de las velocidades de evaporación de los componentes previamente calibrados. Esta técnica de recubrimiento elimina los problemas asociados con el uso de disolventes y permite la formación de capas de perovskita de alta calidad.

6.2 Capítulo 2

Capas delgadas de perovskita con alto rendimiento cuántico de fotoluminiscencia

6.2.1 Introducción

La recombinación no-radiativa de portadores de carga es un proceso perjudicial que debe reducirse al mínimo en favor de la recombinación radiativa para alcanzar el mejor rendimiento posible en los diodos emisores de luz. La eficiencia cuántica externa de la electroluminiscencia (EQE_{EL}) es proporcional al rendimiento cuántico de fotoluminiscencia (PLQY) de los semiconductores, por lo tanto, aumentar el PLQY de los semiconductores es clave para fabricar dispositivos electroluminiscentes eficientes. Una de las estrategias para aumentar el PLQY es el confinamiento espacial de los portadores de carga, que se puede lograr disminuyendo el tamaño de grano de la perovskita. Las perovskitas de dimensión reducida pueden prepararse mediante varios métodos, ya sea utilizando plantillas o mediante la síntesis directa de nano partículas (NP) de perovskita. Desafortunadamente, la plantilla inhibe la conectividad necesaria para el transporte de carga, mientras que se observa comúnmente una reducción sustancial del PLQY cuando las suspensiones de NPs se procesan en película delgada. Las perovskitas de baja dimensionalidad Ruddlesden-Popper (cuasi-2D) ofrecen también un medio para mejorar el PLQY. En este capítulo se

estudian las perovskitas de bromuro de plomo cuasi-2D, empleando el metilamonio (MA) y el butilamonio (BA) como cationes pequeños y grandes, respectivamente, con el objetivo de aumentar el PLQY. Se utilizó la perovskita de $(\text{BA})_2(\text{MA})_{n-1}\text{Pb}_n\text{X}_{3n+1}$ con $n = 5$ y se varió la relación entre BA y MA mientras que la concentración de PbBr_2 se mantuvo constante. En la perovskita cuasi-2D con $n = 5$, la relación molar BA:MA es de 2:4, y para estudiar la influencia de la concentración de los cationes de cadena larga en el crecimiento y propiedades del material, también se investigaron relaciones molares más altas (BA:MA = 3:3 y 4:2).

6.2.2 Metodología y Discusión

Las capas de perovskita cuasi-2D con relación molar BA:MA 2:4, 3:3 y 4:2, han sido fabricadas mediante la deposición desde disolución por spin-coating sobre sustratos de vidrio. En los espectros de absorción óptica de todos los compuestos (**Figura 2.1b**) se pueden identificar varios picos de absorción diferentes, como se espera para las perovskitas cuasi-2D. Las perovskitas de Ruddlesden-Popper, en este caso, presentan una distribución de n , es decir, una distribución de fases con diferentes espesores de las capas inorgánicas. Desafortunadamente, esta serie de películas delgadas exhibió una fotoluminiscencia muy débil a la baja intensidad de excitación utilizada en nuestras medidas. Para mejorar el PLQY, la morfología y el tamaño de los cristales de la perovskita pueden manipularse mediante lavado con antidisolvente durante la deposición de la película delgada. El cloroformo (CHCl_3) se utilizó como antidisolvente debido a su baja polaridad con respecto al disolvente de los precursores de perovskita, el DMSO. Se han ajustado y estudiado varios parámetros para modificar la morfología de la película, en particular la velocidad de rotación, el volumen de antidisolvente y el tiempo de lavado. Como

consecuencia de la deposición con antidisolvente se encontró que los perfiles de absorción óptica de las mismas composiciones de perovskita estaban sustancialmente alterados (**Figura 2.2a**). Además, en este caso, el PLQY correspondiente a la perovskita equimolar 3:3 exhibe un PLQY muy elevado de 35%. Esto es consecuencia del proceso de lavado con antidisolvente, que elimina rápidamente el exceso de DMSO llegando a una rápida cristalización que limita el crecimiento de los granos. La pasivación superficial también es eficaz para reducir los estados de trampa que actúan como centros de recombinación no radiativos. La pasivación puede realizarse mediante la disolución de un dador de electrones en el disolvente utilizado para el lavado y/o mediante tratamientos posteriores a la deposición con diversas bases de Lewis. Aquí elegimos un semiconductor molecular de tipo n, el óxido de 9,9-espirobifluoren-2-il-difenilfosfina óxido (SPPO1), que actúa también como una base de Lewis debido al grupo óxido de fosfina. El proceso de deposición con el aditivo SPPO1 tuvo un fuerte efecto en las propiedades de fotoluminiscencia de la película de perovskita, resultando en un PLQY muy alto, del 80% (**Figura 2.3**). El alto PLQY está relacionado con un tamaño de grano menor, como confirman las medidas de XRD y AFM (**Figura 2.4b** y **2.5**). Las imágenes de AFM evidencian también que el lavado con cloroformo y con SPPO1 reduce drásticamente la rugosidad de la superficie, dando lugar a una muestra más plana y homogénea. El alto PLQY junto con la calidad morfológica de las capas de perovskita cuasi-2D (BA:MA = 3:3) son adecuados para aplicaciones en LEDs y por lo tanto, se integraron en dispositivos multicapa (**Figura 2.8**). La electroluminiscencia de los LEDs alcanzó 1000 cd m^{-2} a 8V, como se muestra en la **Figura 2.9a**. A pesar de la alta luminancia, estos dispositivos mostraron una densidad de corriente relativamente alta, lo que limita la eficiencia a 1.3 cd A^{-1} (**Figura 2.9b**). Este fenómeno podría ser consecuencia de la solubilidad del PEDOT:PSS en el disolvente DMSO utilizado para el procesado de la perovskita. Para mejorar la

estabilidad del PEDOT:PSS, añadimos a sus suspensiones una pequeña cantidad (1 v/v%) de 3-glucidoxipropiltrimetoxisilano (GOPS) como agente reticulante. Como resultado de la modificación de la capa de PEDOT:PSS, la corriente de fuga de los LEDs se reduce sustancialmente, lo que lleva a una reducción del voltaje de encendido (2.8 V), y a una eficiencia de corriente máxima de 3.3 cd A⁻¹ a 5 V (**Figura 2.9a, b**).

6.2.3 Conclusión

En el presente capítulo se ha estudiado la preparación de películas delgadas de perovskita cuasi-2D con alto PLQY. La elaboración de un protocolo de ingeniería de materiales incluyó la modificación de la deposición de la solución de la perovskita con lavado de antidisolvente y la variación de la relación molar entre los cationes orgánicos pequeños (BA) y grandes (MA). Se obtuvo un PLQY del 35% para las películas de perovskita cuasi-2D con una relación BA:MA 3:3. Se logró una mejora adicional del PLQY hasta el 80% con la adición de un semiconductor orgánico con propiedades dadoras de electrones en el antidisolvente, reduciendo los canales de recombinación no radiativos. Se han integrado películas delgadas de estos materiales en LEDs multicapa, que mostraron una baja corriente de fuga y un bajo voltaje de encendido, una alta luminiscencia de 1000 cd m⁻² y una eficiencia máxima de corriente de 3.3 cd A⁻¹.

6.3 Capítulo 3

Deposición en alto vacío de capas delgadas de perovskita de baja dimensionalidad

6.3.1 Introducción

En el capítulo 2 se describió un método fiable para preparar películas delgadas de alta calidad de perovskita cuasi-2D. Sin embargo, el método de lavado con antisolvente requiere el control de muchos parámetros, lo que compromete la reproducibilidad del procesado de la perovskita. Para superar esta limitación, se ha investigado la deposición en alto vacío de las perovskitas cuasi-2D y de las perovskitas 2D puras. Sólo existe un trabajo sobre perovskitas 2D completamente co-evaporadas, y data de 1997. En este trabajo, sin embargo, el perfil de difracción de rayos X sugiere que la película depositada al vacío era defectuosa y desordenada. En este capítulo se presenta la co-deposición en alto vacío de diferentes capas de perovskitas cuasi-2D, así como de perovskitas 2D puras y de haluro mixto. También se investigan sus propiedades estructurales, ópticas y de transporte de carga.

6.3.2 Metodología y Discusión

Inicialmente se eligió la misma perovskita cuasi-2D presentada en el capítulo anterior, $BA_2MA_{n-1}Pb_nBr_{3n+1}$, para su deposición en alto vacío. El proceso implica una co-deposición a partir de tres fuentes: bromuro de butilamonio (BABr), bromuro de metilamonio (MABr) y bromuro de plomo ($PbBr_2$). El espectro de absorción del compuesto obtenido sigue la misma tendencia observada para las perovskitas de Ruddlesen-Popper procesadas por disolución que se presentó en el capítulo anterior. Las películas depositadas al

vacío eran transparentes y uniformes con un color amarillento, como se muestra en la **Figura 3.4**. Las imágenes de microscopía electrónica SEM de la **Figura 3.6** muestran una película homogénea y compacta. Desafortunadamente, los datos de difracción de la **Figura 3.5**, sugieren una baja pureza de fase para este compuesto. Además, la co-deposición en el vacío de las perovskitas cuasi-2D no parece ser muy reproducible. De hecho, durante la deposición, la presión en el interior de la cámara (normalmente estable a 10^{-6} mbar) aumenta a más de 10^{-5} mbar, limitando el control del proceso de evaporación. Además del BABr, también se ha estudiado la sublimación en vacío de otras sales orgánicas, pero sólo la sublimación de los haluros de fenetilamonio demostró ser razonablemente estable, por lo que se investigaron más a fondo el PEAI y el PEABr para la deposición en vacío de las más simples perovskitas 2D. El fenetilamonio plomo yoduro $(\text{PEA})_2\text{PbI}_4$ y el fenetilamonio plomo bromuro $(\text{PEA})_2\text{PbBr}_4$ se depositaron por sublimación de los correspondientes haluros metálicos y sales orgánicas de amonio, el yoduro de fenetilamonio (PEAI) y el yoduro de plomo (PbI_2) en el primer caso, y el bromuro de fenetilamonio (PEABr) y el bromuro de plomo (PbBr_2) en el segundo caso. Las películas de halogenuros mixtos de perovskitas 2D $(\text{PEA})_2\text{PbBr}_2\text{I}_2$ se denominan en este capítulo como $(\text{PEABr})_2\text{PbI}_2$ cuando se depositan por co-sublimación de PEABr y PbI_2 , y como $(\text{PEAI})_2\text{PbBr}_2$ en el caso de co-evaporación de PEAI y PbBr_2 . Las propiedades estructurales de las películas finas sublimadas de perovskita 2D fueron estudiadas por difracción de rayos X. La **Figura 3.8** muestra picos de difracción intensos, indicando una perovskita bien cristalizada. Las señales correspondientes al eje c dominan la difracción, con seis picos [00l]. Esta orientación preferencial indica que la película de perovskita 2D crece con las capas orgánicas e inorgánicas bidimensionales paralelas al plano del sustrato. Tal orientación es común para la perovskita 2D, pero no es favorable para el transporte de carga dentro de un dispositivo de capa delgada. La morfología de

las capas de perovskita 2D se estudió mediante microscopía electrónica de barrido (SEM) y microscopía de fuerza atómica (AFM), que se muestran en las **Figuras 3.11** y **3.12**, respectivamente. Las películas están formadas por plaquetas bien definidas, orientadas al azar y formadas por múltiples granos con un tamaño que va de 200 a 400 nm. Las diferentes perovskitas 2D se distinguen por la diversa rugosidad, como se puede ver en la **Tabla 3.2**. La absorción óptica de las películas $(\text{PEA})_2\text{PbI}_4$ muestra una banda en el UV y un pico excitónico intenso, típico de la perovskita 2D, centrado a 503 nm. Cuando la película de $(\text{PEA})_2\text{PbI}_4$ fue excitada con un LED a 340 nm, se observó una intensa fotoluminiscencia centrada a 521 nm, como muestra la **Figura 3.13a**. La película $(\text{PEA})_2\text{PbBr}_4$ exhibe la banda de absorción óptica esperada a mayor energía, en comparación con el compuesto de yoduro análogo, con un pico excitónico centrado en 403 nm. Se detectó otra banda de absorción más débil a 434 nm, que no puede atribuirse al $(\text{PEA})_2\text{PbBr}_4$. Se observó una fotoluminiscencia intensa y estrecha centrada en 410 nm y otros dos picos adicionales a 434 y 507 nm (**Figura 3.13b**). Lo más probable es que los picos adicionales puedan asociarse a la presencia de una fase más rica en bromuro y una fase más rica en yodo. Estas consideraciones apuntan a una posible contaminación cruzada de haluros en la cámara de evaporación, y el análisis de fluorescencia de rayos X por energía dispersiva verificó esta hipótesis. La contaminación puede deberse a i) la evaporación de materiales previamente depositados en la superficie de la cámara o incluso a ii) el intercambio de haluros entre los vapores de los compuestos y la propia cámara. Estos procesos pueden ser más o menos pronunciados dependiendo de la volatilidad de los materiales, así como de su reactividad química, y plantea un reto que debe tenerse en cuenta en la deposición en vacío de las perovskitas. La absorción óptica de la perovskita de haluro mixto $(\text{PEABr})_2\text{PbI}_2$ (**Figura 3.13c**) presenta un pico excitónico a 446 nm, mientras que el pico de PL es asimétrico con un máximo de 464 nm. En esta proporción

de haluros, las perovskitas 3D suelen mostrar efectos de segregación de haluros, debido a la escasa miscibilidad de las fases de yoduro y bromuro. Por esta razón, estudiamos la evolución del PL a lo largo del tiempo bajo una irradiación láser continua a 375 nm, que confirmó una parcial segregación de haluros. Las propiedades ópticas de las películas de perovskita de haluro mixto $(\text{PEAI})_2\text{PbBr}_2$ son consistentes con la presencia de una fase rica en bromuro, y de una segunda fase rica en yodo (**Figura 3.13d**).

6.3.3 Conclusión

En este capítulo se ha estudiado la deposición en alto vacío y la caracterización de las perovskitas de tipo Ruddlesden-Popper, así como de las perovskitas 2D de haluros puros y mixtos. Las capas de perovskita 2D de tipo PEA_2PbX_4 , donde X es I⁻, Br⁻, o una combinación de ambas, mostraron la tendencia esperada en el bandgap, aumentando desde los materiales de yoduro puro a los de bromuro puro, y con un bandgap intermedio para los compuestos de haluros mixtos. A través de la serie de experimentos realizados, se encontró una inevitable contaminación de haluros entre las diferentes deposiciones, cuya implicación es particularmente relevante para la fabricación de películas de perovskita de ancho de banda amplio como la $(\text{PEA})_2\text{PbBr}_4$, donde la presencia de yoduro da lugar inevitablemente a múltiples picos de luminiscencia. Por lo tanto, se recomienda utilizar una cámara dedicada para cada composición de perovskitas, a fin de asegurar la formación de compuestos de alta pureza.

6.4 Capítulo 4

Heterouniones de perovskita 2D/3D depositadas en alto vacío

6.4.1 Introducción

Las excelentes propiedades de las perovskitas híbridas, como su alto coeficiente de absorción, el transporte de carga ambipolar y la fácil modulación del bandgap, explican el rápido desarrollo de las células solares, que han alcanzado una eficiencia de conversión de energía (PCE) del 25% en sólo 10 años. A pesar de estos logros, la eficiencia aún está lejos del límite de Shockley-Queisser de 30% para un semiconductor con un bandgap de 1.6 eV. Para mejorar aún más la PCE, muchas investigaciones se centran en el aumento del voltaje de circuito abierto (V_{oc}) mediante la reducción de las pérdidas de recombinación no-radiativa, relacionadas con defectos en la superficie y en los bordes de grano de la perovskita. La pasivación de los estados electrónicos asociados a estos defectos puede llevarse a cabo mediante diferentes métodos, entre los que destaca el uso de perovskitas de bandgap ancho y baja dimensionalidad en combinación con perovskitas 3D. Hasta ahora, las capas delgadas de perovskitas 2D se han depositado en la superficie y/o bordes de grano de las perovskitas 3D únicamente mediante procesamiento desde solución, dando lugar a una inevitable mezcla entre las dos fases. En este capítulo se estudia la fabricación de heterouniones de perovskita 2D/3D por deposición en alto vacío. Se estudia la interacción entre las fases 3D (MAPI) y las 2D (PEA_2PbI_4) en tres heteroestructuras de perovskita diferentes: i) 2D/MAPI/2D, ii) 2D/MAPI, iii) MAPI/2D. Todas estas estructuras han sido integradas en células solares depositadas en vacío con el fin de racionalizar el rol de cada interfaz.

6.4.2 Metodología y Discusión

Para investigar la influencia de las capas de perovskita 2D en la morfología y la cristalinidad de la perovskita 3D, se depositaron películas de PEA_2PbI_4 de 10 nm por debajo y por encima de una película de MAPI de 500 nm. Los resultados de la difracción de rayos X en la **Figura 4.2** indican un cambio en la orientación de la película de MAPI cuando se deposita entre capas de perovskita 2D. Además, la superficie de la perovskita 3D depositada entre las capas 2D muestra una reducción del tamaño de cristal y una superficie más compacta y lisa en comparación con la película MAPI de referencia (**Figura 4.6**). Posteriormente, las películas de PEA_2PbI_4 se depositaron entre las interfaces HTL/MAPI, MAPI/ETL o ambas HTL/MAPI/ETL de las células solares en la configuración que se muestra en la **Figura 4.7a**. El grosor del MAPI se mantuvo constante (500 nm) mientras que el grosor del PEA_2PbI_4 varió entre 2,5 nm y 10 nm. Las prestaciones de los dispositivos (**Figura 4.7**) muestran que la extracción de carga de todas las células solares con heterounión 2D/3D resulta obstaculizada y por eso la densidad de corriente disminuye con el aumento del grosor de las capas de perovskitas 2D. Esto concuerda con la formación de perovskitas bidimensionales PEA_2PbI_4 orientadas con las láminas orgánicas aislantes perpendiculares al flujo de corriente. Sin embargo, se observó que el V_{oc} aumentaba en los dispositivos que emplean películas de PEA_2PbI_4 de 5 y 10 nm, lo que implica que las películas 2D son capaces de reducir la recombinación no-radiativa de la capa de MAPI. Por un lado, la incorporación de perovskitas 2D en la interfaz con el MAPI es beneficiosa para el V_{oc} , sin embargo, esta también conduce a una disminución del FF, que se hace más relevante una vez que el grosor de PEA_2PbI_4 aumenta desde 2.5 nm hasta 5 y 10 nm. En el caso de la heterounión MAPI/2D, se observó que el FF disminuía al aumentar el grosor de PEA_2PbI_4 , pero no tan drásticamente como en el caso de las estructuras 2D/MAPI y 2D/MAPI/2D. Además, con esta configuración de dispositivo

MAPI/2D, se observó un aumento sustancial del fotovoltaje, con un V_{oc} superior a 1.1 V para las capas de PEA_2PbI_4 de 5 nm de espesor (**Figura 4.8**). Además de la orientación de la perovskita 2D con respecto al sustrato, otro factor que puede contribuir a la pérdida en FF, es la presencia de una barrera energética para la extracción de la carga (ya sea un hueco o un electrón, o ambos) en la heterounión 3D/2D o en las interfaces perovskita/semiconductor orgánico. Dicha barrera energética está relacionada con la desalineación de los niveles de energía, que es probable que exista al menos en un caso (ya sea 2D/3D o 3D/2D) como consecuencia de que el bandgap de PEA_2PbI_4 es más grande que el de MAPI (**Figura 4.9**).

6.4.3 Conclusiones

En este capítulo, las películas 2D (PEA_2PbI_4) preparadas por deposición en vacío de dos fuentes, se utilizaron por primera vez para la fabricación de heteroestructuras de perovskita procesadas totalmente en vacío. Las capas de PEA_2PbI_4 se depositaron debajo y encima del MAPI, también preparado por co-deposición en vacío. Se investigaron la morfología, la estructura y las propiedades ópticas de las heteroestructuras 3D de referencia y de las 2D/3D/2D. Las películas PEA_2PbI_4 depositadas en vacío tienden a crecer con las láminas inorgánicas y orgánicas paralelas al sustrato y, por lo tanto, cuando se incorporan a los dispositivos, obstaculizan la extracción de carga. Este efecto es el resultado de la interacción de diferentes parámetros, como la orientación preferencial en el plano de la película 2D, la baja movilidad de los portadores de carga y la desalineación de los niveles de energía entre las capas. Estudiando por separado las bicapas 2D/3D y 3D/2D, identificamos un balance entre la V_{oc} y FF de la célula solar. Las células solares de heterounión 3D/2D son la que alcanzan el mejor voltaje de circuito abierto de 1.1 V.



Bibliography

1. International Energy agency. Global Energy - CO2 Status Report 2018 – Analysis - IEA. Available at: <https://www.iea.org/reports/global-energy-co2-status-report-2018>. (Accessed: 9th December 2019)
2. Climate change - Business Insider.
3. Horowitz, C. A. Paris Agreement. *Int. Leg. Mater.* **55**, 740–755 (2016).
4. Perez, R. & Perez, M. A Fundamental Look At Supply Side Energy Reserves For The Planet. *Int. Energy Agency SHC Program. Sol. Updat.* **62**, 4–6 (2015).
5. Bleich, K. & Guimaraes, R. D. Renewable Infrastructure Investment Handbook: A Guide for Institutional Investors. *World Econ. Forum Ind. Agenda* 43 (2016).
6. Tiwari, G. N. & Mishra, R. K. (Rajeev K. *Advanced renewable energy sources*. (RSC Publishing, 2012).
7. Yoshikawa, K. *et al.* Silicon heterojunction solar cell with interdigitated back contacts for a photoconversion efficiency over 26%. *Nat. Energy* **2**, (2017).
8. Kayes, B. M. *et al.* 27.6% Conversion efficiency, a new record for single-junction solar cells under 1 sun illumination. in *2011 37th IEEE Photovoltaic Specialists Conference* 000004–000008 (IEEE, 2011). doi:10.1109/PVSC.2011.6185831
9. First Solar Hits Record 22.1% Conversion Efficiency for CdTe Solar Cell | Greentech Media. Available at: <https://www.greentechmedia.com/articles/read/first-solar-hits-record-22-1-conversion-efficiency-for-cdte-solar-cell>. (Accessed: 29th October 2019)
10. De Wild-Scholten, M. J. Energy payback time and carbon footprint of commercial photovoltaic systems. *Sol. Energy Mater. Sol. Cells* **119**, 296–305 (2013).
11. Green, M. A. *et al.* Solar cell efficiency tables (Version 53). *Prog. Photovoltaics Res. Appl.* **27**, 3–12 (2019).

12. Chuang, C.-H. M., Brown, P. R., Bulović, V. & Bawendi, M. G. Improved performance and stability in quantum dot solar cells through band alignment engineering. *Nat. Mater.* **13**, 796–801 (2014).
13. Meng, L. *et al.* Organic and solution-processed tandem solar cells with 17.3% efficiency. *Science (80-.)*. **361**, 1094–1098 (2018).
14. Lin, Y. *et al.* 17% Efficient Organic Solar Cells Based on Liquid Exfoliated WS₂ as a Replacement for PEDOT:PSS. *Adv. Mater.* **31**, (2019).
15. O'Regan, B. & Grätzel, M. A low-cost, high-efficiency solar cell based on dye-sensitized colloidal TiO₂ films. *Nature* **353**, 737–740 (1991).
16. Gong, J., Liang, J. & Sumathy, K. Review on dye-sensitized solar cells (DSSCs): Fundamental concepts and novel materials. *Renew. Sustain. Energy Rev.* **16**, 5848–5860 (2012).
17. Green, M. A., Ho-Baillie, A. & Snaith, H. J. The emergence of perovskite solar cells. *Nat. Photonics* **8**, 506–514 (2014).
18. Kojima, A., Teshima, K., Shirai, Y. & Miyasaka, T. Organometal Halide Perovskites as Visible-Light Sensitizers for Photovoltaic Cells. *J. Am. Chem. Soc.* **131**, 6050–6051 (2009).
19. Best Research-Cell Efficiency Chart | Photovoltaic Research | NREL. Available at: <https://www.nrel.gov/pv/cell-efficiency.html>. (Accessed: 9th December 2019)
20. Waide, P. & Tanishima, S. Light ' S Labour ' S Lost. *Int. Energy Agency Policies f*, (2006).
21. Tan, Z.-K. *et al.* Bright light-emitting diodes based on organometal halide perovskite. *Nat. Nanotechnol.* **9**, 687–692 (2014).
22. Lin, K. *et al.* Perovskite light-emitting diodes with external quantum efficiency exceeding 20 per cent. *Nature* **562**, 245–248 (2018).
23. Cao, Y. *et al.* Perovskite light-emitting diodes based on spontaneously formed submicrometre-scale structures. *Nature* **562**, 249–253 (2018).
24. Xu, W. *et al.* Rational molecular passivation for high-performance perovskite light-emitting diodes. *Nat. Photonics* **13**, 418–424 (2019).
25. Li, C. *et al.* Formability of ABX₃ (X = F, Cl, Br, I) halide perovskites. *Acta Crystallogr. Sect. B Struct. Sci.* **64**, 702–707 (2008).

26. Jiang, L. Q. *et al.* Prediction of lattice constant in cubic perovskites. **67**, 1531–1536 (2006).
27. Fan, Z., Sun, K. & Wang, J. Perovskites for photovoltaics: a combined review of organic-inorganic halide perovskites and ferroelectric oxide perovskites. *J. Mater. Chem. A* **3**, 18809–18828 (2015).
28. Poglitsch, A., Weber, D., Poglitsch, A. & Weber, D. Dynamic disorder in methylammoniumtrihalogenoplumbates (II) observed by millimeter-wave spectroscopy. *J. Chem. Phys.* **87**, 6373–6378 (1987).
29. MØLLER, C. K. Crystal Structure and Photoconductivity of Cæsium Plumbohalides. *Nature* **182**, 1436–1436 (1958).
30. Weber, D. CH₃NH₃PbX₃, ein Pb(II)-System mit kubischer Perowskitstruktur / CH₃NH₃PbX₃, a Pb(II)-System with Cubic Perovskite Structure. *Zeitschrift für Naturforsch. B* **33**, 1443–1445 (1978).
31. de Jongh, L. J. & Miedema, A. R. Experiments on simple magnetic model systems. *Adv. Phys.* **23**, 1–260 (1974).
32. Dolzhenko, Y. I., Inabe, T. & Maruyama, Y. In Situ X-Ray Observation on the Intercalation of Weak Interaction Molecules into Perovskite-Type Layered Crystals (C₉H₁₉NH₃)₂PbI₄ and (C₁₀H₂₁NH₃)₂CdCl₄. *Bulletin of the Chemical Society of Japan* **59**, 563–567 (1986).
33. Mitzi, D. B., Chondroudis, K. & Kagan, C. R. Organic-inorganic electronics. *IBM J. Res. Dev.* **45**, 29–45 (2001).
34. Lemmerer, A. & Billing, D. G. Lead halide inorganic–organic hybrids incorporating diammonium cations. *CrystEngComm* **14**, 1954 (2012).
35. Stoumpos, C. C. *et al.* High Members of the 2D Ruddlesden-Popper Halide Perovskites: Synthesis, Optical Properties, and Solar Cells of (CH₃(CH₂)₃NH₃)₂(CH₃NH₃)₄Pb₅I₁₆. *Chem* **2**, 427–440 (2017).
36. Calabrese, J. *et al.* Preparation and characterization of layered lead halide compounds. *J. Am. Chem. Soc.* **113**, 2328–2330 (1991).
37. Smith, I. C., Hoke, E. T., Solis-Ibarra, D., McGehee, M. D. & Karunadasa, H. I. A Layered Hybrid Perovskite Solar-Cell Absorber with Enhanced Moisture Stability. *Angew. Chemie Int. Ed.* **53**, 11232–11235 (2014).

38. Tao, S. *et al.* Absolute energy level positions in tin- and lead-based halide perovskites. *Nat. Commun.* **10**, 2560 (2019).
39. Hoke, E. T. *et al.* Reversible photo-induced trap formation in mixed-halide hybrid perovskites for photovoltaics. *Chem. Sci.* **6**, 613–617 (2015).
40. Comin, R. *et al.* Structural, optical, and electronic studies of wide-bandgap lead halide perovskites. *J. Mater. Chem. C* **3**, 8839–8843 (2015).
41. Saba, M., Quochi, F., Mura, A. & Bongiovanni, G. Excited State Properties of Hybrid Perovskites. *Acc. Chem. Res.* **49**, 166–173 (2016).
42. Shimizu, M., Fujisawa, J.-I. & Ishi-Hayase, J. Influence of dielectric confinement on excitonic nonlinearity in inorganic-organic layered semiconductors. *Phys. Rev. B* **71**, 205306 (2005).
43. Katan, C., Mercier, N. & Even, J. Quantum and Dielectric Confinement Effects in Lower-Dimensional Hybrid Perovskite Semiconductors. *Chem. Rev.* **119**, 3140–3192 (2019).
44. Ahmad, S., Hanmandlu, C., Kanaujia, P. K. & Prakash, G. V. Direct deposition strategy for highly ordered inorganic organic perovskite thin films and their optoelectronic applications. *Opt. Mater. Express* **4**, 1313 (2014).
45. Pradeesh, K., Rao, K. N. & Prakash, G. V. Synthesis, structural, thermal and optical studies of inorganic-organic hybrid semiconductors, R-PbI₄. *J. Appl. Phys.* **113**, (2013).
46. Shimizu, M., Fujisawa, J.-I. & Ishi-Hayase, J. Influence of dielectric confinement on excitonic nonlinearity in inorganic-organic layered semiconductors. *Phys. Rev. B* **71**, 205306 (2005).
47. Straus, D. B. & Kagan, C. R. Electrons, Excitons, and Phonons in Two-Dimensional Hybrid Perovskites: Connecting Structural, Optical, and Electronic Properties. *J. Phys. Chem. Lett.* **9**, 1434–1447 (2018).
48. Gélvez-Rueda, M. C. *et al.* Interconversion between Free Charges and Bound Excitons in 2D Hybrid Lead Halide Perovskites. *J. Phys. Chem. C* **121**, 26566–26574 (2017).
49. Blancon, J. C. *et al.* Scaling law for excitons in 2D perovskite quantum wells. *Nat. Commun.* **9**, 1–10 (2018).

50. Cao, D. H., Stoumpos, C. C., Farha, O. K., Hupp, J. T. & Kanatzidis, M. G. 2D Homologous Perovskites as Light-Absorbing Materials for Solar Cell Applications. *J. Am. Chem. Soc.* **137**, 7843–7850 (2015).
51. Schmidt-mende, L. & Weickert, J. *Lukas Schmidt-Mende, Jonas Weickert Organic and Hybrid Solar Cells De Gruyter Graduate*.
52. Shockley, W. & Queisser, H. J. Detailed balance limit of efficiency of p-n junction solar cells. *J. Appl. Phys.* **32**, 510–519 (1961).
53. Guillemoles, J. F., Kirchartz, T., Cahen, D. & Rau, U. Guide for the perplexed to the Shockley–Queisser model for solar cells. *Nat. Photonics* **13**, 501–505 (2019).
54. Tsujimura, T. *OLED Display Fundamentals and Applications -Wiley-SID Series in Display Technology*.
55. Burschka, J. *et al.* Sequential deposition as a route to high-performance perovskite-sensitized solar cells. *Nature* **499**, 316–319 (2013).
56. Kerner, R. A., Zhao, L., Xiao, Z. & Rand, B. P. Ultrasoother metal halide perovskite thin films via sol–gel processing. *J. Mater. Chem. A* **4**, 8308–8315 (2016).
57. Zheng, L., Zhang, D., Ma, Y., Lu, Z. & Chen, Z. Morphology control of the perovskite films for efficient solar cells. 10582–10593 (2015). doi:10.1039/c4dt03869j
58. Jeon, N. J. *et al.* Solvent engineering for high-performance inorganic–organic hybrid perovskite solar cells. *Nat. Mater.* **13**, 897–903 (2014).
59. Conings, B. *et al.* Getting rid of anti-solvents: Gas quenching for high performance perovskite solar cells. *2018 IEEE 7th World Conf. Photovolt. Energy Conversion, WCPEC 2018 - A Jt. Conf. 45th IEEE PVSC, 28th PVSEC 34th EU PVSEC* 1724–1729 (2018). doi:10.1109/PVSC.2018.8547987
60. Huang, F. *et al.* Gas-assisted preparation of lead iodide perovskite films consisting of a monolayer of single crystalline grains for high efficiency planar solar cells. *Nano Energy* **10**, 10–18 (2014).
61. Zheng, L. *et al.* Morphology control of the perovskite films for efficient solar cells. *Dalt. Trans.* **44**, 10582–10593 (2015).
62. Chen, Q. *et al.* Planar Heterojunction Perovskite Solar Cells via Vapor-Assisted Solution Process. *J. Am. Chem. Soc.* **136**, 622–625 (2014).

63. Liu, M., Johnston, M. B. & Snaith, H. J. Efficient planar heterojunction perovskite solar cells by vapour deposition. *Nature* **501**, 395–398 (2013).
64. Ávila, J., Momblona, C., Boix, P. P., Sessolo, M. & Bolink, H. J. Vapor-Deposited Perovskites: The Route to High-Performance Solar Cell Production? *Joule* **1**, 431–442 (2017).
65. Dunlap-Shohl, W. A., Zhou, Y., Padture, N. P. & Mitzi, D. B. Synthetic Approaches for Halide Perovskite Thin Films. *Chem. Rev.* **119**, 3193–3295 (2019).
66. Gil-Escrig, L. *et al.* Vacuum Deposited Triple-Cation Mixed-Halide Perovskite Solar Cells. *Adv. Energy Mater.* **8**, 1703506 (2018).
67. La-Placa, M.-G. *et al.* Vacuum-Deposited 2D/3D Perovskite Heterojunctions. *ACS Energy Lett.* 2893–2901 (2019). doi:10.1021/acsenergylett.9b02224
68. Sessolo, M., Momblona, C., Gil-Escrig, L. & Bolink, H. J. Photovoltaic devices employing vacuum-deposited perovskite layers. *MRS Bull.* **40**, 660–666 (2015).
69. Longo, G., Gil-Escrig, L., Degen, M. J., Sessolo, M. & Bolink, H. J. Perovskite solar cells prepared by flash evaporation. *Chem. Commun.* **51**, 7376–7378 (2015).
70. Mitzi, D. B., Prikas, M. T. & Chondroudis, K. Thin Film Deposition of Organic–Inorganic Hybrid Materials Using a Single Source Thermal Ablation Technique. *Chem. Mater.* **11**, 542–544 (1999).
71. Saltsburg, H. Flash Evaporation. *J. Chem. Phys.* **42**, 1303–1309 (1965).
72. Chen, C.-W. *et al.* Efficient and Uniform Planar-Type Perovskite Solar Cells by Simple Sequential Vacuum Deposition. *Adv. Mater.* **26**, 6647–6652 (2014).
73. Deschler, F. *et al.* High photoluminescence efficiency and optically pumped lasing in solution-processed mixed halide perovskite semiconductors. *J. Phys. Chem. Lett.* **5**, 1421–1426 (2014).
74. Cho, H. *et al.* Overcoming the electroluminescence efficiency limitations of perovskite light-emitting diodes. *Science (80-.)*. **350**, 1222–1225 (2015).

75. Zheng, K. *et al.* Exciton Binding Energy and the Nature of Emissive States in Organometal Halide Perovskites. *J. Phys. Chem. Lett.* **6**, 2969–2975 (2015).
76. Di, D. *et al.* Size-Dependent Photon Emission from Organometal Halide Perovskite Nanocrystals Embedded in an Organic Matrix. *J. Phys. Chem. Lett.* **6**, 446–450 (2015).
77. Li, G. *et al.* Efficient Light-Emitting Diodes Based on Nanocrystalline Perovskite in a Dielectric Polymer Matrix. *Nano Lett.* **15**, 2640–2644 (2015).
78. Kojima, A., Ikegami, M., Teshima, K. & Miyasaka, T. Highly Luminescent Lead Bromide Perovskite Nanoparticles Synthesized with Porous Alumina Media. *Chem. Lett.* **41**, 397–399 (2012).
79. Longo, G., Pertegás, A., Martínez-Sarti, L., Sessolo, M. & Bolink, H. J. Highly luminescent perovskite–aluminum oxide composites. *J. Mater. Chem. C* **3**, 11286–11289 (2015).
80. Zhang, F. *et al.* Brightly luminescent and color-tunable colloidal CH₃NH₃PbX₃ (X = Br, I, Cl) quantum dots: Potential alternatives for display technology. *ACS Nano* **9**, 4533–4542 (2015).
81. Schmidt, L. C. *et al.* Non-template Synthesis of CH₃NH₃PbBr₃ Perovskite Nanoparticles Non-template Synthesis of CH₃NH₃PbBr₃ Perovskite Nanoparticles. *J. Am. Chem. Soc.* **136**, 850–853 (2014).
82. Protesescu, L. *et al.* Nanocrystals of Cesium Lead Halide Perovskites (CsPbX₃, X = Cl, Br, and I): Novel Optoelectronic Materials Showing Bright Emission with Wide Color Gamut. *Nano Lett.* **15**, 3692–3696 (2015).
83. Chondroudis, K. & Mitzi, D. B. Electroluminescence from an organic-inorganic perovskite incorporating a quaterthiophene dye within lead halide perovskite layers. *Chem. Mater.* **11**, 3028–3030 (1999).
84. Yuan, M. *et al.* Perovskite energy funnels for efficient light-emitting diodes. *Nat. Nanotechnol.* **11**, 872–877 (2016).
85. Quan, L. N. *et al.* Tailoring the Energy Landscape in Quasi-2D Halide Perovskites Enables Efficient Green-Light Emission. *Nano Lett.* **17**, 3701–3709 (2017).

86. D’Innocenzo, V., Srimath Kandada, A. R., De Bastiani, M., Gandini, M. & Petrozza, A. Tuning the light emission properties by band gap engineering in hybrid lead halide perovskite. *J. Am. Chem. Soc.* **136**, 17730–17733 (2014).
87. Braly, I. L. *et al.* Hybrid perovskite films approaching the radiative limit with over 90% photoluminescence quantum efficiency. *Nat. Photonics* **12**, 355–361 (2018).
88. Yang, X. *et al.* Efficient green light-emitting diodes based on quasi-two-dimensional composition and phase engineered perovskite with surface passivation. *Nat. Commun.* **9**, 2–9 (2018).
89. Dequilettes, D. W. *et al.* Photoluminescence Lifetimes Exceeding 8 μ s and Quantum Yields Exceeding 30% in Hybrid Perovskite Thin Films by Ligand Passivation. *ACS Energy Lett.* **1**, 438–444 (2016).
90. Braly, I. L. *et al.* Hybrid perovskite films approaching the radiative limit with over 90% photoluminescence quantum efficiency. *Nat. Photonics* **12**, 355–361 (2018).
91. Ban, M. *et al.* Solution-processed perovskite light emitting diodes with efficiency exceeding 15% through additive-controlled nanostructure tailoring. *Nat. Commun.* **9**, 1–10 (2018).
92. Xiao, Z. *et al.* Efficient perovskite light-emitting diodes featuring nanometre-sized crystallites. *Nat. Photonics* **11**, 108–115 (2017).
93. Darmawan, N. *et al.* Highly efficient blue and deep-blue emitting zwitterionic iridium(iii) complexes: Synthesis, photophysics and electroluminescence. *J. Mater. Chem. C* **2**, 2569–2582 (2014).
94. Rivnay, J. *et al.* Structural control of mixed ionic and electronic transport in conducting polymers. *Nat. Commun.* **7**, (2016).
95. Chiang, K. M. *et al.* Vacuum-Deposited Organometallic Halide Perovskite Light-Emitting Devices. *ACS Appl. Mater. Interfaces* **9**, 40516–40522 (2017).
96. Zheng, Z., Lan, H., Su, Z., Peng, H. & Luo, J. Single Source Thermal Evaporation of Two-dimensional Perovskite Thin Films for Photovoltaic Applications. *Sci. Rep.* 1–9 (2019). doi:10.1038/s41598-019-53609-0

97. Era, M., Hattori, T., Taira, T. & Tsutsui, T. Self-Organized Growth of PbI₂-Based Layered Perovskite Quantum Well by Dual-Source Vapor Deposition. *Chem. Mater.* **9**, 8–10 (1997).
98. Brunetti, B., Cavallo, C., Ciccio, A., Gigli, G. & Latini, A. On the Thermal and Thermodynamic (In)Stability of Methylammonium Lead Halide Perovskites. *Sci. Rep.* **6**, (2016).
99. Quan, L. N. *et al.* Ligand-Stabilized Reduced-Dimensionality Perovskites. *J. Am. Chem. Soc.* **138**, 2649–2655 (2016).
100. Liang, C. *et al.* Ruddlesden-Popper Perovskite for Stable Solar Cells. *Energy Environ. Mater.* **1**, 221–231 (2018).
101. Stoumpos, C. C. *et al.* Ruddlesden–Popper Hybrid Lead Iodide Perovskite 2D Homologous Semiconductors. *Chem. Mater.* **28**, 2852–2867 (2016).
102. Shallcross, R. C., Olthof, S., Meerholz, K. & Armstrong, N. R. Impact of Titanium Dioxide Surface Defects on the Interfacial Composition and Energetics of Evaporated Perovskite Active Layers. *ACS Appl. Mater. Interfaces* **11**, 32500–32508 (2019).
103. Du, K. *et al.* Two-Dimensional Lead(II) Halide-Based Hybrid Perovskites Templated by Acene Alkylamines: Crystal Structures, Optical Properties, and Piezoelectricity. *Inorg. Chem.* **56**, 9291–9302 (2017).
104. Mitzi, D. B. *Synthesis, structure, and properties of organic-inorganic perovskites and related materials. Progress in Inorganic Chemistry* **48**, (2007).
105. Papavassiliou, G. C., Mousdis, G. A., Raptopoulou, C. P. & Terzis, A. Preparation and Characterization of [C₆H₅CH₂NH₃]₂PbI₄, [C₆H₅CH₂CH₂SC(NH₂)₂]₃PbI₅ and [C₁₀H₇CH₂NH₃]₃PbI₃ Organic-Inorganic Hybrid Compounds. *Zeitschrift für Naturforsch. B* **54**, 1405–1409 (1999).
106. Shibuya, K., Koshimizu, M., Nishikido, F., Saito, H. & Kishimoto, S. Poly[bis(phenethyl-ammonium) [di-bromido-plumbate(II)]-di-μ-bromido]. *Acta Crystallogr. Sect. E. Struct. Rep. Online* **65**, m1323-4 (2009).
107. Mitzi, D. . A Layered Solution Crystal Growth Technique and the Crystal Structure of (C₆H₅C₂H₄NH₃)₂PbCl₄. *J. Solid State Chem.* **145**, 694–704 (1999).

108. Longo, G. *et al.* Fully Vacuum-Processed Wide Band Gap Mixed-Halide Perovskite Solar Cells. *ACS Energy Lett.* **3**, 214–219 (2018).
109. Nagabhushana, G. P., Shivaramaiah, R. & Navrotsky, A. Direct calorimetric verification of thermodynamic instability of lead halide hybrid perovskites. *Proc. Natl. Acad. Sci.* **113**, 7717–7721 (2016).
110. Ivanov, I. L. *et al.* Thermodynamics of formation of hybrid perovskite-type methylammonium lead halides. *J. Chem. Thermodyn.* **116**, 253–258 (2018).
111. Gélvez-Rueda, M. C. *et al.* Interconversion between Free Charges and Bound Excitons in 2D Hybrid Lead Halide Perovskites. *J. Phys. Chem. C* **121**, 26566–26574 (2017).
112. Gao, Y., Zhang, M., Zhang, X. & Lu, G. Decreasing Exciton Binding Energy in Two-Dimensional Halide Perovskites by Lead Vacancies. *J. Phys. Chem. Lett.* **10**, 3820–3827 (2019).
113. Huang, J., Yuan, Y., Shao, Y. & Yan, Y. Understanding the physical properties of hybrid perovskites for photovoltaic applications. *Nature Reviews Materials* **2**, (2017).
114. Brenner, T. M., Egger, D. A., Kronik, L., Hodes, G. & Cahen, D. Hybrid organic - Inorganic perovskites: Low-cost semiconductors with intriguing charge-transport properties. *Nature Reviews Materials* **1**, (2016).
115. Li, W. *et al.* Chemically diverse and multifunctional hybrid organic-inorganic perovskites. *Nature Reviews Materials* **2**, (2017).
116. Green, M. A. *et al.* Solar cell efficiency tables (version 54). *Prog. Photovoltaics Res. Appl.* **27**, 565–575 (2019).
117. Rühle, S. Tabulated values of the Shockley-Queisser limit for single junction solar cells. *Sol. Energy* **130**, 139–147 (2016).
118. Ball, J. M. & Petrozza, A. Defects in perovskite-halides and their effects in solar cells. *Nat. Energy* **1**, 16149 (2016).
119. Qiu, W. *et al.* Pinhole-free perovskite films for efficient solar modules. *Energy Environ. Sci.* **9**, 484–489 (2016).
120. Saliba, M. *et al.* Incorporation of rubidium cations into perovskite solar cells improves photovoltaic performance. *Science (80-.)*. **354**, 206–209 (2016).

121. Liang, P.-W., Chueh, C.-C., Williams, S. T. & Jen, A. K.-Y. Roles of Fullerene-Based Interlayers in Enhancing the Performance of Organometal Perovskite Thin-Film Solar Cells. *Adv. Energy Mater.* **5**, 1402321 (2015).
122. Grancini, G. & Nazeeruddin, M. K. Dimensional tailoring of hybrid perovskites for photovoltaics. *Nat. Rev. Mater.* **4**, 4–22 (2019).
123. Zheng, X. *et al.* Defect passivation in hybrid perovskite solar cells using quaternary ammonium halide anions and cations. *Nat. Energy* **2**, 17102 (2017).
124. Kim, J., Ho-Baillie, A. & Huang, S. Review of Novel Passivation Techniques for Efficient and Stable Perovskite Solar Cells. *Sol. RRL* **3**, 1800302 (2019).
125. Cho, Y. *et al.* Mixed 3D-2D Passivation Treatment for Mixed-Cation Lead Mixed-Halide Perovskite Solar Cells for Higher Efficiency and Better Stability. *Adv. Energy Mater.* **8**, 1703392 (2018).
126. Grancini, G. *et al.* One-Year stable perovskite solar cells by 2D/3D interface engineering. *Nat. Commun.* **8**, 15684 (2017).
127. Roldán-Carmona, C. *et al.* High efficiency methylammonium lead triiodide perovskite solar cells: the relevance of non-stoichiometric precursors. *Energy Environ. Sci.* **8**, 3550–3556 (2015).
128. Liu, M., Johnston, M. B. & Snaith, H. J. Efficient planar heterojunction perovskite solar cells by vapour deposition. *Nature* **501**, 395–398 (2013).
129. Ross, R. T. Some Thermodynamics of Photochemical Systems. *J. Chem. Phys.* **46**, 4590–4593 (1967).
130. Endres, J. *et al.* Valence and Conduction Band Densities of States of Metal Halide Perovskites: A Combined Experimental–Theoretical Study. *J. Phys. Chem. Lett.* **7**, 2722–2729 (2016).
131. Momblona, C. *et al.* Efficient vacuum deposited p-i-n and n-i-p perovskite solar cells employing doped charge transport layers. *Energy Environ. Sci.* **9**, 3456–3463 (2016).
132. Hutter, E. M. *et al.* Charge Transfer from Methylammonium Lead Iodide Perovskite to Organic Transport Materials: Efficiencies, Transfer Rates, and Interfacial Recombination. *Adv. Energy Mater.* **7**, 1602349 (2017).



Appendices

Cite this: *Chem. Commun.*, 2017, 53, 8707Received 30th May 2017,
Accepted 11th July 2017

DOI: 10.1039/c7cc04149g

rsc.li/chemcomm

Photoluminescence quantum yield exceeding 80% in low dimensional perovskite thin-films *via* passivation control†

 Maria-Grazia La-Placa, Giulia Longo, Azin Babaei, Laura Martinez-Sarti, Michele Sessolo  and Henk J. Bolink *

Quasi-2D perovskites with the BA:MA molar ratio equal to 3:3 show a remarkable PLQY exceeding 80%, thanks to the use of an electron donor as the passivating agent. These films have been applied in LEDs that exhibit high brightness exceeding 1000 cd m⁻² and current efficiencies >3 cd A⁻¹.

Organic–inorganic (hybrid) perovskites are currently one of the most studied semiconducting materials due to the exceptional photovoltaic performance achieved in only a few years of development.¹ Perovskites possess a range of interesting properties, *i.e.* a narrow emission bandwidth, an easily tunable bandgap and high carrier mobility, which make them promising candidates also for light-emitting diodes (LEDs).^{2–6} The exciton binding energy and the rate of radiative recombination of electrons and holes in polycrystalline perovskites are however small, resulting in a photoluminescence quantum yield (PLQY) strongly dependent on the excitation fluence. At low fluence, the PLQY is low, due to the presence of free carriers and trap states which likely mediate non-radiative recombination. At high fluence, all trap states are filled, and both excitonic and bimolecular recombination give rise to luminescence. As for inorganic semiconductors, one way to substantially enhance the luminescence of perovskites is the preparation of nanostructured materials.⁷ In this way, the spatial confinement of electron–hole pairs increases the probability of radiative recombination, with the conditions to efficiently passivate (surface) trap states. Perovskites with reduced dimensionality have been prepared *via* several methods, either using templates^{8,9} or by direct synthesis of perovskite nanoparticles.^{10–13} In the former case, the use of scaffolds such as a wide bandgap metal oxide or polymers inhibits the connectivity needed for efficient charge transport in electroluminescent devices. It has been widely shown that the size of the crystallites in perovskite layers can be substantially reduced by controlling the crystallization rate

from the solution *via* the use of co-solvents or processing additives.^{14,15} Among these, long chain ammonium cations are of particular interest since they can lead to the formation of layered (2D) perovskites. In these materials, sheets of lead halide octahedra are separated by double layers of organic cations.¹⁶ While 2D perovskites are characterized by a very high exciton binding energy (hundreds of meV), the charge transport is limited by their highly anisotropic crystal structures.¹⁷ Recently, efficient electroluminescence has been demonstrated using the so-called “quasi-2D” perovskite phases, an approximation between bulk 3D and 2D polycrystalline materials.^{18–21} These quasi-2D perovskites show a larger exciton binding energy and a shorter exciton diffusion length which are important features to obtain efficient PeLEDs. The morphology and optical properties of these compounds can be readily modified by tuning the relative content of the small and the large cations used, and can be processed into homogeneous films with the grain size in the tens of nanometer range, ensuring a high radiative recombination rate. In the available literature, however, the PLQY values for quasi-2D perovskites do not exceed 60% even at high excitation fluence. Therefore, the improvement of the photoluminescence through the reduction of surface defects and non-radiative recombination in perovskites thin films remains an important challenge.

In this work, we studied the effect of the processing conditions during the deposition of quasi-2D lead bromide perovskites, employing methylammonium (MA) and butylammonium (BA) as the small and large cations, respectively, in an effort to increase the PLQY. As a starting material, we used the (BA)₂(MA)_{n–1}Pb_nX_{3n+1} perovskite with *n* = 5, since a similar stoichiometry with phenethylammonium as large organic cations has been successfully applied in efficient LEDs.^{18,22} By varying the ratio between BA and MA while maintaining the concentration of PbBr₂, and by adjusting the solution-processing parameters, we were able to tune the grain size as well as the overall perovskite film morphology. Importantly, with the addition of an organic semiconductor with electron-donating properties to the non-solvent, we obtained films with a PLQY exceeding 80% even

Instituto de Ciencia Molecular (ICMol), Universidad de Valencia, Catedrático José Beltrán, 2, 46980 Paterna, Spain. E-mail: henk.bolink@uv.es
† Electronic supplementary information (ESI) available. See DOI: 10.1039/c7cc04149g

when measured at very low excitation intensity. These materials are potential candidates to be used as emitting layers in efficient LEDs. We show proof of principle multi-layer devices using organic charge transport layers, characterized by high brightness and current efficiencies.

Perovskite thin films were prepared varying the amount of BABr, MABr and PbBr₂ in dimethyl sulfoxide (DMSO) solutions (see the ESI[†] for details). In particular, the total molar content of BA and MA was kept constant while varying solely their relative molar ratio, without changing the PbBr₂ concentration. We used as the starting compound the quasi-2D perovskite (BA)₂(MA)_{*n*-1}Pb_{*n*}X_{3*n*+1} with *n* = 5, where the BA:MA molar ratio is 2:4. It is important to underline that for higher BA:MA ratios (3:3, 4:2), the stoichiometry deviates from a quasi-2D Ruddlesden–Popper phase. Based on the diffraction patterns obtained from polycrystalline powders of the (3:3) stoichiometry (Fig. S1, ESI[†]), we can estimate that the compound is a low dimensional perovskite with an index *n* close to 3 of a Ruddlesden–Popper phase.¹⁶ However, these compounds represent a useful approximation to study the influence of the long chain cations on the material growth and properties, hence we are referring to them as quasi-2D perovskites in this text. The corresponding archetype 2D and 3D compounds, BA₂PbBr₄ and MAPbBr₃, respectively, were also deposited and used as reference materials. The absorption spectra of the quasi-2D perovskite film series are reported in Fig. 1b. The quasi-2D perovskite with BA:MA = 2:4 shows the typical band-to-band absorption of 3D MAPbBr₃ at about 528 nm, with additional features at 454 nm and 435 nm, characteristic of the 2D BA₂PbBr₄ excitonic absorptions (Fig. 1a). With increasing BA:MA ratio (3:3 and 4:2, Fig. 1b), the excitonic character of these transitions increases (the augmented intensity is due to the higher oscillator strength of the optical transition), as a consequence of the exciton confinement in the inorganic sheets separated by the organic cations. At the same time, the absorption onset at 528 nm slowly disappears, implying that the formation of 2D-type layered perovskites is favored. In fact, the perovskite with the BA:MA ratio of 4:2 shows an additional absorption peak (at about 400 nm), which is characteristic of the pure BA₂PbBr₄ 2D phase (Fig. 1a). Unfortunately, this thin-film series exhibited negligible photoluminescence at the low excitation intensity used in our measurements, *i.e.* monochromatic light at a wavelength of 330 nm from a Xenon lamp coupled to a monochromator (irradiance ~0.1 mW cm⁻²). Since the morphology has a large effect on the

optical properties of perovskites, we manipulated their crystal size through solvent engineering (SE, dripping of a non-solvent during the perovskite formation through spin-coating). The evolution of the absorption spectra for the same perovskite compositions deposited with solvent engineering is reported in Fig. 1c. Independently of the composition, the onset of the absorption (at about 528 nm for the materials without SE, Fig. 1b) is blue shifted, most likely due to a reduction of the grain size and to a modified morphology.²³ At the same time, the excitonic character of the bands associated to 2D and quasi-2D perovskites is reduced, with the 4:2 compound showing an intense and dominant absorption centered at 430 nm. More interesting are the emissive properties of these compounds, now showing bright photoluminescence under excitation at 330 nm (Fig. 1d). This effect is a consequence of the use of solvent engineering, which induces fast crystallization and hence limits the grain growth of the perovskite during deposition. The PL spectral shift follows the trend observed in the optical absorption, blue-shifting from 523 nm to 515 nm and 486 nm when increasing the BA content to BA:MA ratios of 2:4, 3:3 and 4:2, respectively. The corresponding PLQY is below 5% for the 2:4 and 4:2 materials, while the equimolar 3:3 perovskite exhibits a remarkable PLQY of 35%.

It has been shown that a significant gain in the perovskite PLQY can be obtained by (i) dissolving an organic n-type semiconductor in the solvent used for the solvent engineering¹⁴ and (ii) post-deposition treatments with a variety of Lewis bases.²⁴ These approaches have been used to passivate the perovskite surface while avoiding uncontrolled crystallization. Here, we use an n-type molecular semiconductor with a phosphine oxide functionality, 9,9-spirobifluoren-2-yl-diphenylphosphine oxide (SPPO1) (Fig. 2), in order to study its effect on the morphology and optical properties of the perovskite. We added this compound to the chloroform used for the solvent engineering during the deposition of the 3:3 quasi-2D perovskite, which was selected for further studies, being the material with the highest PLQY among the series presented above. The deposition process with the SPPO1 additive has a strong effect on the photoluminescence properties of the perovskite thin-films, resulting in a very high PLQY of 80% (Fig. 2). In spite of the similar absorption spectra (Fig. S2, ESI[†]), these differences might arise from a diminished grain size, as supported by the XRD measurements on such films, where a broadening of the diffraction peaks is observed for the perovskites prepared with solvent engineering and SPPO1 (Fig. S3, ESI[†]). In order to investigate the relationship between the

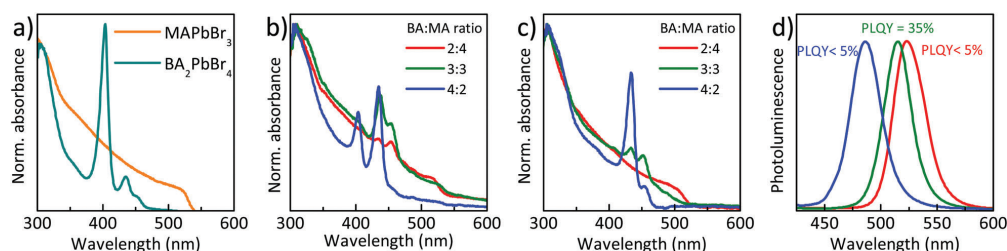


Fig. 1 Absorption spectra in thin-films of (a) the archetype 3D MAPbBr₃ and 2D BA₂PbBr₄ perovskites, and of the intermediate quasi-2D compounds with increasing BA:MA ratio (b) without and (c) with solvent engineering (SE) during deposition. (d) Normalized photoluminescence spectra for the quasi-2D perovskite series under excitation at 330 nm.

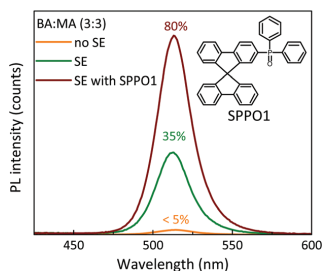


Fig. 2 Photoluminescence spectra under excitation at 330 nm for the quasi-2D compound with equimolar BA:MA ratio, without and with SE, and with SE in the presence of SPP01. The corresponding PLQY and the chemical structure of SPP01 are also reported.

morphology and the PLQY trend, the perovskite thin films were analyzed by atomic force microscopy (AFM). Fig. 3 shows the AFM topographies with the corresponding profiles for the 3:3 quasi-2D perovskite films, prepared without solvent engineering, with solvent engineering and in the presence of the SPP01 passivating agent (Fig. 3c). Clearly, the simple one-step spin-coating does not yield a homogeneous perovskite film (Fig. 3a), leading to incomplete coverage and significant height variation through the sample surface. This is due to the uncontrolled crystallization during the film formation. On the other hand, the chloroform dripping drastically reduces the grain size, leading to a more flat and homogeneous surface (Fig. 3b). In the presence of SPP01, the average grain size appears to be further reduced, as well as the overall homogeneity of the sample surface. The peak to peak roughness R_{PTP} value diminishes from 105 nm for the samples without SE treatment to 80 nm and 70 nm for the quasi-2D perovskite films obtained after SE with CHCl_3 and SE with CHCl_3 and SPP01, respectively. In order to shed light on the role of SPP01 during solvent engineering, we performed time-resolved PL (TRPL) measurements on the nanosecond scale on thin films with and without SPP01. In contrast to previous reports for MAPbI_3 films after passivation,²⁴ we observed that the PL lifetime is essentially unchanged (Fig. S4, ESI[†]). This finding can be explained by considering that with TRPL measurements only the radiative recombination channels can be monitored. If non-radiative recombination

takes place through another deactivation pathway, passivation would hinder such processes resulting in a higher PLQY, without altering the observed PL lifetime. Hence the remarkable PLQY observed is the result of a synergistic effect of (i) the choice of a suitable BA:MA ratio, (ii) the use of solvent engineering and (iii) the introduction of an electron-donating molecule such as SPP01, taking part not only in the control of the grain size but also in removing non-radiative recombination channels. These materials are potentially suited for applications in LEDs (high PLQY and morphological quality, and low roughness), hence they were incorporated into multilayer devices with a p-i-n configuration (the anode is the transparent contact). The device structure consists of an ITO/PEDOT:PSS transparent anode, a perovskite thin-film emitter, a thermally evaporated electron transport layer (ETL), 1,3-bis[3,5-di(pyridin-3-yl)]benzene (BmPyPhB, 40 nm), and a metal cathode (Ba 10 nm, Ag 100 nm). The flat band energy diagram for this set of materials is depicted in Fig. 4a. The LEDs were characterized by measuring the current density versus voltage characteristics (J - V) and monitoring the electroluminescence with a sensitive Si photodiode (Fig. 4b). We observed electroluminescence at a low applied bias (3.5 V), increasing rapidly until it reaches about 1000 cd m^{-2} at 8 V. Despite the high luminance, these devices showed a rather high current density, which limits the overall current efficiency to 1.3 cd A^{-1} . This phenomenon might arise from the partial solubility of PEDOT:PSS in the solvent used for the perovskite processing (DMSO), hindering the formation of a well-defined interface between the hole injection and the emissive layers. In order to improve the PEDOT:PSS stability and its adhesion to the substrate, we added to its suspensions a small amount (1 v/v%) of 3-glycidyloxypropyltrimethoxysilane (GOPS) as a cross-linking agent.²⁵ Therefore, we prepared and characterized LEDs with the same structure as described above using the modified hole injection layer. As a result of the cross-linking of PEDOT:PSS, the leakage current is substantially reduced, leading to the expected J - V curve for a high quality diode. At the same time, we observed a lower turn-on voltage for electroluminescence (2.8 V), indicating a better charge injection into the perovskite emitter. The luminance rapidly increases reaching a brightness of about 1000 cd m^{-2} at 8 V, with green emission analogous to the PL spectrum of the material (see Fig. S5 in the ESI[†]). More importantly, the maximum current efficiency reaches 3.3 cd A^{-1} at 5 V. Despite the promising performance of the LEDs, if one considers the

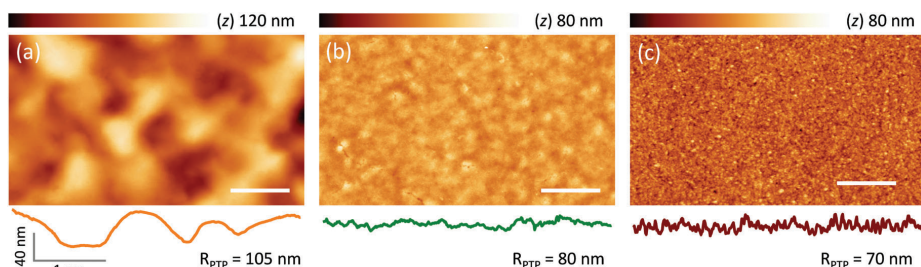


Fig. 3 AFM topographies of the quasi-2D perovskite films with equimolar BA:MA ratio (3:3), (a) without and (b) with SE, and (c) with SE in the presence of SPP01. The corresponding surface profile is shown at the bottom of each picture.

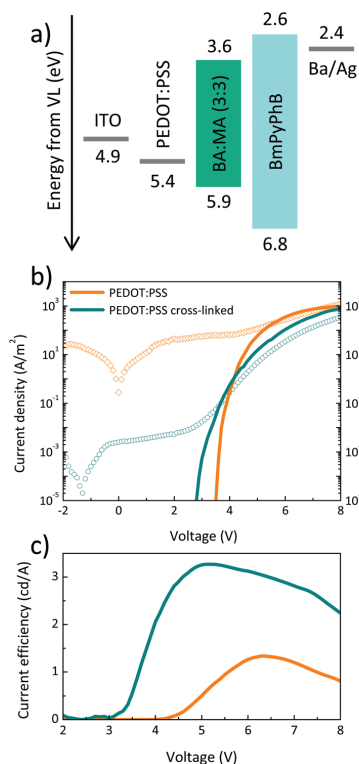


Fig. 4 (a) Schematic flat energy level diagram for the set of materials used, referred to the vacuum level (VL) (values from ref. 21 and 26). (b) Current density and luminance and (c) current efficiency versus applied bias for the LEDs prepared with and without cross-linked PEDOT:PSS.

extremely high PLQY (80%) of the perovskite emitter, it is obvious that other loss mechanisms are hindering efficient electroluminescence. In particular, further improvements might be obtained with the use of a hole-selective material, capable of assisting the hole injection while confining the electrons into the perovskite film. In summary, we were able to obtain a remarkable PLQY of 35% for quasi-2D perovskites with a 3:3 BA:MA ratio. We showed also a novel strategy to further enhance the PLQY; in particular, the addition to the non-solvent of an organic semiconductor with electron donating properties, which is able to efficiently passivate surface states reducing non-radiative recombination channels. Through this method, we obtained PLQY exceeding 80%. Thin-films of these materials have been applied in multilayer LEDs which showed a low current leakage and a low turn-on voltage for electroluminescence, a high brightness of about 1000 cd m^{-2} and a maximum current efficiency of 3.3 cd A^{-1} .

We acknowledge financial support from the European Union H2020 project SOLEDLIGHT (grant 643791), Spanish Ministry of Economy and Competitiveness (MINECO) via the Unidad de

Excelencia María de MDM-2015-0538, MAT2014-55200 and PCIN-2015-255 and the Generalitat Valenciana (Prometeo/2016/135). M. G. L. P. acknowledges support from a Grisolia grant (GRISOLIA/2015/A/146). L. M. S. and M. S. thank the MINECO for a pre-doctoral and a post-doctoral contract (FPI and JdC), respectively.

References

- J.-P. Correa-Baena, A. Abate, M. Saliba, W. Tress, T. Jesper Jacobsen, M. Gratzel and A. Hagfeldt, *Energy Environ. Sci.*, 2017, **10**, 710–727.
- G. Xing, N. Mathews, S. S. Lim, N. Yantara, X. Liu, D. Sabba, M. Gratzel, S. Mhaisalkar and T. C. Sum, *Nat. Mater.*, 2014, **13**, 476–480.
- S. D. Stranks and H. J. Snaith, *Nat. Nanotechnol.*, 2015, **10**, 391–402.
- B. R. Sutherland and E. H. Sargent, *Nat. Photonics*, 2016, **10**, 295–302.
- P. Docampo and T. Bein, *Acc. Chem. Res.*, 2016, **49**, 339–346.
- N. Yantara, S. Bhaumik, F. Yan, D. Sabba, H. A. Dewi, N. Mathews, P. P. Boix, H. V. Demir and S. Mhaisalkar, *J. Phys. Chem. Lett.*, 2015, **6**, 4360–4364.
- K. Zheng, Q. Zhu, M. Abdellah, M. E. Messing, W. Zhang, A. Generalov, Y. Niu, L. Ribaud, S. E. Canton and T. Pullerits, *J. Phys. Chem. Lett.*, 2015, **6**, 2969–2975.
- K. Akihiro, I. Masashi, T. Kenjiro and M. Tsutomu, *Chem. Lett.*, 2012, **41**, 397–399.
- G. Longo, A. Pertegas, L. Martínez-Sarti, M. Sessolo and H. J. Bolink, *J. Mater. Chem. C*, 2015, **3**, 11286–11289.
- F. Zhang, H. Zhong, C. Chen, X.-G. Wu, X. Hu, H. Huang, J. Han, B. Zou and Y. Dong, *ACS Nano*, 2015, **9**, 4533–4542.
- L. Protesescu, S. Yakunin, M. I. Bodnarchuk, F. Krieg, R. Caputo, C. H. Hendon, R. X. Yang, A. Walsh and M. V. Kovalenko, *Nano Lett.*, 2015, **15**, 3692–3696.
- S. González-Carrero, R. E. Galian and J. Pérez-Prieto, *Part. Part. Syst. Charact.*, 2015, **32**, 709–720.
- L. C. Schmidt, A. Pertegas, S. González-Carrero, O. Malinkiewicz, S. Agouram, G. Mínguez Espallargas, H. J. Bolink, R. E. Galian and J. Pérez-Prieto, *J. Am. Chem. Soc.*, 2014, **136**, 850–853.
- H. Cho, S.-H. Jeong, M.-H. Park, Y.-H. Kim, C. Wolf, C.-L. Lee, J. H. Heo, A. Sadhanala, N. Myoung, S. Yoo, S. H. Im, R. H. Friend and T.-W. Lee, *Science*, 2015, **350**, 1222–1225.
- N. J. Jeon, J. H. Noh, Y. C. Kim, W. S. Yang, S. Ryu and S. I. Seok, *Nat. Mater.*, 2014, **13**, 897–903.
- C. C. Stoumpos, D. H. Cao, D. J. Clark, J. Young, J. M. Rondinelli, J. I. Jang, J. T. Hupp and M. G. Kanatzidis, *Chem. Mater.*, 2016, **28**, 2852–2867.
- D. B. Mitzi, K. Chondroudis and C. R. Kagan, *IBM J. Res. Dev.*, 2001, **45**, 29–45.
- M. Yuan, L. N. Quan, R. Comin, G. Walters, R. Sabatini, O. Voznyy, S. Hoogland, Y. Zhao, E. M. Beauregard, P. Kanjanaboos, Z. Lu, D. H. Kim and E. H. Sargent, *Nat. Nanotechnol.*, 2016, **11**, 872–877.
- J. Byun, H. Cho, C. Wolf, M. Jang, A. Sadhanala, R. H. Friend, H. Yang and T.-W. Lee, *Adv. Mater.*, 2016, **28**, 7515–7520.
- N. Wang, L. Cheng, R. Ge, S. Zhang, Y. Miao, W. Zou, C. Yi, Y. Sun, Y. Cao, R. Yang, Y. Wei, Q. Guo, Y. Ke, M. Yu, Y. Jin, Y. Liu, Q. Ding, D. Di, L. Yang, G. Xing, H. Tian, C. Jin, F. Gao, R. H. Friend, J. Wang and W. Huang, *Nat. Photonics*, 2016, **10**, 699–704.
- Z. Xiao, R. A. Kerner, L. Zhao, N. L. Tran, K. M. Lee, T.-W. Koh, G. D. Scholes and B. P. Rand, *Nat. Photonics*, 2017, **11**, 108–115.
- L. N. Quan, Y. Zhao, F. P. García de Arquer, R. Sabatini, G. Walters, O. Voznyy, R. Comin, Y. Li, J. Z. Fan, H. Tan, J. Pan, M. Yuan, O. M. Bakr, Z. Lu, D. H. Kim and E. H. Sargent, *Nano Lett.*, 2017, **17**, 3701–3709.
- V. D'Innocenzo, A. R. Srimath Kandada, M. De Bastiani, M. Gandini and A. Petrozza, *J. Am. Chem. Soc.*, 2014, **136**, 17730–17733.
- D. W. deQuilletes, S. Koch, S. Burke, R. K. Paranjli, A. J. Shropshire, M. E. Ziffer and D. S. Ginger, *ACS Energy Lett.*, 2016, **1**, 438–444.
- J. Rivnay, S. Inal, B. A. Collins, M. Sessolo, E. Stavrinidou, X. Strakoskas, C. Tassone, D. M. Delongchamp and G. G. Malliaras, *Nat. Commun.*, 2016, **7**, 11287.
- N. Darmawan, C.-H. Yang, M. Mauro, R. Frohlich, L. De Cola, C.-H. Chang, Z.-J. Wu and C.-W. Tai, *J. Mater. Chem. C*, 2014, **2**, 2569–2582.



Cite this: *J. Mater. Chem. C*, 2020, **8**, 1902

Received 4th December 2019,
Accepted 23rd January 2020

DOI: 10.1039/c9tc06662d

rsc.li/materials-c

Dual-source vacuum deposition of pure and mixed halide 2D perovskites: thin film characterization and processing guidelines†

Maria-Grazia La-Placa,^a Dengyang Guo,^b Lidón Gil-Escrig,^c Francisco Palazon,^{id}^a Michele Sessolo ^{id}*^a and Henk J. Bolink ^{id}^a

The dual-source vacuum deposition of 2D perovskite films of the type PEA_2PbX_4 (PEA = phenethylammonium and $\text{X} = \text{I}^-$, Br^- , or a combination of both) is presented. Low-temperature deposited 2D perovskite films showed high crystallinity with the expected trend of bandgap as a function of halide type and concentration. Importantly, we observed an unavoidable halide cross-contamination among different deposition runs, as well as a strong dependence of the material quality on the type of halide precursors used. These findings should be taken into account in the development of vacuum processing for low-dimensional mixed halide perovskites.

Two-dimensional (2D), layered perovskites are a wide family of semiconductors with general formula $(\text{R-NH}_3)_2\text{MX}_4$, where inorganic sheets of corner-sharing metal (M, mostly Pb^{2+} and Sn^{2+}) halide (X) octahedra are separated by bilayers of aliphatic or aromatic mono-ammonium cations (R-NH_3), or single layers of diammonium cations.^{1,2} 2D perovskites present a large compositional flexibility, which makes it possible to design and modulate their electrical and optical properties for specific applications. A wide spectrum of materials can be obtained through simple substitution of the halide anion and organic cations.³ As in the analogous 3D perovskites,⁴ halide substitution/mixing results in marked changes of the optical properties, as the valence band is formed from a mixture of metal s-orbitals and halide p-orbitals, while the conduction band is composed mainly of metal p-orbitals. Increasing the halide electronegativity (from I to Br and Cl) results in a significant downward shift of the valence band maximum and, to a less extent, in an upward shift of the conduction band minimum, thereby increasing the bandgap (E_g).^{5,6} In low dimensional perovskites, due to the alternation of

inorganic semiconducting and organic insulating sheets, electrons and holes are confined within the inorganic framework, causing quantum and dielectric confinement effects.⁷ These lead to a much higher exciton binding energy (E_b) in 2D perovskites (hundreds of meV) compared to the 3D counterparts (tens of meV).^{8,9} In contrast to 3D perovskites, 2D perovskites offer also less restrictions on the size of the cations that can be accommodated between the inorganic sheets, in compliance with the Goldschmidt tolerance parameter.^{10,11} While the length of the organic cation has only minor effects on the electronic and optical properties of the semiconductor, its dielectric constant ϵ_{org} (which varies depending on the chemical structure of the cation), can be used as a tool to influence E_g and E_b .^{9,12,13} A high E_b limits the conversion of excitons to free carriers and consequently the charge carrier mobility in pure 2D perovskites. The latter can be recovered by increasing the thickness of the inorganic slabs such as in 2D Ruddlesden–Popper perovskites.¹⁴ Thanks to the possibility to modulate the optical and electronic properties, 2D perovskites have been investigated for several applications, such as electroluminescence devices (LEDs),^{15,16} field effect transistors (FETs),¹⁷ photodetectors^{18,19} and solar cells.^{20–22} 2D perovskites were initially studied in the 1990s and recently the interest towards this family of semiconductors is resurgent. While solution processing and single crystal fabrication of 2D hybrid perovskites have been widely reported, vacuum processing of these materials remains rather unexplored. To the best of our knowledge, only one report exists on fully co-evaporated 2D perovskites,²³ while other works have described a sequential vacuum-deposition and a flash evaporation of low-dimensional Ruddlesden–Popper perovskite films.^{11,24–26} Vacuum deposition presents important advantages over solution-based methods, such as the fine control over the film thickness, high material purity, and it being intrinsically additive. Moreover, it eliminates the issues related to the use of solvents such as the solubility limit of the precursors and the presence of resilient solvents in the final film.²⁷

In this work, we report the synthesis of different pure and mixed halide 2D perovskites by dual source vacuum deposition

^a Instituto de Ciencia Molecular, Universidad de Valencia, C/Beltrán 2, Paterna, 46980, Spain. E-mail: michele.sessolo@uv.es

^b Department of Chemical Engineering, Delft University of Technology, Delft, 2629 HZ, The Netherlands

^c Helmholtz-Zentrum Berlin für Materialien und Energie GmbH, Young Investigator Group for Perovskite Tandem Solar Cells, Kekuléstraße 5, Berlin, 12489, Germany

† Electronic supplementary information (ESI) available. See DOI: 10.1039/c9tc06662d

and we investigated their structural, optical and charge transport properties. We deposited pure phenethylammonium lead iodide (PEAI)₂PbI₄ and phenethylammonium lead bromide (PEABr)₂PbBr₄ by sublimation of the corresponding organic ammonium and metal halides, phenethylammonium iodide (PEAI), phenethylammonium bromide (PEABr), lead iodide (PbI₂) and lead bromide (PbBr₂). Furthermore, we explore the preparation of mixed halide compounds using different organic and lead halide precursors. In particular, we co-deposited perovskite films using PEABr and PbI₂ as well as PEAi and PbBr₂, respectively. The 2D films were deposited by simultaneous co-deposition of the precursors, after the calibration of the deposition rate of each compound. The calibration factors were obtained by comparing the thickness of the thin-films as detected from the quartz crystal microbalance sensors with that measured with a mechanical profilometer. Organic salts are often not thermally stable and not easy to sublime due to the possible dissociation into their volatile precursors.²⁸ However, once properly outgassed in a high vacuum chamber, PEAi and PEABr can be sublimed with a low and stable rate at the minimum temperature required for evaporation, around 160 °C. The inorganic materials were sublimed at temperatures ranging from 260 to 300 °C.

The mixed halide (PEAI)₂PbBr₂I₂ perovskite films were prepared with the same procedure and will be described in the text as (PEABr)₂PbI₂ when deposited by co-sublimation of PEABr and PbI₂ and as (PEAI)₂PbBr₂ in the case of PEAi and PbBr₂ co-evaporation. All the thin film depositions were performed in the same vacuum chamber. The relative deposition rate of the organic halides and lead salts was 2 : 1, accordingly with the compound's stoichiometry. Details of the thin-film deposition are provided in the ESI.†

The structural features of the layered perovskite were studied by X-ray diffraction (XRD) on co-sublimed thin films (Fig. 1 and Fig. S1, ESI†). As can be seen from Fig. S1 (ESI†), vacuum-deposited films of (PEA)₂PbX₄ (X = Br or I) show similar diffractograms before and after thermal annealing, albeit with more intense and sharper diffraction peaks for annealed samples (especially in the bromide case). This suggests that crystallization of the desired materials occurs directly during the deposition process at room temperature, while crystallinity can be slightly enhanced after a short thermal annealing at 100 °C. Therefore, we performed thermal annealing as a standard process for all compositions. Whole-pattern Le Bail refinements (solid lines) were performed on the acquired diffractograms (open circles)

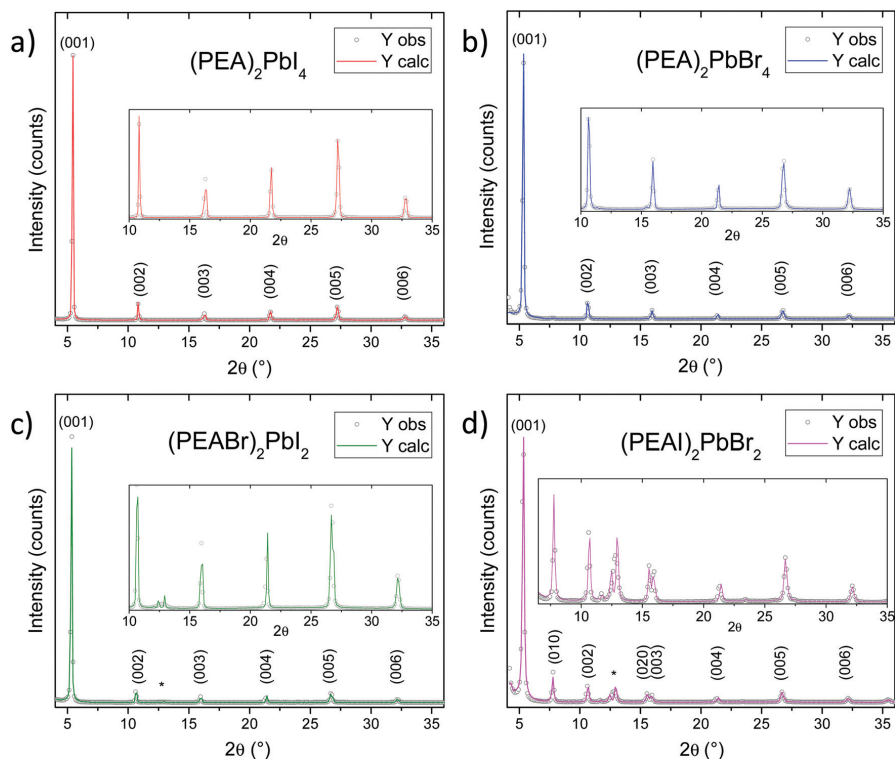


Fig. 1 X-ray diffraction analysis of 200 nm thick, vacuum-deposited 2D perovskite thin films after annealing for 5 min at 100 °C. "Y obs" indicates the experimental traces while "Y calc" indicates the calculated intensities based on whole-pattern fitting (Le Bail refinement).

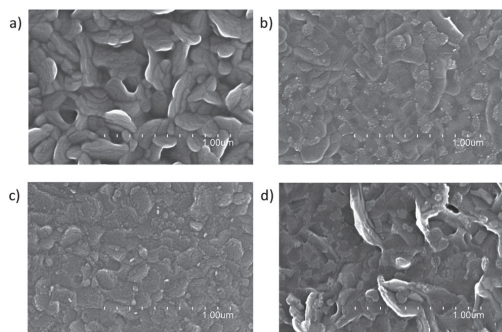
Table 1 Lattice parameters derived from Le Bail fits of different samples. Space group = $P\bar{1}$

Sample	<i>a</i> (Å)	<i>b</i> (Å)	<i>c</i> (Å)	α (°)	β (°)	γ (°)
(PEA) ₂ PbI ₄	11.49	11.73	17.14	99.63	105.36	89.85
(PEA) ₂ PbBr ₄	11.60	11.63	17.51	99.57	105.55	89.83
(PEABr) ₂ PbI ₂	11.60	11.63	17.49	99.61	105.62	89.81
(PEAI) ₂ PbBr ₂	11.60	11.56	17.48	99.59	105.67	89.79

with Fullprof software (see experimental section for details). Fig. 1 shows that all diffractograms can be well-fitted by considering a $P\bar{1}$ space group with varying lattice parameters as detailed in Table 1.

Table 1 shows that as the halogen becomes smaller, the *c*-axis parameter, perpendicular to the inorganic perovskite sheets, increases from 17.14 Å for (PEA)₂PbI₄ to 17.51 Å for (PEA)₂PbBr₄. Qualitatively, this can be clearly seen by a shift of the corresponding (001) peaks to lower angles (see comparison in Fig. S2, ESI[†]). This behavior, which could be considered counterintuitive, has already been reported on the same and in similar materials, and it has been attributed to a different orientation of the phenethylammonium cations between the inorganic layers.^{29,30} When the octahedra contract (due to smaller and more electronegative halides), the alkylic substituents of the organic cations will adopt a higher angle with respect to the surface of the inorganic slabs and result in a larger distance between them. Furthermore, it is obvious from Fig. 1 that all films show a preferential orientation along the [001] direction (*i.e.*, perovskite slabs parallel to the substrate). This is common for 2D perovskites and 2D materials in general, but not favorable for charge transport within a thin film device.^{31–34} In the case of the (PEAI)₂PbBr₂ sample prepared from co-sublimation of PEAi and PbBr₂, we also note intense reflections for the (010) and (020) planes at $2\theta = 7.8^\circ$ and $2\theta = 15.6^\circ$, respectively as well as a broad signal around $2\theta = 12.8^\circ$, which could be attributed to a combination of (1–11) and (–1–12) planes and possibly PbI₂ formed from co-sublimation. Hence, it appears that this sample shows a more heterogeneous crystallinity.

The morphology of the 2D perovskite films was studied by scanning electron microscopy (SEM, Fig. 2) and atomic force microscopy (AFM, ESI[†] Fig. S4). The top-view SEM image of the

**Fig. 2** SEM pictures of vacuum deposited (a) (PEA)₂PbI₄, (b) (PEA)₂PbBr₄, (c) (PEABr)₂PbI₂ and (d) (PEAI)₂PbBr₂ thin-films.**Table 2** Root mean square roughness R_{RMS} and average height z_{AVG} of the 2D perovskite films

Sample	R_{RMS} (nm)	z_{AVG} (nm)
(PEA) ₂ PbI ₄	25.8	95.0
(PEA) ₂ PbBr ₄	10.9	28.3
(PEABr) ₂ PbI ₂	4.0	14.1
(PEAI) ₂ PbBr ₂	29.2	74.8

(PEA)₂PbI₄ perovskite (Fig. 2a) shows well-defined, randomly distributed platelets formed by multiple grains with size ranging from 200 nm to 400 nm. The surface was found to be rather rough, with a quite high root mean square roughness and average height (Table 2 and Fig. S4a, ESI[†]). The pure bromide (PEA)₂PbBr₄ perovskite films are also characterized by the presence of platelets, this time more compact compared to the iodide counterpart. The grain size is in the range of hundreds of nanometers and the topography is characterized by a reduced R_{RMS} and a z_{AVG} (Table 2 and Fig. S4b, ESI[†]). The morphology and grain size of the mixed (PEABr)₂PbI₂ perovskite films was found to be very similar to the pure bromide 2D films, although with a much flatter topography as described in Table 2. Finally, the (PEAI)₂PbBr₂ films (Fig. 2d) present a more heterogeneous morphology, with small platelets and large lamellar aggregates, resulting in a very rough surface, also in this case with high R_{RMS} and z_{AVG} values (Table 2 and Fig. S4d, ESI[†]). The overall high roughness of the vacuum deposited 2D perovskite films might be related with the slow sublimation of the precursors towards the substrate. Due to the highly oriented crystal structure of 2D perovskite and the high reactivity and affinity of the precursors, the grain growth proceeds faster than the nucleation rate, resulting in rough films with large platelets and other out-of-plane structures.

The steady state optical characterization of the vacuum-deposited 2D perovskite films is presented in Fig. 3. The optical absorption of the (PEA)₂PbI₄ films shows a band in the UV and an intense excitonic peak centered at 503 nm, with a full width at half maximum (FWHM) of 35 nm. When the film of (PEA)₂PbI₄ was excited with a LED at 340 nm, intense photoluminescence (yellow dashed line) centered at 521 nm was observed. The peak has a FWHM of 24 nm and a Stokes shift of 80 meV. The values of Stokes shift and FWHM are larger than the ones seen for (PEA)₂PbI₄ thin films prepared by solution processing (see ESI[†] Fig. S3).

The 2D (PEA)₂PbBr₄ film exhibits the expected optical absorption band at a higher energy, compared to the analogous iodide compound, with a very sharp excitonic peak (FWHM = 15 nm) centered at 403 nm. However, another weak absorption band was detected at 434 nm, which cannot be ascribed to the pure (PEA)₂PbBr₄ phase. Intense and narrow photoluminescence centered at 410 nm and with FWHM of 17 nm was observed, with a small Stokes shift of 60 meV. The excitonic absorption and PL peaks of the vacuum-deposited (PEA)₂PbBr₄ 2D perovskite agrees well with the results obtained from solution-processed films, in terms of Stokes shift and FWHM (see ESI[†] Fig. S3). However, two other peaks were systematically detected in the PL spectrum, a low intensity peak centered at 434 nm and a more intense and

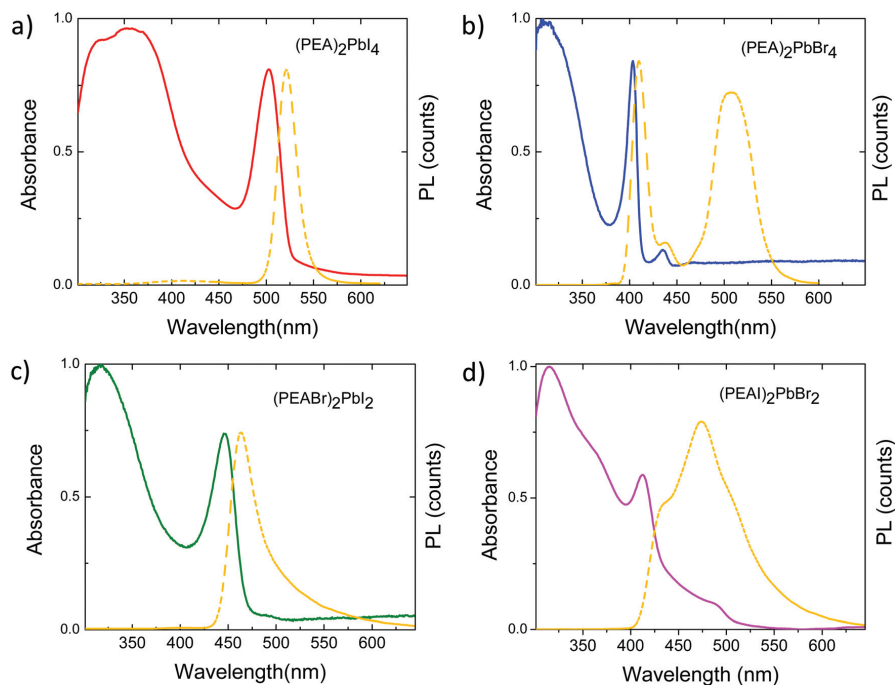


Fig. 3 Optical absorption and photoluminescence spectra (excitation at 340 nm) of 200 nm thick films of (a) $(\text{PEA})_2\text{PbI}_4$, (b) $(\text{PEA})_2\text{PbBr}_4$, (c) $(\text{PEABr})_2\text{PbI}_2$ and (d) $(\text{PEAI})_2\text{PbBr}_2$ perovskites.

broad band centered at 507 nm. Most likely, the additional small intensity peak can be associated with the presence of a bromide-rich, mixed bromide/iodide phase, while the broad PL band at a lower energy can be ascribed to the formation of an iodide-rich phase. These considerations point towards a possible halide cross-contamination in the evaporation chamber, which was used for the vacuum processing of both $(\text{PEA})_2\text{PbBr}_4$ and PEA_2PbI_4 perovskites. In order to verify this hypothesis, we carried out energy-dispersive X-ray spectroscopy (EDS) on the films in a scanning electron microscope (SEM). In the 2D $(\text{PEA})_2\text{PbI}_4$ films, we found an I/Br ratio of 14.3, indicating that approximately 6% of the total halide content comes from bromide. In the case of the 2D $(\text{PEA})_2\text{PbBr}_4$ perovskite, the Br/I ratio was as low as 3.5, meaning that as much as 22% of the total halide content is due to iodide contamination. The EDS analysis justified the observed optical properties of the perovskite film, and clearly indicates that there is cross-contamination between different precursors from different vacuum-deposition runs. Interestingly, in the case of the 2D $(\text{PEA})_2\text{PbI}_4$ films, there is a rather low bromide contamination, while the contamination of iodide in 2D $(\text{PEA})_2\text{PbBr}_4$ films is more relevant. The contamination can be due to (i) re-evaporation of previously deposited materials from the surface of the chamber or even to (ii) halide exchange between the subliming vapors and the chamber itself. These processes can be more or less pronounced depending on the

volatility of the materials as well as on their chemical reactivity, as observed in our iodide and bromide compounds.

The optical absorption of the mixed halide $(\text{PEABr})_2\text{PbI}_2$ perovskite (Fig. 3c), deposited by dual source sublimation of PEABr and PbI_2 , was found to be blue shifted with respect to that of the $(\text{PEA})_2\text{PbI}_4$ and red-shifted compared to $(\text{PEA})_2\text{PbBr}_4$, as expected for a mixed halide perovskite. The excitonic absorption was centered at 446 nm (FWHM = 36 nm), while the PL peak was found to be asymmetric with a maximum at 464 nm (FWHM = 34 nm), implying a large Stokes shift of 110 meV. The EDS analysis revealed a Br/I ratio of 0.9, very close to the expected stoichiometry for the $(\text{PEABr})_2\text{PbI}_2$ perovskite and with only a negligible 2% excess of iodide. At this halide ratio, 3D perovskites usually show halide segregation effects,³⁵ due to the poor miscibility of the iodide and bromide phases. For this reason, we studied the evolution of the PL over time under continuous laser irradiation (375 nm, Fig. S5, ESI†). Immediately after illumination, we noted the presence of the previously observed high energy peak at 464 nm with a weak component at a lower energy (approximately 500 nm). With continuous irradiation, the low energy component dominates the PL spectrum, implying the formation of iodide-rich phases where carriers are efficiently transferred and radiatively recombined. This is hence in agreement with what is generally observed for other mixed halide perovskites.

Rather different optical properties were observed for the other mixed halide (PEAI)₂PbBr₂ perovskite films, obtained by simultaneous sublimation of PEA and PbBr₂. The absorption spectrum in Fig. 3d shows an excitonic peak at 412 nm, close to that of the pure bromide compounds (PEA)₂PbBr₄, and a weak absorption at approximately 490 nm, which is close to the excitonic absorption of the pure iodide (PEA)₂PbI₄ perovskite. This behavior suggests the coexistence of different domains, as also confirmed by the PL spectrum, which shows a broad band composed of several peaks: one with a maximum at approximately 434 nm and a second, more intense at 475 nm with a shoulder around 504 nm. The optical characteristics are consistent with the presence of a dominant, bromide-rich phase and a second iodide-rich one. This hypothesis is supported by the elemental analysis, which revealed a Br/I ratio of 1.8, implying that approximately 65% of the halide consists of bromide. The high bromide content of the (PEAI)₂PbBr₂ films could also partially explain why the corresponding unit cell parameters are close to those of the (PEA)₂PbBr₄ (Table 1). When PbBr₂ is reacting with PEA during the co-deposition process, the halide exchange is limited to an iodide inclusion of about only 30–40 mol%. On the other hand, the co-deposition of PbI₂ and PEABr was found to lead to perovskites with a well-balanced halide content. This phenomenon could be ascribed either to a higher chemical reactivity of PEABr, or to a higher stability of PbBr₂ compared to PbI₂. Some literature points towards the latter hypothesis, as the energetic stability of lead halides increases with increasing halide electronegativity (from iodide to bromide).^{36,37}

The vacuum-deposited 2D perovskite films were further studied by means of time-resolved microwave conductivity (TRMC). Fig. 4 shows the time-dependent photoconductivity traces for all the 2D perovskites reported here. Three different excitation wavelengths (pulsed laser excitation at 510 nm, 403 nm and 445 nm) were applied according to the maximum absorption at the excitonic peak of each compound. Upon excitation, electron–hole pairs are generated within the inorganic sheets of the 2D perovskite and, due to the strong confinement (large E_b), they will mostly exist as bound excitons, hence not contributing to the photoconductance.

This is important as in these compounds, the TRMC signal is not directly a measure of the charge mobility, but rather its product with the free carrier generation yield.¹⁴

From the maximum change in TRMC signal (Fig. 4a) recorded with an excitation density on the order of 10¹² photons per cm², one can immediately observe that the pure iodide 2D compound (PEA)₂PbI₄ presents a larger photoconductance (0.1 cm² V⁻¹ s⁻¹) as compared to the bromide and mixed halide analogs. The photoconductance of (PEA)₂PbI₄ is consistent with the low yield of exciton dissociation into mobile carriers, and is comparable to previously reported values for similar solution-processed 2D perovskite films.¹⁴ The lower absolute photoconductance observed for (PEA)₂PbBr₄ and mixed (PEABr)₂PbI₂ and (PEAI)₂PbBr₂ films can be ascribed to the lower crystal/grain size, as observed by electron microscopy (Fig. 2). Among these materials, the larger grains in (PEAI)₂PbBr₂ films might hence be responsible for the slightly higher photoconductance observed for this specific compound (0.02 cm² V⁻¹ s⁻¹). In order to evaluate the charge carrier recombination, the TRMC traces were normalized (Fig. 4b) allowing a direct comparison of the recombination lifetime $t_{1/2}$ (time after excitation when the charge carrier concentration drops to 1/2 of its initial value). Interestingly, the pure bromide (PEA)₂PbBr₄ perovskite showed a longer lifetime (160 ns) compared to the pure 2D iodide films ($t_{1/2}$ = 70 ns). This trend is somewhat unexpected, as E_b was reported to increase when moving from iodide to bromide perovskites, implying a lower photoconductance, but also a lower lifetime for bromide compounds.³⁸ The larger lifetime is hence most likely correlated with the presence of iodide in (PEA)₂PbBr₄, acting as carrier traps and causing slower charge recombination within the material. Finally, the overall lower lifetimes observed for the mixed compounds (40 ns) correlates with an increased disorder due to the presence of mixed halide domains. In all cases, the lifetime values observed here well compare with the literature data.¹⁴

In summary, we have presented the dual-source vacuum deposition of 2D perovskite films of the type PEA₂PbX₄, where PEA is phenethylammonium and X stands for I⁻, Br⁻, or a combination of both. As for vacuum-deposited 3D perovskite films,

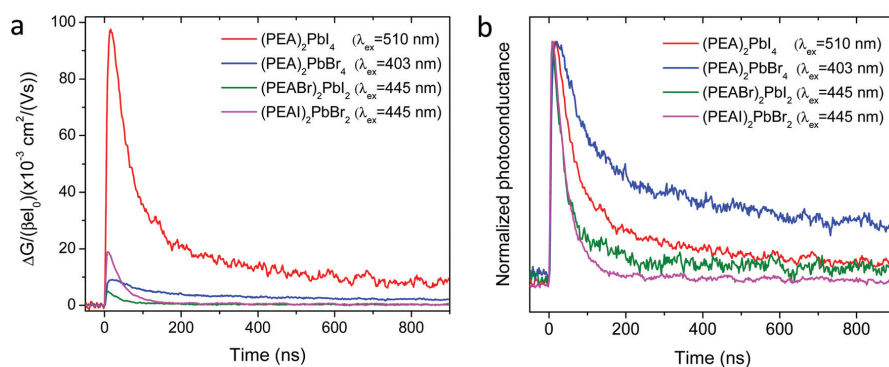


Fig. 4 (a) Time-resolved microwave conductivity traces of vacuum-deposited 2D perovskite selectively excited at 510, 403 and 445 nm. (b) Normalized time-dependent photoconductance of the same sample series.

we observed a high degree of crystallinity for all 2D compounds even at room temperature, a remarkable feature which is advantageous for the fabrication of multilayer perovskite stacks. The 2D perovskite films exhibited the expected trend in bandgap, increasing from the pure iodide to pure bromide materials, and intermediate for the mixed halide compounds. Through the series of experiments carried out here, we have observed an unavoidable halide cross-contamination among different deposition runs. Its implication is particularly relevant for the fabrication of wide bandgap perovskite films (here $(\text{PEA})_2\text{PbBr}_4$), where the presence of iodide unavoidably results in multiple luminescence features due to the heterogeneous energy landscape within the semiconductor. Hence, it is mandatory to have a dedicated chamber for a given composition in order to ensure the formation of high purity perovskite compounds. We have also investigated the preparation of mixed I/Br 2D perovskites by co-sublimation of either PEA-I and PbBr_2 or *vice versa*. Interestingly, Br/I 1:1 stoichiometry could only be obtained when using PbI_2 and PEABr, most likely due to the higher reactivity of PbI_2 (as compared to the more stable PbBr_2) towards the organic cations. This is another important observation to be considered when designing vacuum deposition of low-dimensional, mixed halide compounds. The materials were also analyzed by time-resolved microwave conductivity (TRMC). The pure iodide PEA_2PbI_4 showed photoconductance and lifetime values in agreement with previously reported solution-processed thin films, making it an interesting candidate for implementation in multilayer optoelectronic devices.

Conflicts of interest

There are no conflicts to declare.

Acknowledgements

The research leading to these results has received funding from the European Union Programme for Research and Innovation Horizon 2020 (2014–2020) under the Marie Skłodowska-Curie Grant Agreement PerovSAMs No. 747599 and the Spanish Ministry of Economy and Competitiveness (MINECO) *via* the Unidad de Excelencia María de Maeztu MDM-2015-0538, MAT2017-88821-R, RTI2018-095362-A-I00, PCIN-2015-255, PCIN-2017-014, and the Generalitat Valenciana (Prometeo/2016/135). M. S. acknowledges the MINECO for his RyC contract. D. G. acknowledges the funding from the China Scholarship Council (CSC).

Notes and references

- D. B. Mitzi, K. Chondroudis and C. R. Kagan, *IBM J. Res. Dev.*, 2001, **45**, 29–45.
- A. Lemmerer and D. G. Billing, *CrystEngComm*, 2012, **14**, 1954.
- M. D. Smith, B. A. Connor and H. I. Karunadasa, *Chem. Rev.*, 2019, **119**, 3104–3139.
- M. Saliba, *Adv. Energy Mater.*, 2019, **9**, 1803754.
- M. D. Smith, E. J. Crace, A. Jaffe and H. I. Karunadasa, *Annu. Rev. Mater. Res.*, 2018, **48**, 111–136.
- S. Tao, I. Schmidt, G. Brocks, J. Jiang, I. Tranca, K. Meerholz and S. Olthof, *Nat. Commun.*, 2019, **10**, 2560.
- C. Katan, N. Mercier and J. Even, *Chem. Rev.*, 2019, **119**, 3140–3192.
- T. Ishihara, X. Hong, J. Ding and A. V. Nurmikko, *Surf. Sci.*, 1992, **267**, 323–326.
- X. Hong, T. Ishihara and A. V. Nurmikko, *Phys. Rev. B: Condens. Matter Mater. Phys.*, 1992, **45**, 6961–6964.
- G. Kieslich, S. Sun and A. K. Cheetham, *Chem. Sci.*, 2015, **6**, 3430–3433.
- S. Ahmad, C. Hanmandlu, P. K. Kanaujia and G. V. Prakash, *Opt. Mater. Express*, 2014, **4**, 1313.
- A. Raja, A. Chaves, J. Yu, G. Arefe, H. M. Hill, A. F. Rigosi, T. C. Berkelbach, P. Nagler, C. Schüller, T. Korn, C. Nuckolls, J. Hone, L. E. Brus, T. F. Heinz, D. R. Reichman and A. Chernikov, *Nat. Commun.*, 2017, **8**, 15251.
- D. B. Straus and C. R. Kagan, *J. Phys. Chem. Lett.*, 2018, **9**, 1434–1447.
- M. C. Gélvez-Rueda, E. M. Hutter, D. H. Cao, N. Renaud, C. C. Stoumpos, J. T. Hupp, T. J. Savenije, M. G. Kanatzidis and F. C. Grozema, *J. Phys. Chem. C*, 2017, **121**, 26566–26574.
- M. Era, S. Morimoto, T. Tsutsui and S. Saito, *Appl. Phys. Lett.*, 1994, **65**, 676–678.
- K. Chondroudis and D. B. Mitzi, *Chem. Mater.*, 1999, **11**, 3028–3030.
- C. R. Kagan, D. B. Mitzi and C. D. Dimitrakopoulos, *Science*, 1999, **286**, 945–947.
- Y. Liu, H. Ye, Y. Zhang, K. Zhao, Z. Yang, Y. Yuan, H. Wu, G. Zhao, Z. Yang, J. Tang, Z. Xu and S. (Frank) Liu, *Matter*, 2019, **1**, 465–480.
- Y. Zhang, Y. Liu, Z. Xu, H. Ye, Q. Li, M. Hu, Z. Yang and S. (Frank) Liu, *J. Mater. Chem. C*, 2019, **7**, 1584–1591.
- I. C. Smith, E. T. Hoke, D. Solis-Ibarra, M. D. McGehee and H. I. Karunadasa, *Angew. Chem.*, 2014, **126**, 11414–11417.
- G. Grancini, C. Roldán-Carmona, I. Zimmermann, E. Mosconi, X. Lee, D. Martineau, S. Narbey, F. Oswald, F. De Angelis, M. Graetzel and M. K. Nazeeruddin, *Nat. Commun.*, 2017, **8**, 15684.
- X. Zhu, D. Yang, R. Yang, B. Yang, Z. Yang, X. Ren, J. Zhang, J. Niu, J. Feng and S. (Frank) Liu, *Nanoscale*, 2017, **9**, 12316–12323.
- M. Era, T. Hattori, T. Taira and T. Tsutsui, *Chem. Mater.*, 1997, **9**, 8–10.
- K. M. Chiang, B. W. Hsu, Y. A. Chang, L. Yang, W. L. Tsai and H. W. Lin, *ACS Appl. Mater. Interfaces*, 2017, **9**, 40516–40522.
- D. B. Mitzi, M. T. Prikas and K. Chondroudis, *Chem. Mater.*, 1999, **11**, 542–544.
- Z. Zheng, H. Lan, Z. Su, H. Peng and J. Luo, *Sci. Rep.*, 2019, 1–9.
- J. Ávila, C. Momblona, P. P. Boix, M. Sessolo and H. J. Bolink, *Joule*, 2017, **1**, 431–442.
- R. C. Shallock, S. Olthof, K. Meerholz and N. R. Armstrong, *ACS Appl. Mater. Interfaces*, 2019, **11**, 32500–32508.
- K. Du, Q. Tu, X. Zhang, Q. Han, J. Liu, S. Zauscher and D. B. Mitzi, *Inorg. Chem.*, 2017, **56**, 9291–9302.
- D. B. Mitzi, *Synthesis, Structure, and Properties of Organic-Inorganic Perovskites and Related Materials*, 1994.

- 31 G. C. Papavassiliou, G. A. Mousdis, C. P. Raptopoulou and A. Terzis, *Z. Naturforsch., B: J. Chem. Sci.*, 1999, **54**, 1405–1409.
- 32 K. Shibuya, M. Koshimizu, F. Nishikido, H. Saito and S. Kishimoto, *Acta Crystallogr., Sect. E: Struct. Rep. Online*, 2009, **65**, m1323-4.
- 33 D. Mitzi, *J. Solid State Chem.*, 1999, **145**, 694–704.
- 34 C. C. Stoumpos, D. H. Cao, D. J. Clark, J. Young, J. M. Rondinelli, J. I. Jang, J. T. Hupp and M. G. Kanatzidis, *Chem. Mater.*, 2016, **28**, 2852–2867.
- 35 G. Longo, C. Momblona, M.-G. La-Placa, L. Gil-Escrig, M. Sessolo and H. J. Bolink, *ACS Energy Lett.*, 2018, **3**, 214–219.
- 36 G. P. Nagabhushana, R. Shivaramaiah and A. Navrotsky, *Proc. Natl. Acad. Sci. U. S. A.*, 2016, **113**, 7717–7721.
- 37 I. L. Ivanov, A. S. Steparuk, M. S. Bolyachkina, D. S. Tsvetkov, A. P. Safronov and A. Y. Zuev, *J. Chem. Thermodyn.*, 2018, **116**, 253–258.
- 38 Y. Gao, M. Zhang, X. Zhang and G. Lu, *J. Phys. Chem. Lett.*, 2019, **10**, 3820–3827.

Vacuum-Deposited 2D/3D Perovskite Heterojunctions

Maria-Grazia La-Placa,[†] Lidón Gil-Escrig,[‡] Dengyang Guo,^{||} Francisco Palazon,[†] Tom J. Savenije,^{||} Michele Sessolo,^{*,†} and Henk J. Bolink[†]

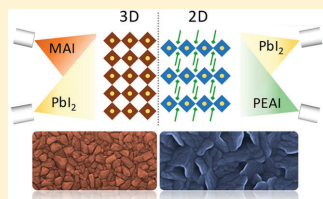
[†]Instituto de Ciencia Molecular, Universidad de Valencia, C/Beltrán 2, Paterna 46980, Spain

[‡]Helmholtz-Zentrum Berlin für Materialien und Energie GmbH, Young Investigator Group for Perovskite Tandem Solar Cells, Kekuléstraße 5, Berlin 12489, Germany

^{||}Department of Chemical Engineering, Delft University of Technology, Delft 2629 HZ, The Netherlands

Supporting Information

ABSTRACT: Low-dimensional (quasi-) 2D perovskites are being extensively studied in order to enhance the stability and the open-circuit voltage of perovskite solar cells. Up to now, thin 2D perovskite layers on the surface and/or at the grain boundaries of 3D perovskites have been deposited solely by solution processing, leading to unavoidable intermixing between the two phases. In this work, we report the fabrication of 2D/3D/2D perovskite heterostructures by dual-source vacuum deposition, with the aim of studying the interaction between the 3D and 2D phases as well as the charge transport properties of 2D perovskites in neat 2D/3D interfaces. Unlike what is normally observed in solution-processed 3D/2D systems, we found a reduced charge transport with no direct evidence of surface passivation, in spite of larger open-circuit voltage. This is likely due to a nonfavorable orientation of the 2D perovskite with respect to methylammonium lead iodide and to the formation of 2D phases with very low dimensionality (pure 2D).



Organic–inorganic metal halide perovskites are being widely studied because of their exceptional optoelectronics properties, among others a high absorption coefficient, ambipolar charge transport, and easy-to-tune bandgap.^{1–3} Importantly, high-quality perovskite films can be deposited through a variety of scalable methods, either from solution or in vacuum, and assembled into optoelectronic thin-film devices.^{4,5} These properties lead to the demonstration of perovskite solar cells (PSCs) with certified power conversion efficiency (PCE) of 25% in only 10 years of development.⁶ The most widely studied perovskite compositions, such as methylammonium lead iodide (CH₃NH₃PbI₃, MAPI), are based on the three-dimensional (3D) AMX₃ structure, where A represents a monovalent organic or inorganic cation, typically methylammonium (MA), formamidinium (FA), or cesium (Cs⁺), M is a divalent metal cation (Pb²⁺ or Sn²⁺) and X is a halide (Cl⁻, Br⁻, I⁻).^{7–10} Polycrystalline perovskite thin films used in high-efficiency PSCs still contain defects, notably at the surface, which limits the device performance as a consequence of nonradiative charge recombination.^{11,12} Defects on the surface and on the grain boundaries also play an important role in the permeation of moisture or oxygen into the perovskite film, accelerating the film/device degradation. Several methods have been reported to simultaneously passivate and enhance the stability of perovskites,¹³ most notably the use of additive, alternative precursors, or altered

stoichiometry,^{14–16} embedding small alkali metal cations,^{17–19} or the use of thin organic buffer layers at the perovskite/transport material interface.^{20–23}

More recently, several works reported on mixed-dimensional perovskites, using monoammonium or diammonium cations, which interact with the 3D perovskite, not only passivating surface defects but also improving the device stability, thanks to the hydrophobic character of the alkylammonium chains.^{24,25} The structural analysis of modified 3D perovskite films suggested the coexistence of two distinct phases: a 3D perovskite layer and a 2D (layered) perovskite. 2D perovskites form when the inorganic lead halide framework cannot accommodate the large organic cations into a 3D structure and collapses into a low-dimensional material with inorganic sheets separated by the organic cations. The general formula for pure 2D perovskites is (R-NH₃)₂MX₄, where R is an aliphatic or aromatic group. The layered perovskite family is not restricted solely to this structure, and thicker inorganic sheets can be incorporated as well. In the Ruddlesden–Popper layered perovskites with formula (RNH₃)₂(A)_{n-1}PbI_{3n+1}, the thickness of the inorganic layers increases with increasing *n*.²⁶ The properties of this last class of materials, also known as

Received: October 11, 2019

Accepted: November 5, 2019

Published: November 5, 2019

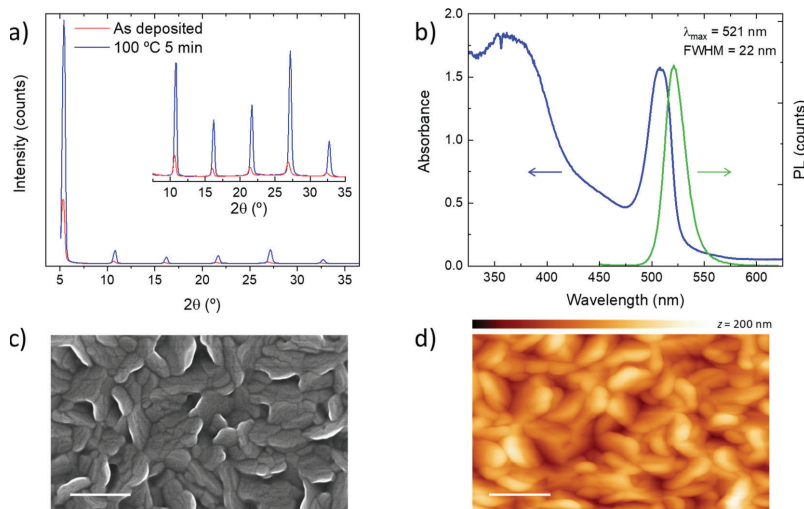


Figure 1. (a) XRD patterns of 200 nm thick, vacuum-deposited PEA_2PbI_4 perovskite thin films. (b) Optical absorption and photoluminescence spectra (excitation at 375 nm), (c) SEM image, and (d) AFM topography of PEA_2PbI_4 thin films after annealing at 100 °C for 5 min. The scale bar in both microscopy images is 400 nm.

quasi-2D perovskites, have been widely studied.^{27,28} It was shown that solar cells with $n < 40$ show inferior performance as a consequence of a reduced charge carrier mobility.^{29,30} Ruddlesden–Popper perovskites have been applied to light-emitting diodes and solar cells, showing good charge transport properties and enhanced photovoltage and stability.^{29,31–40}

A complementary approach involves the use of 2D–3D bilayers. The underlying concept is to combine the high efficiency of the 3D absorber with the stabilization and passivation properties of 2D perovskites.⁴¹ These bilayers can be prepared by functionalization of the 3D perovskite surface with large ammonium cations, resulting in the formation of thin low-dimensional perovskite layers.^{42–49} Alternatively, the direct processing of a 2D perovskite film on top of a preformed 3D material can also be beneficial for the bottom perovskite film.^{50,51} Up to now, the introduction of thin 2D perovskite layers on the surface and/or at the grain boundaries of 3D perovskite has been carried out solely by solution processing, leading to unavoidable intermixing between the 2D and 3D perovskites, with the formation of an intermediate, low-dimensional quasi-2D layer.⁵² Vacuum deposition is an alternative solvent-free technique suited to develop multilayer perovskite structures.⁵³ Vacuum processing of perovskites is intrinsically additive, eliminating issues such as the solubility limitation of precursors or the need for orthogonal solvents in order to process multilayer devices.^{54,55} At the same time, it allows a fine control over the film thickness and the deposition of high-purity semiconductors.^{56,57} Recently, a 3D/2D heterojunction produced exclusively by vacuum methods has been reported.⁵⁸ The heterojunction consists of a MAPI film (formed by conversion of a sublimed PbI_2 layer converted with MAI vapors), subsequently exposed to butylammonium iodide vapors, forming a surface layer of the quasi-2D perovskite $(\text{BA})_2(\text{MA})_{n-1}\text{Pb}_n\text{I}_{3n+1}$, with $n \approx 3$. While an increase in stability was found for the surface-modified solar cells, the

performance and especially the photovoltage were not found to improve as compared to the reference MAPI devices.

In this work, we report the fabrication of 2D/3D perovskite heterojunctions by dual-source vacuum deposition, with the aim of studying the interaction between the 3D and 2D phases as well as the charge transport properties of 2D perovskites in neat 2D/3D interfaces. We prepared 2D/MAPI/2D perovskite heterostructures by employing pure MAPI (3D) and pure phenethylammonium lead iodide (PEA_2PbI_4 , 2D). These structures were integrated into vacuum-deposited PSCs. In order to rationalize the role of each interface, we also separately studied the two possible bilayer configurations, 2D/MAPI and MAPI/2D. Unlike what was observed in solution-processed 3D/2D films, we observed generally hindered charge transport with no direct evidence of surface passivation. These phenomena are likely due to a nonfavorable orientation of the 2D perovskite with respect to the MAPI (growth parallel to the substrate and impeding charge transport) and to the formation of 2D phases with very low dimensionality (n virtually equal to 1). Despite the lower mobility and unfavorable orientation of the 2D perovskite, we identified a trade-off between the open-circuit voltage (V_{oc} , which was found to increase up to 1.1 V) and fill factor (FF, related to charge transport) as a function of the 2D layer thickness.

The 2D PEA_2PbI_4 perovskite thin films were prepared by co-sublimation of the precursor compounds, phenethylammonium iodide (PEAI) and lead iodide, upon calibration of the deposition rate for each material. The calibration factor was obtained by comparing the thickness of the thin film detected from the quartz crystal microbalance sensors with that measured with a mechanical profilometer. PEAi can be sublimed with a stable and controlled deposition rate; however, it must be properly outgassed in high vacuum before deposition. Details of the thin-film and device fabrication are

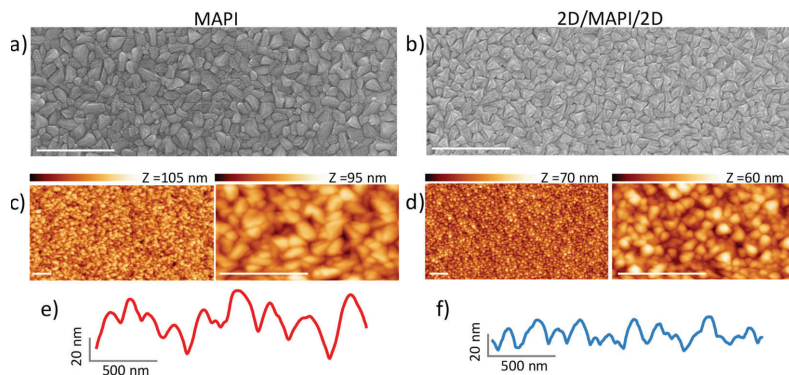


Figure 2. SEM pictures and AFM topographies at different magnifications of (a,c) a MAPI film and of (b,d) a 2D/MAPI/2D heterostructure. (e,f) AFM profiles for the same samples. The scale bar in all SEM and AFM images is 1 μm .

provided in the Supporting Information. Estimation of layered PEA_2PbI_4 perovskite stoichiometry was performed offline with X-ray diffraction (XRD). The diffractograms (Figure 1a) were collected for both the pristine samples and low-temperature annealed films (5 min at 100 $^\circ\text{C}$ in an inert atmosphere). The as-prepared materials already show the expected XRD pattern for a 2D perovskite, meaning that crystallization occurs already at room temperature, as for vacuum-deposited MAPI films.

However, after the short low-temperature annealing, we observed more intense diffraction peaks, indicating a well-crystallized perovskite. The c -axis diffraction signals strongly dominate the diffraction pattern, with six observed [001] peaks (5.4° , 10.8° , 16.3° , 21.7° , 27.2° , 32.8°) corresponding to the (002), (004), (006), (008), (0010), and (0012) crystal planes, respectively. The preferential orientation along the [001] direction suggests that the 2D perovskite film grows with the alternating organic and inorganic sheets parallel to the substrate's plane. Such an orientation is not a priori favorable for device operation as the insulating organic sheets would be perpendicular to the direction of charge transport. The optical absorption spectrum of the PEA_2PbI_4 film (Figure 1b) exhibits the characteristic components of 2D perovskites: a band in the UV–blue range, corresponding to the interband transitions leading to free carrier generation, and a red-shifted intense peak at 508 nm due to exciton absorption.⁵⁹ The corresponding photoluminescence (PL), measured upon excitation with a continuous-wave laser at 375 nm) spectrum shows the expected sharp emission peak with a very small Stokes shift at 521 nm, with a full width at half-maximum (FWHM) of only 22 nm. Taken together, the XRD and the optical characteristics indicate the formation of a pure 2D ($n = 1$) perovskite compound. The morphology of the layers was studied by scanning electron microscopy (SEM, Figure 1c) and atomic force microscopy (AFM, Figure 1d). SEM shows a distinct morphology with well-defined, randomly distributed platelets (size up to 500 nm) composed of grains in the <100 nm range. These vacuum-deposited 2D materials were found to be very reproducible and could maintain stable structural properties for more than 6 months (Figure S1).

We then used these 2D films to fabricate perovskite heterostructures. Initially, we deposited 10 nm thick PEA_2PbI_4 films below and on top of a 500 nm thick MAPI film in order

to investigate the influence of the 2D layers on the morphology and crystallinity of the 3D perovskite. The XRD patterns of a 3D sample on glass and sandwiched between 2D layers are presented in Figure S2. As can be observed for the reference sample (MAPI on glass), a preferential orientation occurs along the [110] direction, as commonly observed for both solution-processed and vacuum-deposited MAPI.^{60,61} However, when the MAPI layer is sandwiched between two PEA_2PbI_4 films, we observe a decrease in the intensity of the (110) and (220) peaks along with an increase of the (022) and (134) reflections. These observations suggest a change in the orientation of the MAPI film when deposited between 2D perovskites. The change of the diffraction profiles together with their enlarged FWHM also indicates a reduction of the crystal size for the MAPI film. We also noted a weak diffraction signal at low angle ($2\theta = 12.7^\circ$), ascribed to the presence of unreacted PbI_2 , both in the pure MAPI and in the 2D/MAPI/2D heterostructure. The role of a small PbI_2 excess in MAPI films has been widely studied, but its effect has not been fully rationalized yet. Specifically, in vacuum-deposited MAPI films and solar cells, the presence of resilient PbI_2 has been often identified, and it seems not to interfere with charge generation and transport.^{62,63} Interestingly, in several solution-processed 3D/2D perovskite systems, excess PbI_2 is intentionally used as a platform to then form a low-dimensional perovskite by simply spin-coating the corresponding organic ammonium halide.⁴¹ In our case, the excess PbI_2 in the MAPI film is maintained even after deposition of the 2D PEA_2PbI_4 film. Considering that no PbI_2 diffraction could be observed in pure PEA_2PbI_4 films (meaning that the PbI_2 signal comes only from the underlying MAPI layer), these observations suggest that no intermixing takes place between the two materials, resulting in a neat 3D/2D perovskite interface. The formation of a pure PEA_2PbI_4 film at the interface with MAPI is also supported by the PL of a 2D/3D bilayer, where the signals correspond to those of the pure separated materials (Figure S7).

While no changes were observed in the optical absorption of the 2D/MAPI/2D heterostructure (Figure S3) as compared to the bare MAPI (the contribution of the very thin PEA_2PbI_4 films is not noticeable because the 3D absorption saturates in the green–blue region of the spectrum), we did observe differences in their morphology. The morphology of the 3D

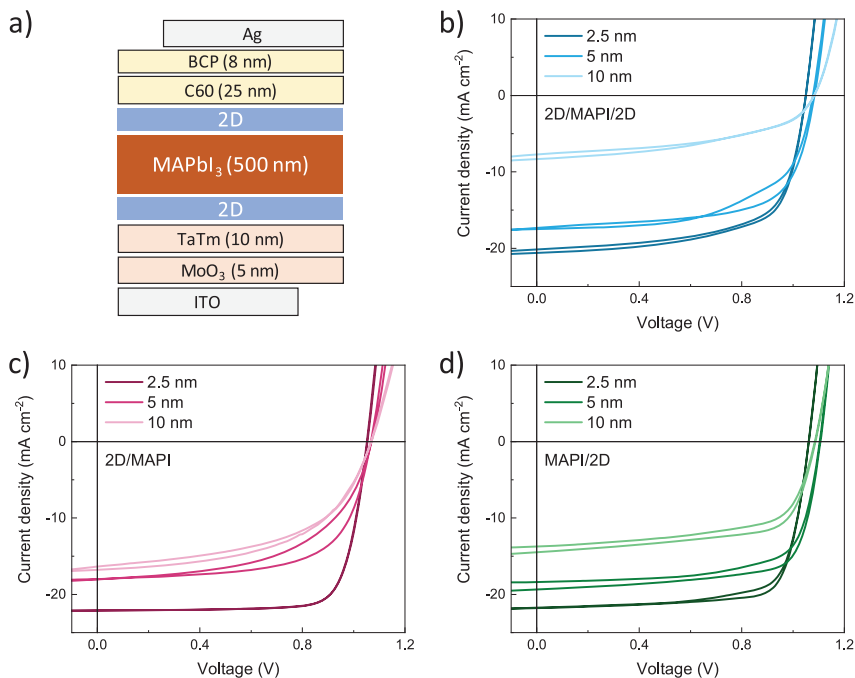


Figure 3. (a) Schematics of the p-i-n solar cells employing a perovskite heterostructure as the active layer. J - V curve under 100 mW cm^{-2} illumination of the (b) 2D/MAPI/2D, (c) 2D/MAPI, and (d) MAPI/2D heterojunction solar cells for different PEA₂PbI₄ layer thicknesses.

layer with and without the 2D perovskite interlayers was investigated by SEM. The surface of the MAPI film appears homogeneous and compact (Figure 2a), composed of grains with an average size of approximately 100 nm.

In the 2D/MAPI/2D heterostructure (Figure 2b), we can already observe how the PEA₂PbI₄ layer affects the film growth and morphology as the grain size is reduced, and the surface seems more textured as compared to the bare MAPI film.^{64,65} These effects correlate with the XRD discussed before (Figure S2). The surface of the samples was further analyzed by AFM. While homogeneous on a large scale (Figure 2c), the MAPI film surface was found to be rather rough, with a root-mean-square roughness R_{RMS} of 13 nm and average height z_{AVG} as high as 50 nm (Figures 2e and S4). The grain size reduction observed by SEM for the 2D/MAPI/2D heterostructure was also confirmed by AFM (Figure 2d), where the topography was characterized by $R_{\text{RMS}} = 8 \text{ nm}$ and a strongly diminished z_{AVG} of 27 nm (Figure 2f). At the same time, the height distribution was found also to be narrower, indicating a more homogeneous surface. Grain size reduction as a result of the interaction of a 3D perovskite with large cations has also been observed previously.^{42,66}

To evaluate the potential of a 2D/MAPI/2D perovskite heterostructure in photovoltaics, we incorporated it in fully vacuum-deposited PSCs using a p-i-n device layout (Figure 3a). The diodes were prepared on indium tin oxide (ITO), using molybdenum oxide (MoO₃, 5 nm) and N₄,N₄,N₄',N₄'-tetra([1,1'-biphenyl]-4-yl)-[1,1':4',1''-terphenyl]-4,4''-diamine (TaTm, 10 nm) as the hole transport layer (HTL) and a 500

nm thick MAPI film, fullerene (C60, 25 nm), and bathocuproine (BCP, 8 nm) as the electron transport layers (ETLs). The devices were completed with the deposition of a silver electrode (100 nm). The low-dimensional PEA₂PbI₄ films were vacuum-deposited in between the HTL/MAPI or the MAPI/ETL interfaces, varying the thickness between 2.5 and 10 nm. All layers were thermally deposited in high vacuum with a base pressure of 10^{-6} mbar. The current density-voltage (J - V) curves of PSCs were recorded under simulated AM 1.5G illumination (100 mW cm^{-2} , Figure 3), and the corresponding photovoltaic parameters are summarized in Table 1 (only for devices with 2.5 nm thick 2D films).

We initially fabricated and tested the triple layer heterojunctions of the type 2D/MAPI/2D. The heterojunction device with 2.5 nm thick 2D films showed a short-circuit current density (J_{sc}) exceeding 20 mA cm^{-2} , only slightly lower than that of the reference MAPI solar cell (Table 1 and Figure S5). While the open-circuit voltage (V_{oc}) was found to decrease only approximately 6–7 meV compared to the reference, we observed a strongly reduced FF (65.5%) even though the two 2D films were only 2.5 nm thick (Figure 3b). With increasing thickness of the low-dimensional perovskite films, the FF further decreased to 49.7%, accompanied by a drastic reduction in the current density, being as low as 8 mA cm^{-2} for 10 nm thick 2D films.

Clearly, the 2D/MAPI/2D heterojunction solar cells suffer from hindered charge extraction, a situation that becomes more severe for thicker 2D films. This is in agreement with the formation of PEA₂PbI₄ films with insulating sheets perpendic-

Table 1. PV Performance Parameters Extracted from the J - V Characteristics of p - i - n Solar Cells of the Control MAPI Absorber Device and of 2D/MAPI/2D-, 2D/MAPI-, and MAPI/2D-Based PSCs with 2.5 nm Thick PEA_2PbI_4 2D Films

perovskite structure		V_{oc} [mV]	J_{sc} [mA cm^{-2}]	FF [%]	PCE [%]
MAPI	fwd	1057	22.7	77.2	18.6
	rev	1056	22.7	78.5	18.9
2D/MAPI/2D	fwd	1050	20.1	65.5	13.9
	rev	1050	20.6	66.0	14.3
2D/MAPI	fwd	1054	22.1	78.4	18.3
	rev	1051	22.1	78.6	18.3
MAPI/2D	fwd	1062	21.7	73.5	17.0
	rev	1061	21.8	76.6	17.7

ular to the current flow, as described above. All solar cells based on the 2D/MAPI/2D heterostructure showed also hysteresis in the J - V curve when scanning in forward (from short- to open-circuit) or reverse (from open- to short-circuit) bias. However, the V_{oc} for the devices employing 5 and 10 nm thick PEA_2PbI_4 films was found to increase up to >1080 mV, meaning that the 2D films are indeed capable of reducing nonradiative recombination of the MAPI layer.

In order to rationalize the properties of the 2D/MAPI/2D heterostructure devices, we fabricated and characterized analogous solar cells based on either 2D/3D or 3D/2D bilayers as the active materials, with increasing thickness of the PEA_2PbI_4 films. The heterojunction device with the 2.5 nm thick 2D film at the front contact (2D/MAPI, Figure 3c), shows high short-circuit current density (J_{sc} , 22.1 mA cm^{-2}) and very good rectification, with a FF as high as 78.6% and negligible hysteresis. The V_{oc} is approximately 1.05 V, leading to a PCE of 18.3%, comparable to that of the reference MAPI solar cells. Increasing the thickness of PEA_2PbI_4 to 5 and 10 nm results in lower photocurrent (18 and 16.5 mA cm^{-2} , respectively) and causes again a drastic reduction of the FF, which is below 55% for both thicknesses. The cells with thicker 2D films show also hysteresis in the J - V curve. However, when compared to bare MAPI, the solar cell photovoltage is also found to increase to about 1070 mV for thicker 2D perovskite films.

A similar behavior was observed for the solar cells based on the MAPI/2D heterojunction (Figure 3d), where the PEA_2PbI_4 is now deposited on top of MAPI, below the C60 ETL. The current density decreases with increasing thickness of the 2D perovskite films, from 21.8 mA cm^{-2} (2.5 nm) to approximately 14 mA cm^{-2} (10 nm). The J - V curves for devices including thicker (5 and 10 nm) 2D films show hysteresis, with slightly larger current densities (approximately 1 mA cm^{-2}) in reverse bias. Also for MAPI/2D heterojunction, the FF was observed to scale inversely with the thickness of PEA_2PbI_4 but not as drastically as in the case of 2D/MAPI structures. The FF decreases from 73.5% to 63.9% when the 2D layer thickness is increased from 2.5 nm to 10 nm. Importantly, with this device configuration, we do observe a substantial increase in the photovoltage, with the MAPI/2D solar cells having a V_{oc} exceeding 1.1 V for 5 nm thick PEA_2PbI_4 layers. This observation indicates that the 2D perovskite layer is indeed capable of reducing the nonradiative recombination within the MAPI film. Interestingly, the fact that no changes in photovoltage were observed with the 2D/MAPI heterojunction (as compared to bare MAPI) might indicate that the interface chemistry of the 2D/3D interface differs from that of the MAPI/2D one.

Figure 4 summarizes the thickness-dependent photovoltage and FF measured on the different heterojunction solar cells. In general, we observe a trend where 2.5 nm thick films of PEA_2PbI_4 , independent of the side where the MAPI's are deposited, do not lead to an appreciable increase in the photovoltage (for MAPI cells it is 1055 mV), while they already undermine the charge extraction as the FF diminishes (Figure 3b). One exception is the 2D/3D heterojunction, where the V_{oc} and FF are essentially unchanged with respect to the reference MAPI solar cells, leading to similar PCE exceeding 18%.

Increasing the 2D layer thickness to 5 nm leads to a general enhancement of the V_{oc} with the devices based on the 2D/3D and 2D/3D/2D structures reaching 1070 and 1084 mV, respectively, and a peak for the 3D/2D heterojunction solar cells at 1104 mV. While such a 50 mV increase in V_{oc} might appear moderate, it corresponds to a 7-fold enhancement of the external PL quantum yield.^{67,68} We note that devices with different thicknesses of the 2D films show comparable dark leakage currents, indicating that the observed changes of voltage have no direct electrical origin (Figure S8). Hence, the

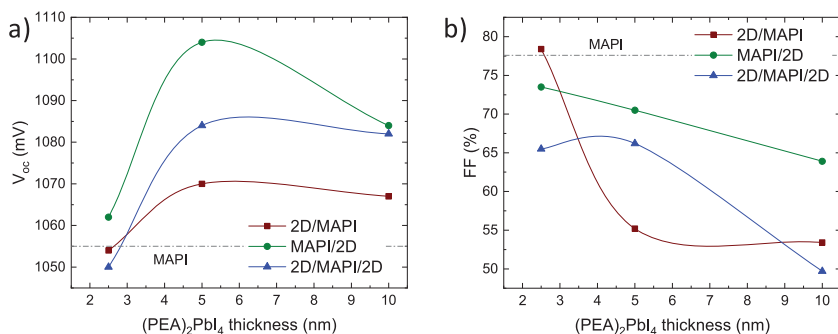


Figure 4. Trend of the (a) V_{oc} and (b) FF for the three different heterojunction solar cells as a function of the 2D perovskite (PEA_2PbI_4) layer thickness. The dotted lines represent average values for single-layer MAPI devices.

vacuum-deposited PEA_2PbI_4 films on top of MAPI are indeed capable of reducing nonradiative charge recombination, although at the expense of the FF (70%). For thicker (10 nm) 2D films, we observed a reduction of the V_{oc} , which is more prominent for the 3D/2D heterojunction with a 10 nm thick film. Although the incorporation of 2D perovskites at the interface with MAPI is beneficial in terms of photovoltage, it leads to a drop in FF, which became more important once the PEA_2PbI_4 thickness increased from 5 and 10 nm (Figure 3b). The loss in FF can be attributed to the unfavorable orientation of the insulating sheets formed by the bulky organic cations within the 2D perovskite films (Figure 1), perpendicularly oriented to the direction of the charge transport.

Besides the orientation of the 2D perovskite with respect to the substrate, another factor that can contribute to the loss in FF is the presence of an energy barrier for the charge extraction (either hole or electron, or both) at the 3D/2D heterojunction or at the perovskite/organic interfaces. Such an energy barrier is related to misalignment of the energy levels, which is likely to exist at least in one case (either 2D/3D or 3D/2D) as a consequence of the larger bandgap of PEA_2PbI_4 as compared to that of MAPI. The ionization energy (IE) can be used to estimate the valence band maximum (VBM) in an intrinsic semiconductor. We measured via air photoemission spectroscopy the IE of both 3D and 2D perovskites (Figure S6). We found an IE for MAPI of 5.0 eV, only slightly smaller as compared to recently reported ultraviolet photoemission spectroscopy measurements,⁶⁹ while a larger IE of 5.5 eV was measured for PEA_2PbI_4 films. This implies the presence of an energy barrier for the hole extraction of approximately 0.5 eV, which supports the severe drop in FF observed when PEA_2PbI_4 is deposited in between the HTL and the MAPI (Figure 3b). Estimating the bandgap of PEA_2PbI_4 from the absorption spectrum (2.4 eV) and considering a MAPI bandgap of 1.6 eV,⁶⁹ the barrier for the electron extraction at the 3D/2D interface would be 0.3 eV (Figure S6). The lower energy difference among the electronic affinities at the 3D/2D interface agrees with the smaller FF losses associated with using the 2D perovskite on top of the MAPI surface and below the ETL.

The vacuum-deposited 2D/3D heterostructures were further studied by means of time-resolved microwave conductivity (TRMC). Figure 5a depicts the normalized time-dependent conductance traces for bare MAPI and 2D/MAPI bilayers, obtained by selectively and homogeneously exciting the 3D MAPI film at 600 nm from both sides. Due to the lack of optical absorption at this wavelength, we did not observe any appreciable signal from the 2D layer. After a fast initial rise limited by the response time of the microwave cavity, the signals decayed due to charge recombination or trapping. Interestingly, the decay kinetics of the MAPI and 2D/MAPI are very similar and independent of the excitation side and the presence of the 2D layer. Hence, from this measurement, we cannot conclude that the MAPI film is effectively passivated by the 2D layer.

From the maximum change in photoconductance, ΔG_{\max} , the product of charge carrier generation efficiency per incident photon, η , and the sum of electron and hole mobility, $\sum \mu$ is calculated using

$$\eta \sum \mu = \frac{\Delta G_{\max}}{I_0 e \beta} \quad (1)$$

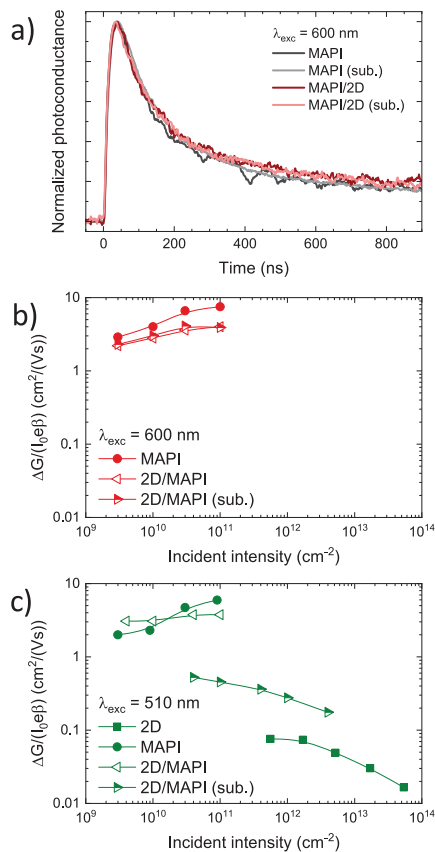


Figure 5. (a) Normalized change in conductance for a MAPI film and a 2D/MAPI bilayer deposited on quartz, measured by TRMC with an incident laser pulse of 10^{11} photons/cm². Maximum TRMC signal heights expressed in charge carrier yield times mobility for excitation at (b) 600 and (c) 510 nm. The annotation (sub.) denotes that the light is shined through the quartz substrate.

where I_0 is the incident intensity, e is the elementary charge, and β is a geometrical factor. For both the 3D film as well as the 3D/2D bilayer, the $\eta \sum \mu$ values increase slightly with light intensity, reaching values close to 10 cm²/(Vs), which is comparable to values previously reported and discussed on evaporated 3D perovskite layers.^{70,71} The slight difference in maximum mobility can be related to the different substrate on which the 3D MAPI layer has been deposited. Importantly, the dependence of the MAPI film with intensity is larger than that of the 2D/MAPI bilayers, which is almost constant (Figure 5b). Such dependence can be explained by the fact that the 3D film contains a substantial amount of deep traps, which become saturated at higher intensities.⁷² This observation agrees with the higher V_{oc} values observed for the heterostructure devices (Figure 4a). Finally, we excited the samples at 510 nm, which corresponds with the maximum absorption of the excitonic band of the 2D perovskite (see

Figure 5c). The 2D layer exhibited very low signal, which can be explained by the high exciton binding energy preventing dissociation of the excitons into mobile carriers.⁷³ The MAPI films as well as the 3D/2D bilayer gave signal intensities comparable to that of excitation at 600 nm, implying that the charge carrier yield is independent of the used wavelengths. Interestingly, exciting the 2D/MAPI sample through the 2D layer leads to a substantial decrease of the signal intensity. This can be explained by the fact that a substantial part of the incident light is absorbed by the 2D perovskite itself, and the excited states generated in the 2D layer do not lead to mobile carriers in the MAPI film by either charge or energy transfer. This inefficient charge carrier generation might partially explain the photocurrent losses observed in the heterostructure devices (Figure 3).

In summary, we show for the first time the fabrication of perovskite heterostructures by dual-source vacuum deposition. This was achieved by vacuum processing thin layers of the 2D perovskite phenethylammonium lead iodide (PEA₂PbI₄) below and on top of a vacuum-deposited methylammonium lead iodide (MAPI) film. We investigated the morphology, structure, and optical properties of the 2D and 3D separately, as well as of the 2D/3D/2D heterostructure, and observed that vacuum-deposited PEA₂PbI₄ films tend to grow with the alternating inorganic and organic sheets parallel to the substrate. For this reason, when incorporated into devices, the 2D/3D/2D perovskite heterostructure shows a strongly hindered charge extraction, a result of an interplay of parameters among the preferential in-plane orientation of the 2D film, the low carrier mobility, and the mismatch in the transport energy levels. By separately studying the 2D/3D and 3D/2D bilayers, we identified a trade-off between the solar cell photovoltage and FF, with 3D/2D heterojunction solar cells having open-circuit voltage as high as 1.1 V. By TRMC, we observed that the density of deep traps in the MAPI active layers is reduced in the presence of the 2D perovskite; however, the latter leads to a reduced photocurrent as we did not observe any charge or energy transfer from the 2D film to the MAPI. In general, our results show a marked difference between vacuum-deposited and solution-processed 3D/2D architectures, with unfavorable orientation but high phase purity obtained by dual-source vapor deposition. Future work will address the vacuum deposition of vertically oriented 2D perovskite films in order to promote charge transport and will focus on their role on the overall device stability.

■ ASSOCIATED CONTENT

■ Supporting Information

The Supporting Information is available free of charge on the ACS Publications website at DOI: 10.1021/acsenergylett.9b02224.

Experimental methods, XRD patterns of PEA₂PbI₄ measured as prepared and after 6 months, XRD patterns of 3D perovskite and the (2D/3D/2D) heterostructure, absorption spectra and roughness analysis of 3D perovskite and the (2D/3D/2D) perovskite heterostructure, *J*–*V* curves of the ref 3 MAPI solar cell and of 2D/3D, 3D/2D, and 2D/3D/2D heterojunction devices with 2.5 nm PEA₂PbI₄, APS of 3D and 2D thin films, and flat band energy diagram with ionization energies and electron affinity (PDF)

■ AUTHOR INFORMATION

Corresponding Author

*E-mail: michele.sessolo@uv.es.

ORCID

Francisco Palazon: 0000-0002-1503-5965

Tom J. Savenije: 0000-0003-1435-9885

Michele Sessolo: 0000-0002-9189-3005

Henk J. Bolink: 0000-0001-9784-6253

Notes

The authors declare no competing financial interest.

■ ACKNOWLEDGMENTS

The research leading to these results received funding from the European Union Programme for Research and Innovation Horizon 2020 (2014–2020) under the Marie Skłodowska-Curie Grant Agreement PerovSAMS No. 747599 and the Spanish Ministry of Economy and Competitiveness (MINECO) via the Unidad de Excelencia Maria de Maeztu MDM-2015-0538, MAT2017-88821-R, RTI2018-095362-A-I00, PCIN-2015-255, and PCIN-2017-014 and the Generalitat Valenciana (Prometeo/2016/135). M.S. acknowledges the MINECO for his RyCcontract. D.G acknowledges funding from the China Scholarship Council (CSC).

■ REFERENCES

- (1) Li, W.; Wang, Z.; Deschler, F.; Gao, S.; Friend, R. H.; Cheetham, A. K. Chemically Diverse and Multifunctional Hybrid Organic–Inorganic Perovskites. *Nat. Rev. Mater.* **2017**, *2* (3), 16099.
- (2) Huang, J.; Yuan, Y.; Shao, Y.; Yan, Y. Understanding the Physical Properties of Hybrid Perovskites for Photovoltaic Applications. *Nat. Rev. Mater.* **2017**, *2* (7), 17042.
- (3) Brenner, T. M.; Egger, D. A.; Kronik, L.; Hodes, G.; Cahen, D. Hybrid Organic–Inorganic Perovskites: Low-Cost Semiconductors with Intriguing Charge-Transport Properties. *Nat. Rev. Mater.* **2016**, *1* (1), 15007.
- (4) Swartwout, R.; Hoerantner, M. T.; Bulović, V. Scalable Deposition Methods for Large-Area Production of Perovskite Thin Films. *Energy Environ. Mater.* **2019**, *2* (2), 119–143.
- (5) Li, Z.; Klein, T. R.; Kim, D. H.; Yang, M.; Berry, J. J.; van Hest, M. F. A. M.; Zhu, K. Scalable Fabrication of Perovskite Solar Cells. *Nat. Rev. Mater.* **2018**, *3* (4), 18017.
- (6) Green, M. A.; Dunlop, E. D.; Levi, D. H.; Hohl-Ebinger, J.; Yoshita, M.; Ho-Baillie, A. W. Y. Solar Cell Efficiency Tables (Version 54). *Prog. Photovoltaics* **2019**, *27* (7), 565–575.
- (7) Saliba, M. Polyelemental, Multicomponent Perovskite Semiconductor Libraries through Combinatorial Screening. *Adv. Energy Mater.* **2019**, *9* (25), 1803754.
- (8) Zhao, Y.; Zhu, K. Organic–Inorganic Hybrid Lead Halide Perovskites for Optoelectronic and Electronic Applications. *Chem. Soc. Rev.* **2016**, *45* (3), 655–689.
- (9) Stoumpos, C. C.; Kanatzidis, M. G. Halide Perovskites: Poor Man's High-Performance Semiconductors. *Adv. Mater.* **2016**, *28* (28), 5778–5793.
- (10) Zhao, D.; Yu, Y.; Wang, C.; Liao, W.; Shrestha, N.; Grice, C. R.; Cimaroli, A. J.; Guan, L.; Ellingson, R. J.; Zhu, K.; et al. Low-Bandgap Mixed Tin–Lead Iodide Perovskite Absorbers with Long Carrier Lifetimes for All-Perovskite Tandem Solar Cells. *Nat. Energy* **2017**, *2* (4), 17018.
- (11) Wang, J.; Fu, W.; Jariwala, S.; Sinha, L.; Jen, A. K.-Y.; Ginger, D. S. Reducing Surface Recombination Velocities at the Electrical Contacts Will Improve Perovskite Photovoltaics. *ACS Energy Lett.* **2019**, *4*, 222.
- (12) Ball, J. M.; Petrozza, A. Defects in Perovskite-Halides and Their Effects in Solar Cells. *Nat. Energy* **2016**, *1* (11), 16149.

- (13) Aydin, E.; Bastiani, M.; Wolf, S. Defect and Contact Passivation for Perovskite Solar Cells. *Adv. Mater.* **2019**, *31*, 1900428.
- (14) Wang, L.; McCleese, C.; Kovalsky, A.; Zhao, Y.; Burda, C. Femtosecond Time-Resolved Transient Absorption Spectroscopy of $\text{CH}_3\text{NH}_3\text{PbI}_3$ Perovskite Films: Evidence for Passivation Effect of PbI_2 . *J. Am. Chem. Soc.* **2014**, *136* (35), 12205–12208.
- (15) Chen, Q.; Zhou, H.; Song, T.-B.; Luo, S.; Hong, Z.; Duan, H.-S.; Dou, L.; Liu, Y.; Yang, Y. Controllable Self-Induced Passivation of Hybrid Lead Iodide Perovskites toward High Performance Solar Cells. *Nano Lett.* **2014**, *14* (7), 4158–4163.
- (16) Qiu, W.; Merckx, T.; Jaysankar, M.; Masse de la Huerta, C.; Rakocevic, L.; Zhang, W.; Paetzold, U. W.; Gehlhaar, R.; Froyen, L.; Poortmans, J.; et al. Pinhole-Free Perovskite Films for Efficient Solar Modules. *Energy Environ. Sci.* **2016**, *9* (2), 484–489.
- (17) Li, N.; Tao, S.; Chen, Y.; Niu, X.; Onwudinanti, C. K.; Hu, C.; Qiu, Z.; Xu, Z.; Zheng, G.; Wang, L.; et al. Cation and Anion Immobilization through Chemical Bonding Enhancement with Fluorides for Stable Halide Perovskite Solar Cells. *Nat. Energy* **2019**, *4* (5), 408–415.
- (18) Abdi-Jalebi, M.; Andaji-Garmaroudi, Z.; Cacovich, S.; Stavrakas, C.; Philippe, B.; Richter, J. M.; Alarsi, M.; Booker, E. P.; Hutter, E. M.; Pearson, A. J.; et al. Maximizing and Stabilizing Luminescence from Halide Perovskites with Potassium Passivation. *Nature* **2018**, *555* (7697), 497–501.
- (19) Saliba, M.; Matsui, T.; Domanski, K.; Seo, J.-Y.; Ummadisingu, A.; Zakeeruddin, S. M.; Correa-Baena, J.-P.; Tress, W. R.; Abate, A.; Hagfeldt, A.; et al. Incorporation of Rubidium Cations into Perovskite Solar Cells Improves Photovoltaic Performance. *Science (Washington, DC, U. S.)* **2016**, *354* (6309), 206–209.
- (20) Wang, Q.; Dong, Q.; Li, T.; Gruverman, A.; Huang, J. Thin Insulating Tunneling Contacts for Efficient and Water-Resistant Perovskite Solar Cells. *Adv. Mater.* **2016**, *28* (31), 6734–6739.
- (21) Liang, P.-W.; Chueh, C.-C.; Williams, S. T.; Jen, A. K.-Y. Roles of Fullerene-Based Interlayers in Enhancing the Performance of Organometal Perovskite Thin-Film Solar Cells. *Adv. Energy Mater.* **2015**, *5* (10), 1402321.
- (22) Shao, Y.; Xiao, Z.; Bi, C.; Yuan, Y.; Huang, J. Origin and Elimination of Photocurrent Hysteresis by Fullerene Passivation in $\text{CH}_3\text{NH}_3\text{PbI}_3$ Planar Heterojunction Solar Cells. *Nat. Commun.* **2014**, *5* (1), 5784.
- (23) Wang, K.; Neophytou, M.; Aydin, E.; Wang, M.; Laurent, T.; Harrison, G. T.; Liu, J.; Liu, W.; De Bastiani, M.; Khan, J. I. Triarylphosphine Oxide as Cathode Interfacial Material for Inverted Perovskite Solar Cells. *Adv. Mater. Interfaces* **2019**, *6*, 1900434.
- (24) Zhao, T.; Chueh, C.-C.; Chen, Q.; Rajagopal, A.; Jen, A. K.-Y. Defect Passivation of Organic–Inorganic Hybrid Perovskites by Diammonium Iodide toward High-Performance Photovoltaic Devices. *ACS Energy Lett.* **2016**, *1* (4), 757–763.
- (25) Zheng, X.; Chen, B.; Dai, J.; Fang, Y.; Bai, Y.; Lin, Y.; Wei, H.; Zeng, X. C.; Huang, J. Defect Passivation in Hybrid Perovskite Solar Cells Using Quaternary Ammonium Halide Anions and Cations. *Nat. Energy* **2017**, *2* (7), 17102.
- (26) Stoumpos, C. C.; Soe, C. M. M.; Tsai, H.; Nie, W.; Blancon, J.-C.; Cao, D. H.; Liu, F.; Traoré, B.; Katan, C.; Even, J.; et al. High Members of the 2D Ruddlesden-Popper Halide Perovskites: Synthesis, Optical Properties, and Solar Cells of $(\text{CH}_3)_3\text{NH}_3$ $2(\text{CH}_3)_2\text{NH}_3$ 4PbI_2 5I . *Chem.* **2017**, *2* (3), 427–440.
- (27) Yusoff, A. R. b. M.; Nazeeruddin, M. K. Low-Dimensional Perovskites: From Synthesis to Stability in Perovskite Solar Cells. *Adv. Energy Mater.* **2018**, *8* (26), 1702073.
- (28) Thrithamarassery Gangadharan, D.; Ma, D. Searching for Stability at Lower Dimensions: Current Trends and Future Prospects of Layered Perovskite Solar Cells. *Energy Environ. Sci.* **2019**, *12*, 2860.
- (29) Quan, L. N.; Yuan, M.; Comin, R.; Voznyy, O.; Beauregard, E. M.; Hoogland, S.; Buijn, A.; Kirmani, A. R.; Zhao, K.; Amassian, A.; et al. Ligand-Stabilized Reduced-Dimensionality Perovskites. *J. Am. Chem. Soc.* **2016**, *138* (8), 2649–2655.
- (30) Milot, R. L.; Sutton, R. J.; Eperon, G. E.; Haghighirad, A. A.; Martinez Hardigree, J.; Miranda, L.; Snaith, H. J.; Johnston, M. B.; Herz, L. M. Charge-Carrier Dynamics in 2D Hybrid Metal–Halide Perovskites. *Nano Lett.* **2016**, *16* (11), 7001–7007.
- (31) Cohen, B.-E.; Wierzbowska, M.; Etgar, L. High Efficiency and High Open Circuit Voltage in Quasi 2D Perovskite Based Solar Cells. *Adv. Funct. Mater.* **2017**, *27* (5), 1604733.
- (32) Mitzi, D. B. Solution-Processed Inorganic Semiconductors. *J. Mater. Chem.* **2004**, *14* (15), 2355.
- (33) Cao, D. H.; Stoumpos, C. C.; Farha, O. K.; Hupp, J. T.; Kanatzidis, M. G. 2D Homologous Perovskites as Light-Absorbing Materials for Solar Cell Applications. *J. Am. Chem. Soc.* **2015**, *137* (24), 7843–7850.
- (34) Koh, T. M.; Shanmugam, V.; Schlipf, J.; Oesinghaus, L.; Müller-Buschbaum, P.; Ramakrishnan, N.; Swamy, V.; Mathews, N.; Boix, P. P.; Mhaisalkar, S. G. Nanostructuring Mixed-Dimensional Perovskites: A Route Toward Tunable, Efficient Photovoltaics. *Adv. Mater.* **2016**, *28* (19), 3653–3661.
- (35) Chen, Y.; Sun, Y.; Peng, J.; Zhang, W.; Su, X.; Zheng, K.; Pullerits, T.; Liang, Z. Tailoring Organic Cation of 2D Air-Stable Organometal Halide Perovskites for Highly Efficient Planar Solar Cells. *Adv. Energy Mater.* **2017**, *7* (18), 1700162.
- (36) Ma, C.; Shen, D.; Ng, T.-W.; Lo, M.-F.; Lee, C.-S. 2D Perovskites with Short Interlayer Distance for High-Performance Solar Cell Application. *Adv. Mater.* **2018**, *30* (22), 1800710.
- (37) Jiang, W.; Ying, J.; Zhou, W.; Shen, K.; Liu, X.; Gao, X.; Guo, F.; Gao, Y.; Yang, T. A New Layered Nano Hybrid Perovskite Film with Enhanced Resistance to Moisture-Induced Degradation. *Chem. Phys. Lett.* **2016**, *658*, 71–75.
- (38) Yantara, N.; Bruno, A.; Iqbal, A.; Jamaludin, N. F.; Soci, C.; Mhaisalkar, S.; Mathews, N. Designing Efficient Energy Funneling Kinetics in Ruddlesden–Popper Perovskites for High-Performance Light-Emitting Diodes. *Adv. Mater.* **2018**, *30* (33), 1800818.
- (39) Yuan, M.; Quan, L. N.; Comin, R.; Walters, G.; Sabatini, R.; Voznyy, O.; Hoogland, S.; Zhao, Y.; Beauregard, E. M.; Kanjanaboos, P.; et al. Perovskite Energy Funnel for Efficient Light-Emitting Diodes. *Nat. Nanotechnol.* **2016**, *11*, 872.
- (40) Gharibzadeh, S.; Abdollahi Nejad, B.; Jakoby, M.; Abzieher, T.; Hauschild, D.; Moghadamzadeh, S.; Schwenzler, J. A.; Brenner, P.; Schmagier, R.; Haghighirad, A. A.; et al. Record Open-Circuit Voltage Wide-Bandgap Perovskite Solar Cells Utilizing 2D/3D Perovskite Heterostructure. *Adv. Energy Mater.* **2019**, *9* (21), 1803699.
- (41) Grancini, G.; Nazeeruddin, M. K. Dimensional Tailoring of Hybrid Perovskites for Photovoltaics. *Nat. Rev. Mater.* **2019**, *4* (1), 4–22.
- (42) Wang, Z.; Lin, Q.; Chmiel, F. P.; Sakai, N.; Herz, L. M.; Snaith, H. J. Efficient Ambient-Air-Stable Solar Cells with 2D–3D Heterostructured Butylammonium–Caesium–Formamidinium Lead Halide Perovskites. *Nat. Energy* **2017**, *2* (9), 17135.
- (43) Poli, I.; Eslava, S.; Cameron, P. Tetrabutylammonium Cations for Moisture-Resistant and Semitransparent Perovskite Solar Cells. *J. Mater. Chem. A* **2017**, *5* (42), 22325–22333.
- (44) Liu, Y.; Akin, S.; Pan, L.; Uchida, R.; Arora, N.; Milić, J. V.; Hinderhofer, A.; Schreiber, F.; Uhl, A. R.; Zakeeruddin, S. M.; et al. Ultrahydrophobic 3D/2D Fluoroarene Bilayer-Based Water-Resistant Perovskite Solar Cells with Efficiencies Exceeding 22%. *Sci. Adv.* **2019**, *5* (6), No. eaaw2543.
- (45) Ye, T.; Bruno, A.; Han, G.; Koh, T. M.; Li, J.; Jamaludin, N. F.; Soci, C.; Mhaisalkar, S. G.; Leong, W. L. Efficient and Ambient-Air-Stable Solar Cell with Highly Oriented 2D@3D Perovskites. *Adv. Funct. Mater.* **2018**, *28* (30), 1801654.
- (46) Kim, J.; Ho-Baillie, A.; Huang, S. Review of Novel Passivation Techniques for Efficient and Stable Perovskite Solar Cells. *Sol. RRL* **2019**, *3* (4), 1800302.
- (47) Lee, D. S.; Yun, J. S.; Kim, J.; Soufiani, A. M.; Chen, S.; Cho, Y.; Deng, X.; Seidel, J.; Lim, S.; Huang, S.; et al. Passivation of Grain Boundaries by Phenethylammonium in Formamidinium-Methylammonium Lead Halide Perovskite Solar Cells. *ACS Energy Lett.* **2018**, *3* (3), 647–654.
- (48) Cho, Y.; Soufiani, A. M.; Yun, J. S.; Kim, J.; Lee, D. S.; Seidel, J.; Deng, X.; Green, M. A.; Huang, S.; Ho-Baillie, A. W. Y. Mixed 3D-

2D Passivation Treatment for Mixed-Cation Lead Mixed-Halide Perovskite Solar Cells for Higher Efficiency and Better Stability. *Adv. Energy Mater.* **2018**, *8* (20), 1703392.

(49) Cho, K. T.; Grancini, G.; Lee, Y.; Oveisi, E.; Ryu, J.; Almora, O.; Tschumi, M.; Schouwink, P. A.; Seo, G.; Heo, S.; et al. Selective Growth of Layered Perovskites for Stable and Efficient Photovoltaics. *Energy Environ. Sci.* **2018**, *11* (4), 952–959.

(50) Grancini, G.; Roldán-Carmona, C.; Zimmermann, I.; Mosconi, E.; Lee, X.; Martineau, D.; Nabey, S.; Oswald, F.; De Angelis, F.; Graetzel, M.; et al. One-Year Stable Perovskite Solar Cells by 2D/3D Interface Engineering. *Nat. Commun.* **2017**, *8* (1), 15684.

(51) Cho, K. T.; Zhang, Y.; Orlandi, S.; Cavazzini, M.; Zimmermann, I.; Lesch, A.; Tabet, N.; Pozzi, G.; Grancini, G.; Nazeeruddin, M. K. Water-Repellent Low-Dimensional Fluorous Perovskite as Interfacial Coating for 20% Efficient Solar Cells. *Nano Lett.* **2018**, *18* (9), 5467–5474.

(52) Quintero-Bermudez, R.; Gold-Parker, A.; Proppe, A. H.; Munir, R.; Yang, Z.; Kelley, S. O.; Amassian, A.; Toney, M. F.; Sargent, E. H. Compositional and Orientational Control in Metal Halide Perovskites of Reduced Dimensionality. *Nat. Mater.* **2018**, *17* (10), 900–907.

(53) Ávila, J.; Momblona, C.; Boix, P. P.; Sessolo, M.; Bolink, H. J. Vapor-Deposited Perovskites: The Route to High-Performance Solar Cell Production? *Joule* **2017**, *1* (3), 431–442.

(54) Forgács, D.; Gil-Escrig, L.; Pérez-Del-Rey, D.; Momblona, C.; Werner, J.; Niesen, B.; Ballif, C.; Sessolo, M.; Bolink, H. J. Efficient Monolithic Perovskite/Perovskite Tandem Solar Cells. *Adv. Energy Mater.* **2017**, *7*, 1602121.

(55) Ávila, J.; Momblona, C.; Boix, P.; Sessolo, M.; Anaya, M.; Lozano, G.; Vandewal, K.; Míguez, H.; Bolink, H. J. High Voltage Vacuum-Deposited $\text{CH}_3\text{NH}_3\text{PbI}_3 - \text{CH}_3\text{NH}_3\text{PbI}_3$ Tandem Solar Cells. *Energy Environ. Sci.* **2018**, *11* (11), 3292–3297.

(56) Borchert, J.; Milot, R. L.; Patel, J. B.; Davies, C. L.; Wright, A. D.; Martínez Maestro, L.; Snaith, H. J.; Herz, L. M.; Johnston, M. B. Large-Area, Highly Uniform Evaporated Formamidinium Lead Triiodide Thin Films for Solar Cells. *ACS Energy Lett.* **2017**, *2* (12), 2799–2804.

(57) Fan, P.; Gu, D.; Liang, G.-X.; Luo, J.-T.; Chen, J.-L.; Zheng, Z.-H.; Zhang, D.-P. High-Performance Perovskite $\text{CH}_3\text{NH}_3\text{PbI}_3$ Thin Films for Solar Cells Prepared by Single-Source Physical Vapour Deposition. *Sci. Rep.* **2016**, *6* (1), 29910.

(58) Lin, D.; Zhang, T.; Wang, J.; Long, M.; Xie, F.; Chen, J.; Wu, B.; Shi, T.; Yan, K.; Xie, W.; et al. Stable and Scalable 3D-2D Planar Heterojunction Perovskite Solar Cells via Vapor Deposition. *Nano Energy* **2019**, *59*, 619–625.

(59) Silver, S.; Yin, J.; Li, H.; Brédas, J.-L.; Kahn, A. Characterization of the Valence and Conduction Band Levels of $n = 1$ 2D Perovskites: A Combined Experimental and Theoretical Investigation. *Adv. Energy Mater.* **2018**, *8* (16), 1703468.

(60) Roldán-Carmona, C.; Gracia, P.; Zimmermann, I.; Grancini, G.; Gao, P.; Graetzel, M.; Nazeeruddin, M. K. High Efficiency Methylammonium Lead Triiodide Perovskite Solar Cells: The Relevance of Non-Stoichiometric Precursors. *Energy Environ. Sci.* **2015**, *8* (12), 3550–3556.

(61) Liu, M.; Johnston, M. B.; Snaith, H. J. Efficient Planar Heterojunction Perovskite Solar Cells by Vapour Deposition. *Nature* **2013**, *501* (7467), 395–398.

(62) Huang, X.; Sendner, M.; Müller, C.; Sessolo, M.; Gil-Escrig, L.; Kowalsky, W.; Pucci, A.; Beck, S.; Lovrinčić, R. Quantifying the Composition of Methylammonium Lead Iodide Perovskite Thin Films with Infrared Spectroscopy. *J. Phys. Chem. C* **2019**, *123* (36), 22083–22088.

(63) Palazon, F.; Pérez-del-Rey, D.; Dänekamp, B.; Dressen, C.; Sessolo, M.; Boix, P. P.; Bolink, H. J. Room-Temperature Cubic Phase Crystallization and High Stability of Vacuum-Deposited Methylammonium Lead Triiodide Thin Films for High-Efficiency Solar Cells. *Adv. Mater.* **2019**, *31* (39), 1902692.

(64) Olthof, S.; Meerholz, K. Substrate-Dependent Electronic Structure and Film Formation of MAPbI₃ Perovskites. *Sci. Rep.* **2017**, *7*, 40267.

(65) Parrott, E. S.; Patel, J. B.; Haghghirad, A.-A.; Snaith, H. J.; Johnston, M. B.; Herz, L. M. Growth Modes and Quantum Confinement in Ultrathin Vapour-Deposited MAPbI₃ Films. *Nano-scale* **2019**, *11* (30), 14276–14284.

(66) Lu, J.; Jiang, L.; Li, W.; Li, F.; Pai, N. K.; Scully, A. D.; Tsai, C.-M.; Bach, U.; Simonov, A. N.; Cheng, Y.-B.; et al. Diammonium and Monoammonium Mixed-Organic-Cation Perovskites for High Performance Solar Cells with Improved Stability. *Adv. Energy Mater.* **2017**, *7* (18), 1700444.

(67) Braly, I. L.; deQuilettes, D. W.; Pazos-Outón, L. M.; Burke, S.; Ziffer, M. E.; Ginger, D. S.; Hillhouse, H. W. Hybrid Perovskite Films Approaching the Radiative Limit with over 90% Photoluminescence Quantum Efficiency. *Nat. Photonics* **2018**, *12* (6), 355–361.

(68) Ross, R. T. Some Thermodynamics of Photochemical Systems. *J. Chem. Phys.* **1967**, *46* (12), 4590–4593.

(69) Endres, J.; Egger, D. A.; Kulbak, M.; Kerner, R. A.; Zhao, L.; Silver, S. H.; Hodes, G.; Rand, B. P.; Cahen, D.; Kronik, L.; et al. Valence and Conduction Band Densities of States of Metal Halide Perovskites: A Combined Experimental–Theoretical Study. *J. Phys. Chem. Lett.* **2016**, *7* (14), 2722–2729.

(70) Momblona, C.; Gil-Escrig, L.; Bandiello, E.; Hutter, E. M.; Sessolo, M.; Lederer, K.; Blochwitz-Nimoth, J.; Bolink, H. J. Efficient Vacuum Deposited P-i-n and n-i-p Perovskite Solar Cells Employing Doped Charge Transport Layers. *Energy Environ. Sci.* **2016**, *9* (11), 3456–3463.

(71) Hutter, E. M.; Hofman, J.-J.; Petrus, M. L.; Moes, M.; Abellón, R. D.; Docampo, P.; Savenije, T. J. Charge Transfer from Methylammonium Lead Iodide Perovskite to Organic Transport Materials: Efficiencies, Transfer Rates, and Interfacial Recombination. *Adv. Energy Mater.* **2017**, *7* (13), 1602349.

(72) Savenije, T. J.; Huijser, A.; Vermeulen, M. J. W.; Katoh, R. Charge Carrier Dynamics in TiO₂ Nanoparticles at Various Temperatures. *Chem. Phys. Lett.* **2008**, *461* (1–3), 93–96.

(73) Gélvez-Rueda, M. C.; Hutter, E. M.; Cao, D. H.; Renaud, N.; Stoumpos, C. C.; Hupp, J. T.; Savenije, T. J.; Kanatzidis, M. G.; Grozema, F. C. Interconversion between Free Charges and Bound Excitons in 2D Hybrid Lead Halide Perovskites. *J. Phys. Chem. C* **2017**, *121* (47), 26566–26574.

List of abbreviations and acronyms

2D	Two-dimensional
3D	Three-dimensional
AFM	Atomic Force Microscopy
APS	Air Photoemission Spectroscopy
AM	Air Mass
BABr	Butylammonium bromide
CB	Conduction Band
CBM	Conduction Band Minimum
CHCl ₃	Chloroform
DMF	Dimethyl formamide
DMSO	Dimethyl sulfoxide
E _b	Exciton binding energies
E _g	Energy bandgap
EDS	Energy-Dispersive x-ray Spectroscopy
EL	Electroluminescence
EQE	External Quantum Efficiency
ETL	Electron Transport Layer
FF	Fill Factor
FWHM	Full-Width Half-Maximum
GOPS	Glycidoxypropyltrimethoxysilane
HTL	Hole Transport Layer
IE	Ionization Energy

IR	Infrared
ITO	Indium Tin Oxide
J_{ph}	Photocurrent
J_{sc}	Short Circuit Current
LED	Light Emitting Diodes
MABr	Methylammonium bromide
MAPbBr ₃	Methylammonium lead bromide
MAI	Methylammonium iodide
MAPbI ₃ /MAPI	Methylammonium lead iodide
MPP	Maximum Power Point
PbBr ₂	Lead bromide
PbI ₂	Lead iodide
PCE	Power Conversion Efficiency of the cell
PEABr	Phenethylammonium bromide
PEAI	Phenethylammonium iodide
PEDOT:PSS	Poly(styrenesulfonate)
PLQY	Photoluminescence Quantum Yield
QCM	Quartz Crystal Microbalance
QFLS	Quasi-Fermi Level Splitting
R_{PTP}	Peak to peak roughness
R_{RMS}	Root-mean-square roughness
SE	Solvent Engineering
SEM	Scanning Electron Microscopy
SPPO1	9,9-spirobifluoren-2-yl-diphenylphosphine oxide
TRMC	Time-Resolved Microwave Conductivity

UV	Ultra Violet
VB	Valence Band
VBM	Valence Band Maximum
V_{oc}	Open circuit voltage
XRD	X-ray Diffraction
Z_{AVG}	Average height

Author contributions

- (1) La-Placa, M.-G.; Guo, D.; Gil-Escrig, L.; Palazon, F.; Sessolo, M.; Bolink, H. J. Dual-Source Vacuum Deposition of Pure and Mixed Halide 2D Perovskites: Thin Film Characterization and Processing Guidelines. *J. Mater. Chem. C* **2020**, 1902–1908. <https://doi.org/10.1039/c9tc06662d>.
- (2) La-Placa, M.-G.; Gil-Escrig, L.; Guo, D.; Palazon, F.; Savenije, T. J.; Sessolo, M.; Bolink, H. J. Vacuum-Deposited 2D/3D Perovskite Heterojunctions. *ACS Energy Lett.* **2019**, 2893–2901. <https://doi.org/10.1021/acsenergylett.9b02224>.
- (3) La-Placa, M. G.; Longo, G.; Babaei, A.; Martínez-Sarti, L.; Sessolo, M.; Bolink, H. J. Photoluminescence Quantum Yield Exceeding 80% in Low Dimensional Perovskite Thin-Films: Via Passivation Control. *Chem. Commun.* **2017**, 53 (62), 8707–8710. <https://doi.org/10.1039/c7cc04149g>.
- (4) Avila, J.; La-Placa, M. G.; Longhi, E.; Sessolo, M.; Barlow, S.; Marder, S. R.; Bolink, H. J. Ruthenium Pentamethylcyclopentadienyl Mesitylene Dimer: A Sublimable n-Dopant and Electron Buffer Layer for Efficient n-i-p Perovskite Solar Cells. *J. Mater. Chem. A* **2019**, 7 (45), 25796–25801. <https://doi.org/10.1039/c9ta09838k>.
- (5) La-Placa, M.-G.; Igual-Muñoz, A. M.; Romero, J.; Daniels, R. E.; Kozhevnikov, V. N.; Sessolo, M.; Bolink, H. J. Red Light-Emitting Electrochemical Cells Employing Pyridazine-Bridged Cationic Diiridium Complexes. *ECS J. Solid State Sci. Technol.* **2019**, 8 (6), R84–R87. <https://doi.org/10.1149/2.0161906jss>.
- (6) Longo, G.; Momblona, C.; La-Placa, M. G.; Gil-Escrig, L.; Sessolo, M.; Bolink, H. J. Fully Vacuum-Processed Wide Band Gap Mixed-Halide Perovskite Solar Cells. *ACS Energy Lett.* **2018**, 3 (1), 214–219. <https://doi.org/10.1021/acsenergylett.7b01217>.
- (7) Gil-Escrig, L.; Momblona, C.; La-Placa, M. G.; Boix, P. P.; Sessolo, M.; Bolink, H. J. Vacuum Deposited Triple-Cation Mixed-Halide Perovskite Solar Cells. *Adv. Energy Mater.* **2018**, 8 (14), 1703506. <https://doi.org/10.1002/aenm.201703506>.

- (8) Hierlinger, C.; Trzop, E.; Toupet, L.; Ávila, J.; La-Placa, M. G.; Bolink, H. J.; Guerchais, V.; Zysman-Colman, E. Impact of the Use of Sterically Congested Ir(III) Complexes on the Performance of Light-Emitting Electrochemical Cells. *J. Mater. Chem. C* **2018**, *6* (24), 6385–6397. <https://doi.org/10.1039/c8tc01130c>.
- (9) Hallani, R. K.; Fallah Hamidabadi, V.; Huckaba, A. J.; Galliani, G.; Babaei, A.; La-Placa, M. G.; Bahari, A.; McCulloch, I.; Nazeeruddin, M. K.; Sessolo, M.; et al. A New Cross-Linkable 9,10-Diphenylanthracene Derivative as a Wide Bandgap Host for Solution-Processed Organic Light-Emitting Diodes. *J. Mater. Chem. C* **2018**, *6* (47), 12948–12954. <https://doi.org/10.1039/c8tc05013a>.
- (10) Babaei, A.; Rakstys, K.; Guelen, S.; Fallah Hamidabadi, V.; La-Placa, M. G.; Martínez-Sarti, L.; Sessolo, M.; Joel, H. A.; Gaudin, O. P. M.; Schanen, V.; et al. Solution Processed Organic Light-Emitting Diodes Using a Triazatruxene Crosslinkable Hole Transporting Material. *RSC Adv.* **2018**, *8* (62), 35719–35723. <https://doi.org/10.1039/C8RA07184E>.
- (11) Keller, S.; Brunner, F.; Junquera-Hernández, J. M.; Pertegás, A.; La-Placa, M. G.; Prescimone, A.; Constable, E. C.; Bolink, H. J.; Ortí, E.; Housecroft, C. E. CF₃ Substitution of [Cu(P[^]P)(Bpy)][PF₆] Complexes: Effects on Photophysical Properties and Light-Emitting Electrochemical Cell Performance. *Chempluschem* **2018**, *83* (4), 217–229. <https://doi.org/10.1002/cplu.201700501>.
- (12) Sessolo, M., La-Placa, M-G., Martínez-Sarti, L., Bolink, H. J. Perovskite Light-emitting Devices-Fundamental and Working Principles-Halide Perovskites: Photovoltaics, Light Emitting Devices, and Beyond. Book, Wiley-VCH Verlag GmbH & Co. KGaA, 2018, 199-221.
- (13) Wong, M. Y.; La-Placa, M. G.; Pertegas, A.; Bolink, H. J.; Zysman-Colman, E. Deep-Blue Thermally Activated Delayed Fluorescence (TADF) Emitters for Light-Emitting Electrochemical Cells (LEECs). *J. Mater. Chem. C* **2017**, *5* (7), 1699–1705. <https://doi.org/10.1039/c6tc04821h>.
- (14) Ertl, C. D.; Momblona, C.; Pertegás, A.; Junquera-Hernández, J. M.; La-Placa, M. G.; Prescimone, A.; Ortí, E.; Housecroft, C. E.; Constable, E. C.; Bolink, H. J. Highly Stable Red-Light-Emitting Electrochemical Cells. *J. Am. Chem. Soc.* **2017**, *139* (8), 3237–3248. <https://doi.org/10.1021/jacs.6b13311>.

- (15) Longo, G.; La-Placa, M. G.; Sessolo, M.; Bolink, H. J. High Photoluminescence Quantum Yields in Organic Semiconductor–Perovskite Composite Thin Films. *ChemSusChem* **2017**, *10* (19), 3788–3793. <https://doi.org/10.1002/cssc.201701265>.
- (16) Martínez-Sarti, L.; Koh, T. M.; La-Placa, M. G.; Boix, P. P.; Sessolo, M.; Mhaisalkar, S. G.; Bolink, H. J. Efficient Photoluminescent Thin Films Consisting of Anchored Hybrid Perovskite Nanoparticles. *Chem. Commun.* **2016**, *52* (76), 11351–11354. <https://doi.org/10.1039/c6cc05549d>.
- (17) Gemmi, M.; La Placa, M. G. I.; Galanis, A. S.; Rauch, E. F.; Nicolopoulos, S. Fast Electron Diffraction Tomography. *J. Appl. Crystallogr.* **2015**, *48* (3), 718–727. <https://doi.org/10.1107/S1600576715004604>.
- (18) Monti, F.; La Placa, M. G. I.; Armaroli, N.; Scopelliti, R.; Grätzel, M.; Nazeeruddin, M. K.; Kessler, F. Cationic Iridium(III) Complexes with Two Carbene-Based Cyclometalating Ligands: Cis versus Trans Isomers. *Inorg. Chem.* **2015**, *54* (6), 3031–3042. <https://doi.org/10.1021/acs.inorgchem.5b00148>.

Acknowledgements

This PhD has been a long journey where a lot has changed, where I have achieved more than I ever imagined and which has been made unique by many people to whom I would like to express my gratitude.

Firstly, I would like to thank my supervisors, Henk Bolink and Michele Sessolo for giving me the opportunity to work in this fantastic group. *Henk*, thank you for the challenges you have entrusted me with, which have allowed me to gain all the knowledge I own now. Thanks for caring, supporting and guiding me also during difficult time, I deeply appreciate it. Thank you for all your advice and for always being willing to listen and discuss despite your busy schedule. *Michele*, sono molte le cose per cui devo ringraziarti, servirebbe un sezione a parte, ma so che apprezzi la sintesi quindi cercherò di essere breve. Grazie per il tuo supporto costante a livello lavorativo e personale, per la tua grande empatia, per il tuo inesauribile aiuto. Sei stato uno dei migliori insegnanti e mentori che io abbia mai avuto. I ricordi di questi anni e di questa tesi sarebbero stati more bitter and less sweet senza i tuoi preziosi consigli e la tua sensibilità. Per tutto questo e per molto altro, grazie di cuore.

Maria, gracias por acompañarme siempre desde el principio, para apoyarme y escucharme cuando lo necesité y para hacerme sentir que ante cualquier problema tu ayuda no me faltaría. Gracias por haber sido mi hermana mayor aquí en Valencia, por motivarme y por ser una verdadera inspiración. Y gracias claramente por tu infinita paciencia delante la larga lista de papeleo de estos años. *Benni*, eres uno de los mejores amigos que Valencia me ha regalado y uno de mis principales apoyos. Gracias por ser la persona en la que siempre puedo confiar, por entenderme tan fácilmente y sobre todo gracias por todas las risas y las profundas discusiones en tu chill out temple. *Azin*, thanks for the support and all the help of these years, many are the things that we have lived together. Thanks for all the laughs in our trips around Spain. Thanks for our Mat and Pat moments and for the beautiful aromas of your Iranian dishes. *Lidon*, eres una persona increíble, siempre dispuesta a escuchar y ayudar. Tienes un talento sin igual en la organización y eficiencia (sólo tu puedes usar tres evaporadoras diferentes al mismo tiempo). Muchísima gracias por toda tu ayuda a lo largo de los años y especialmente en esta última etapa. *Laura*, gracias por ser siempre

disponible a ayudar y por el gran apoyo que me diste en mis primeros pasos en Valencia y en el trabajo. Gracias por los buenos ratos, las risas y todos los viajes, desde Biarritz hasta New York. *Chris*, you are one of the kindest and smartest person I have ever met. You were born to be a researcher. It is in your blood. Thank you for all your help and for our scientific and non-scientific chats. *Dani*, tu auto-ironía, junto con las miles bromas diaria han hecho más liviano los días de trabajo en la oficina y en la sala limpia. ¡Mi corazón te lo agradece! A *Kassio* y *Ana*, ¡por la constante lucha en el laboratorio me identifico en vosotros! *Ana*, también si nuestro pequeño equipo de trabajo duró poco lo he disfrutado mucho, fuiste una sorpresa. Me encanta tu ironía y tu Spanish slang. *Kassio*, you have been a great addition to MOED group, always ready to help. You have a great personality and I really like talking to you. *Jorge A.*, gracias por acercarme al pensamiento de Nietzsche y también a la música española que me gusta. Gracias por los ratillos de humor entre vecino de escritorio en los días bueno. *Paco*, gracias por ayudarme a resolver mis dudas sobre el maravilloso mundo de la cristalografía y por todos tus consejos y trucos sobre la fotografía. *Angel*, gracias por estar siempre dispuesto a ayudar. Antes de encontrar el problema tú ya estás ahí con la solución. Eres increíble. Tu apoyo y experiencia está siempre disponible para todos sin el más mínimo interés. Gracias por todas nuestras charlas y por el buen rollo. *Isidora*, gracias por tu perenne sonrisa y para organizar planes por sobrevivir en tiempos de estrés. *Jorge F.*, gracias por todo lo que has hecho en el laboratorio a lo largo de los años. Sin tu fundamental trabajo, estaríamos perdidos. ¡Nunca olvidaré todos los sustos que me has pegado durante este doctorado! *Pablo*, gracias por todos tus consejos, tus bromas y el buen rollo. *Alejandra*, gracias por todas las medidas y por tu disponibilidad. *Giulia*, grazie per avere condiviso con me sfoghi ma soprattutto risate a Valencia, ad Oxford e nella mia amata Sicilia. *Cristina*, gracias por ser siempre tan amable y disponible. *Paz, David, Enrico, Toni, Javi, Vaheed, Sang, Yous, Bas, Lorenzo, Cihan, Xavi, Beom, Abhi, Miguel, Vicente, Nathan, Paula, Vladimir* (I hope I didn't forget anyone), thank you for being part of this great group, for your help, for the laughs and for all the time we have spent together.

I would like to express my gratitude to *Laura Miranda*, for welcoming me at OxfordPV during my research stay. Many thanks also to *Alice, Angela, Laura, Tania, Faye, Thomas* and to all the other for contributing to an experience that enriched me both professionally and personally.

Alvin, admiro mucho la persona maravillosa que eres. Gracias por simplificar mis complicados pensamientos, por apoyarme y ayudarme a superar todos los desafíos. Gracias por creer tanto en mí y por el cariño sin el cual, este último periodo habría sido muy diferente. Y sobre todo, gracias por tu comprensión y por aguantar mis días malos... . *Coti*, tienes ese don especial de saber decirme las palabras necesarias en cada momento. Eres una de las personas más lindas que esta ciudad me ha dado. Gracias por tu dosis de positividad. *Mauro*, grazie per avere sempre creduto in me. ¡Hasta la vittoria, siempre! *Giuggi e Boris*, lontane ma vicine. Grazie per esserci sempre e comunque e per mostrarmi il mondo da altre prospettive. Many thanks to *Benji, Sarah, Sthefanie* and all those people without whom Valencia would not have been the same.

Ringrazio la mia *famiglia* per il supporto che mi ha dato. Per avermi insegnato ad essere tenace e sempre onesta con me stessa e con gli altri. Grazie a voi sono quella che sono oggi e se questo traguardo è stato raggiunto lo devo anche a voi.

~Maria Grazia~

